UCRL-20644

K^+D INTERACTIONS AT 12 GeV/c

David A. Lissauer
(Ph. D. Thesis)

August 1971

AEC Contract No. W-7405-eng-48

UCRL-20644

DISCLAIMER

K^+D INTERACTIONS AT 12 GEV/c

Contents

K^+D INTERACTIONS AT 12 GeV/c

David Arie Lissauer
(Ph. D. Thesis)

Lawrence Radiation Laboratory
University of California
Berkeley, California 94720

May 20, 1971

ABSTRACT

We have studied the following reactions in a deuterium-filled bubble chamber exposed to a 12-GeV/c K^+ meson beam:

$K^+n \rightarrow K^0p$	163 events	(1)
$K^+n \rightarrow K^+\pi^-p$	6454 events	(2)
$K^+n \rightarrow K^0\pi^+\pi^-p$	865 events	(3)
$K^+D \rightarrow K^+\pi^+\pi^-D$	5834 events	(4)
$K^+D \rightarrow K^0\pi^+D$	133 events	(5)

We measured the differential cross section for the charge exchange reaction $K^+n \rightarrow K^0p$ and found that the forward amplitude is mainly real, the differential cross section equals that for the $K^-p \rightarrow \bar{K}^0n$ charge exchange reaction, and the differential cross section agrees well with the prediction of the Regge pole model of Rarita and Schwarzchild.

The reaction $K^+n \rightarrow K^+\pi^-p$ was found to be dominated by $K^*(890)$, $K^*(1420)$ production. Evidence is presented for the existence of: a) a possible enhancement at $M(K\pi) \approx 1250$ MeV with an angular distribution consistent with a spin parity $J^P = 0^+$ or 1^-; b) $K^*(1380)$ resonance with $M \approx 1380$ MeV,

$\Gamma < 150$ MeV, with spin parity 0^+ if produced by pion exchange, but $J^P = 1^-$ or 2^+ cannot be ruled out; c) structure in the K^+, π^- system at a mass near 1.85 GeV. One interpretation of the observation is the production by pion exchange of a $J^P = 3^- K^*$ resonance at about this mass, which interferes strongly with other processes.

The coherent reaction $K^+ D \to K^+ \pi^+ \pi^- D$ is dominated by Q^+ production. Evidence for structure in the Q^+ region is presented. Assuming two resonances are present, the result can be interpreted as the mixing of two $J^P = 1^+ K^*$ states. We have also studied D^{*++} and L produced in the same final state.

The reaction $K^+ D \to K^0 \pi^+ D$ is dominated by $K^*(890)$ produced by vector exchange.

I. INTRODUCTION

The SLAC 82" bubble chamber was exposed to an rf-separated K^+ meson beam.[1] Resolution in beam momentum to within $\Delta p/p = \pm .2\%$ was achieved by using known correlations between beam momentum and transverse position in the chamber. Approximately 500,000 exposures were taken and analyzed. Experimental details and cross section calculations are given in the Appendix.

The experiment was intended to study in detail both K^+d coherent reactions and K^+n charge exchange reactions. If it is desired to study neutron interactions, the lack of stable free neutrons must be overcome by obtaining data from bound neutrons. Usually the deuteron, a system of a loosely bound proton and neutron, is used. The problems arising from relative motion of the two nucleons and difficulties of analysis and interpretation are discussed in Chapter II. Coherent reactions are of special interest since the deuteron is in an I = 0 state, and if the reaction is coherent, it will allow only I = 0 exchange in the t channel.

In this paper we report the results of the reactions:

$K^+d \to K^0pp$	189 events	(1)
$K^+d \to K^+\pi^-pp$	6784 events	(2)
$K^+d \to K^0\pi^+\pi^-pp$	949 events	(3)
$K^+d \to K^+\pi^+\pi^-d$	5834 events	(4)
$K^+d \to K^0\pi^+d$	133 events	(5)

The elastic charge exchange reaction $K^+n \to K^0p$ offers an opportunity for detailed study of the problems of ρ-A_2 exchange degeneracy and the validity of Regge pole approximation to the scattering amplitudes. While this reaction has been studied extensively up to 5.5 GeV/c, little has been reported at higher

momenta. We have measured the differential cross section for this reaction and found it to be equal to that of $K^- p \to \bar{K}^0 n$ charge exchange reactions, which supports the notion of exchange degeneracy.

In the nonelastic charge exchange reactions we have found reaction (2) to be dominated by $K^*(890)$ and $K^*(1420)$ production. $K^*(890)$ production can be described well by an O. P. E. model proposed by G. Abrams and U. Maor.[21] We have found evidence for additional structure in the $K^+\pi^-$ mass spectrum:

a) At $M(K^+\pi^-) \approx 1250$ MeV we found evidence for a possible enhancement; if interpreted as a resonance and if pion exchange is assumed, spin parity values of $J^P = 0^+$ or 1^- are indicated.

b) At $M(K^+\pi^-) \approx 1380$ MeV we found evidence for a resonance with $\Gamma < 150$ MeV and $J^P = 0^+$ if produced by pion exchange, but $J^P = 1^-$, 2^+ cannot be eliminated.

c) At $M(K^+\pi^-) \approx 1850$ MeV there was evidence for a broad mass enhancement. The angular distribution requires the presence of more than one J^P state. On the assumption of pion exchange the highest J^P value required is $J^P = 3^-$.

We have also determined the intensities for K(1420) decay into $K^*(890)\pi$ and $K\rho$ and found the $K^*(1420)$ branching ratios to be in agreement with SU_3 predictions.

The coherent reaction $K^+ D \to K^+\pi^+\pi^- D$ is dominated by low $K\pi\pi$ mass, Q^+ production. The Q^+ has $I = 1/2$, and spin parity $J^P = 1^+$. We show that the Q^+ can be described in terms of two Breit-Wigners. The fact that two mesons are produced off the deuteron supports the notion of K^* mixing. The $D\pi$ mass is dominated by D^{*++} production. We show evidence that D^{*++} is not a resonance but probably the result of nucleon recombination for the reaction $K^+ d \to K^+\pi^- \Delta^{++} n$.

We find that the L^+ produced in this reaction is associated with low $D\pi^+$ mass.

II. THE DEUTERON TARGET

The bubble chamber was filled with deuterium because of the need for a pure I = 0 target to study coherent reactions and for a neutron target to study charge exchange reactions. The deuteron is a lightly bound composite of a proton and a neutron predominantly in the S-wave, J spin 1 state.[2] The deuteron binding energy is 2.2 MeV; thus it can easily break up in a collision into a proton and a neutron. Reactions where the deuteron does not break up are called coherent and are characterized by steep momentum transfer distributions. Reactions where two protons are present in the final state are called charge exchange reactions. In this chapter we will discuss (1) some important effects which must be considered when using a neutron as the target particle and (2) the problems of identifying coherent reactions on a deuteron.

A. The Hulthén Wave Function and the Spectator Momentum Distribution

The deuteron is a bound state of a proton and a neutron. The nuclear forces binding the nucleon together are presumed to be due to the exchange of virtual pions. Solving Schroedinger's equation with a suitable potential provides us with a wave function describing the radial distribution of the nucleons in the deuteron. Such a function was proposed by Hulthén.[3] The function is

$$\psi(r) = N\left(e^{-\alpha r} - e^{-\beta r}\right)/r$$

Using the normalization condition

$$\int |\psi(r)|^2 r^2 dr = 1$$

we get

$$N^2 = 2\alpha\beta(\alpha+\beta)/(\alpha-\beta)2$$

where

r = the separation between the two nucleons,

α = 4.5 MeV = (4.33 fermi)$^{-1}$ = $\sqrt{2\mu B}$

μ = deuteron reduced mass $1/\mu = 1/M_p + 1/M_n$

β = deuteron binding energy $\approx$2.2 MeV.

For the value of β, we use 7 as taken by Gluckstern and Bethe.[4] Other values of β are used in the literature. For example, β = 5.18 is used by Morovcsik.[5] But the features of the expected physical distributions are not very sensitive to the value of β.

The Fourier transformations of $\psi(r)$ give us the momentum space wave function $\phi(p)$ of the deuteron.

$\phi(p)$ is calculated to be

$$p^2\phi(p) = cp^2\left[\frac{1}{(p^2+\alpha^2)} - \frac{1}{(p^2+\beta^2)}\right]^2$$

where

$$\int \phi^2(p)p^2 dp = 1$$

In Fig. 1a we show the curve for the expected nucleon separation $r^2\psi^2(r)$ in the deuteron. In Fig. 1b we show the expected momentum distribution for the nucleons in the deuteron, $p^2\phi(p)$.

The expected momentum distribution $p^2\phi^2(p)$ can be measured experimentally to the extent that the impulse approximation is valid for K^+d collisions. The assumption here is that the spectator nucleon emerges from the deuteron after the collision with the same momentum as it had in the deuteron just before the collision.

For the charge exchange reactions $K^+d \rightarrow K^0pp$, $K^+d \rightarrow K^+\pi^-pp$, and $K^+d \rightarrow K^0\pi^+\pi^-pp$, the slower proton is assumed to be the spectator proton and the faster proton the recoil nucleon. For odd prong events, events with an invisible spectator, a four-constraint fit was made by assigning the invisible spectator a zero initial momentum and an error of $\Delta p_y = \Delta p_x = 30$ MeV/c, $\Delta p_z = 40$ MeV/c. All events which fit this hypothesis with chi-square probability greater than .1% were accepted.

In Figs. 2a, b, c, we show the spectator momentum distribution for the reactions $K^+d \rightarrow K^0pp$, $K^+d \rightarrow K^+\pi^-pp$, and $K^+d \rightarrow K^0\pi^+\pi^-pp$ respectively. In all distributions we see fair agreement with theoretical predictions for $P_s < 300$ MeV/c. The deviation at low P_s is attributed to the kinematic fitting procedure which starts the spectator momentum at zero. The excess of events with $P_s > 300$ MeV/c can be explained by one or more of the following conjectures:

(a) double scattering; rescattering of one of the final state particles with a spectator nucleon.

(b) inadequacy of the Hulthén wave function.

B. Flux Factor, Spectator-Beam Angle, and c.m. Energy

If an unpolarized deuteron target were to decay spontaneously into two nucleons, this decay would be isotropic about any fixed axis in the laboratory. In the framework of a spectator model, the spectator proton acts just as if it were the result of a decay. The isotropy of the spectator is therefor a test of the model.

There are several reasons why we can expect deviations from the above prediction. The statement fails to consider the fact that when the target particle is moving against the beam particle, it has a greater flux than when it moves away from the beam particle. Since the spectator has its momentum vector opposite to the target nucleon, this means that we would expect to have more events with cos > 0 than with cos < 0. To the first order, one can write the differential cross section normalized to the total cross section as

$$\frac{d\sigma}{dt} = \frac{\sigma_0}{2} \left[1 - \frac{\beta(n)}{\beta(k)} \cos\theta \right]$$

where $\beta(n)$, $\beta(k)$ are the velocities of the target nucleon and the incoming K^+ meson respectively, and θ is the angle between the nucleon and the beam direction in the laboratory system[6]. It is clear that as the beam momentum increases this effect becomes very small. At 12 GeV/c the relationship predicts a forward/backward ratio of spectator nucleons averaged over spectator momentum to be 1.01. The effect is more important at lower incident momenta and higher internal momenta.

It is also possible that scanning efficiency and measuring efficiency and measuring efficiency for short-recoil protons are not uniform.

In Fig. 3a, b, c we show the angle between the beam and the spectator proton for events in final states $K^+d \to K^0pp$, $K^+d \to K^+\pi$

and $K^+ d \rightarrow K^0 \pi^+ \pi^- pp$. The angular distributions for all final states are consistent with being flat. The small excess of events at $\cos\theta = \pm 1$ is attributed to the fact that heavily dipped tracks ($\cos\theta \approx 0$) have smaller scanning efficiency. These events will be classified as three-prong events but will be rejected in kinematic fit if the recoil track has too large a momentum.

An important effect arising from the motion of the nucleon in the deuteron is the smearing of the c.m. energy distribution. The c.m. energy for a 12-GeV/c K^+ incident on a nucleon is 4.85. If the target nucleon has a momentum of 60 MeV/c in the same or opposite direction as the beam, the energy changes to 4.4 and 5.2 respectively. This energy shift is responsible for the fact that interactions on the neutron do not have unique Chew-Low boundaries or Dalitz plot boundaries. This smearing effect is important if one wants to study the possibility of turnover of differential cross section in the forward direction or phenomena which have a strong energy dependence.

C. Pauli Exclusion Principle

After a charge exchange interaction on a neutron there are two protons in the final state. The deuteron is a proton-neutron in an S-wave (ignoring the small D-wave (ignoring the small D-wave component) spin-1 configuration. In this configuration the spin component of the wave function is symmetric, and it is forbidden by the Pauli exclusion principle for identical formations; i.e,, two protons. Thus we can see that at the limit of no momentum transfer, such charge exchange collisions cannot occur without a spin-flip on the nucleon.

The effect of the Pauli exclusion principle on charge exchange reactions of a neutron has been calculated for the reaction $K^+d \to K^0pp$ to be[7, 8]

$$\left.\frac{d\sigma}{dt}\right|_{KD\to K^0pp} = \left(1-H(t)\right)\left.\frac{d\sigma}{dt}\right|_{nf} + \left(1-1/3\,H(t)\right)\left.\frac{d\sigma}{dt}\right|_{f}, \qquad (1)$$

where $\left.\frac{d\sigma}{dt}\right|_{nf}$, $\left.\frac{d\sigma}{dt}\right|_{f}$ are the differential cross sections for spin-nonflig and spin-flip on a free neutron. Here H(q) is given by

$$H(q) = \int \psi^*(r)\, e^{-i\vec{q}\cdot\vec{r}}\, \psi(r)\, dr$$

where $4(r)$ is the deuteron wave function and $q = \vec{p}$ or $|q| \approx \sqrt{-t}$, where t is the four-momentum transfer squared. If we use the Hulthén wave function to evaluate H(q) we get[7]

$$H(\sqrt{-t}) = 2\alpha\beta/(\alpha-\beta)^2\left[\tan^{-1}(\sqrt{-t}/2\alpha) + \tan^{-1}(\sqrt{-t}/2\beta) - 2\tan^{-1}(\sqrt{-t}/(\alpha+\beta))\right].$$

In Fig. 4a we show the expected value of H(t) as a function of t, and in Fig. 4b we plot $\frac{1}{1-H(t)}$ versus t. From Fig. 4a we note that H(t)

is substantially different from zero only for $-t < .1$ $(GeV/c)^2$ and it is only in this range that Pauli exclusion is important. We also show the initial tangent and a chord to the curve H(t) versus t. They can be approximated by e^{-56t} and e^{-22t} respectively.

The derivation of Eq. (1) uses the closure approximation to evaluate the correlation factor H(t). In an interaction at $t = 0$, $H(t) = 1$, the final state protons have the same orbital angular momenta as did the neutron and proton in the initial state ($I = 0$). The deuteron is in a $J = 1$, $S = 1$ state. If there were no spin-flip on the nucleon, the total spin of the two protons would still be $S = 1$, $J = 1$, $L = 0$. But the Pauli exclusion principle forbids such a state. Therefore the spin-nonflip amplitude should vanish at $t = 0$. For the case where there was a spin-flip at the nucleon vertex, when we start an unpolarized deuteron, ($^3S_1$), there are three possible configurations. They are (a) up-up, (b) down-down, and (c) up-down. Clearly (a) and (b) after a spin-flip will have an up-down configuration which can be an $S = 0$ state, which is allowed. But if the initial state was up-down, the final state will be an $S = 1$ state, and this would not be allowed.

To correct for the deuteron effect, one must know the relative size of spin-flip and spin-nonflip cross sections. In practice it is necessary to get this ratio from model-dependent predictions.

D. Glauber Screening

If we imagine that the target deuteron is composed of two nucleons which are considered to be tiny spheres packed close together, then the spheres will line up behind each other part of the time and thus reduce the effective cross section. In 1955 Glauber derived the expression to explain this effect. The expression is

$$\sigma(K^+d) = \sigma(K^+n) + \sigma(K^+p) - \sigma(Kp)\sigma(Kn)/4\pi\langle r^2\rangle$$

where $\langle r^2\rangle$ is the average separation between two nucleons.

In 1966 Willkins[11] derived a modified formula which exhibits charge independence. His correction terms became

$$\sigma(Kp)\sigma(Kn) - \frac{1}{4}\left[\sigma(Kp) - \sigma(Kn)\right]^2/4\pi\langle r^2\rangle$$

Clearly, at our energy $\sigma(Kp) \approx \sigma(Kn)$[10] and hence the two formulae are identical.

A value for $\langle \frac{1}{r2}\rangle$ was calculated considering two nucleons to be black spheres with geometrical cross sections

$$\langle r^2\rangle \approx .02 \text{ m/b}^{-1}.$$

The correction at our energy is of the order

$$\frac{\sigma(K^+n)\,\sigma(K^+p)}{4\pi\,\langle r^2\rangle} \Big/ \left[\sigma(K^+p) + \sigma(K^+n)\right] \approx 4\%.$$

It is not known how this defect is to be apportioned between the various channels, but it seems implausible that the effect would differ much from channel to channel.

E. Identifying Coherent Deuteron Events

Events which correspond to those reactions in which the deuteron remains intact after the collision are called coherent deuteron events. In this experiment we have studied the two coherent deuteron reactions, $K^+d \to K^0\pi^+d$ and $K^+d \to K^+\pi^+\pi^-d$. As a result of the low binding energy of the deuteron, coherent deuteron reactions are characterized by a very steep momentum transfer distribution. Since the deuteron must have a minimum momentum of 110 MeV/c in order to be detected in the bubble chamber, a good fraction of the coherent events at low momentum transfer will have an invisible deuteron. The events with a visible deuteron in the final state will generally also make the corresponding one-constraint fit with a proton and neutron in the final state rather than a deuteron; i.e., $K^+d \to K^0\pi^+pn$ and $K^+d \to K^+\pi^+\pi^-pn$. If the event is not coherent, the deuteron breaks up and we would expect to find no strong correlation between neutron and proton direction. Furthermore, the invariant mass of the proton and neutron should likewise display no sharp enhancement near the deuteron mass. If, however, the event is really a coherent event, we would expect the proton and neutron directions to be nearly the same. Also, the invariant mass of the proton and neutron should be enhanced near the deuteron mass.

In Fig. 5a we show the invariant mass of the p,n in 1-MeV bins for all events satisfying the hypothesis $K^+d \to K^0\pi^+pn$. The shaded region represents the subsample which also fits the four-constraint deuteron hypothesis. In Fig. 5b we show the p,n mass for all events satisfying the hypothesis $K^+d \to K^+\pi^+\pi^-pn$.

The shaded region again represents those events which also fit the

reaction $K^+D \to K^+\pi^+\pi^-D$. In both reactions we note that the spike full width at half maximum (FWHM) $\approx$ 2 MeV near the minimum p, n mass is due entirely to the coherent events. In Fig. 6a, b we show the distribution in $\cos\theta$ for the reactions $K^+D \to K^0\pi^+pn$, $K^+d \to K^+\pi^+\pi^-pn$. (Here θ is defined as the angle between the proton and the neutron in the laboratory frame.) The shaded regions correspond to the subsample satisfying the corresponding coherent reaction. We note that, as expected, the coherent events are concentrated near $\cos\theta \approx +1$.

The final states $K^+D \to K^+\pi^+\pi^-pn$, $K^+d \to K^0\pi pn$ in the odd-prong topologies; i.e., three-prong, one-prong, and a vee, are underconstrained unless we assign the spectator proton zero momentum. In order to study the reliability of the coherent fits in the odd-prong events, we perform this pseudo-one-constraint fit.

In Fig. 7a we show the invariant mass for all events satisfying the hypothesis $K^+d \to K^+\pi^+\pi^-pn$ in the three-prong topology. There is a clear enhancement of events at low p, n mass although it is somewhat broader in this case (FWHM $\approx$ 7 MeV). The shaded region represents events also satisfying the coherent hypothesis. We interpret the depletion of events at M(p, n) $\approx$ 1900 MeV as a result of the artificial separation of three- and four-prong events. In Fig. 7b we plot the p, n mass for all neutron recoil events, $K^+d \to K^+\pi^+\pi^-p_sn$. The dip at 1900 MeV disappears. As before, the shaded region represents the coherent candidates. To select our coherent sample, we remove all events with M(p, n) > 1886 MeV in the corresponding one-constraint fit. Finally, the three-prong events also have a background due to τ decays; i.e., $K^+ \to \pi^+\pi^+\pi^-$. In order to remove

these events, we calculate the three out-going mesons' invariant mass assuming that they are all π mesons and remove all events with less than $M(\pi, \pi, \pi) < 560$ MeV.

III. K^+n ELASTIC CHARGE EXCHANGE REACTION

A. General Features of the Data

A total of 189 events satisfying the hypothesis $K^+D \rightarrow K^0pp$, $K^0 \rightarrow \pi^+\pi^-$ were found in both one-prong plus vee and two-prong plus vee topologies. All events which fit the seven-constraint multivertex fit $K^+D \rightarrow K^0pp$, $K^0 \rightarrow \pi^+\pi^-$ with chi-square probability greater than .1% were accepted as fulfilling this hypothesis. However, for the events with two visible prongs plus a vee, the spectator frequently is a very short track and therefore is difficult to measure accuretely. Although the momentum is adequately determined from range, the angles may be mismeasured for tracks of less than a few millimeters in length. For this reason a five-constraint multi-vertex fit is also performed for the two-prong plus vee events with short recoil, in which the angles of the short recoil are left free. Events which fit this special five-constraint hypothesis, but nót the seven-constraint hypothesis, are also accepted. For the reaction $K^+d \rightarrow K^0pp$, 52% of the events have two visible prootns and 48% of the events have only one visible proton in the bubble chamber. The recoil proton is taken to be the faster of the two. The spectator momentum distribution is in agreement with the expected distribution for spectator momenta, less than 300 MeV/c. The excess of events with $P_s > 300$ MeV/c is attributed to double scattering. These events have been excluded in the data sample. (see Chapter II).

The cross section for the reaction $K^+d \rightarrow K^0pp$ is 38.2 ± 32 μb 12 GeV/c. (See Appendix for details.) The corresponding cross-section for the reaction $K^+n \rightarrow K^0p$ is calculated to be 43.5 ± 3.6 μb where corrections for the suppression of cross section due to the

Pauli principle have been made assuming the cross section is dominated by the spin-nonflip amplitude.

In Fig. 8 we show the cross section for the reaction $K^+d \rightarrow K^0pp$ as a function of incident momentum[12]. Above 1 GeV/c incident momentum, the data can be fitted to a function of the form $\sigma(p) = Ap^{-n}$ where p is the incident momentum. The best fit parameters are $A = 7.3 \pm .2$ mb, $n = 2.1 \pm .05$ with chi-square 2.4 for four degrees of freedom.

In Fig. 9 we show the distribution $\frac{d\sigma}{dt}$ for the reaction $K^+D \rightarrow K^0pp$. In Fig. 10 we show the distribution $\frac{d\sigma}{dt}\Big|_{cex}$ for the charge exchange reaction $K^+n \rightarrow K^0p$ corrected for the Pauli principle. To apply the deuteron correction properly, one must know the relative size of spin-flip and spin-nonflip cross sections. The ratio is generally unknown, except in the forward direction where the spin-flip cross section must vanish.

The deuteron correction is significant only in the region $t < .1$ $(GeV/c)^2$, where the spin-flip term can be assumed to be small. Here we have neglected it. A least-squares fit to the data of Fig. 10 for a function of the form $\frac{d\sigma}{dt} = Ae^{-Bt}$ gives the values for the best fit $A = 237 \pm 20$ and $B = 5.6 \pm .3$ $(GeV/c)^{-2}$ with a chi-square value of 7.9 for 5 degrees of freedom.

In order to determine the relative strength of the real and imaginary parts of the K^+n charge exchange amplitude, the forward scattering intensity obtained in this experiment is compared with the forward intensity expected from the imaginary part of the amplitude calculated using the optical theorem and isotropic spin conservation. Specifically, isotopic spin conservation gives us the relations:

$$f(K^+p \to K^+p) = f_1,$$

$$f(K^+n \to K^+n) = \frac{1}{2}(f_1 + f_0),$$

$$f(K^+n \to K^0p) = \frac{1}{2}(f_1 - f_0),$$

$$f(K^+n \to K^0p) = f(K^+p \to K^+p) - f(K^+n \to K^+n)$$

The optical theorem gives us the relations

$$\text{Im } f(K^+p \to K^+p)\Big|_{t=0} = \frac{k}{4\pi}\,\sigma_{tot}(K^+p)$$

$$\text{Im } f(K^+n \to K^+n)\Big|_{t=0} = \frac{k}{4\pi}\,\sigma_{tot}(K^+p)$$

The best values of K^+p cross sections at present are[9]

$$\sigma tot(K^+p) = 17.3 \pm 1 \text{ mb},$$

$$\sigma tot(K^+n) = 17.6 \pm 4 \text{ mb}.$$

Using these values, we can predict

$$\frac{d\sigma}{dt}\,(\text{Im } f)\Big|^{cex}_{t=0} = 46 \pm 8.2\ \mu b/(\text{GeV}/c)^2$$

The experimentally extrapolated forward scattering cross section is $237 \pm 20\ \mu b/(\text{GeV}/c)^2$. Thus we have an indication here that the amplitude is largely real in the forward direction. Using the charge exchange data, we get

$$\left|\frac{\text{Im } f(0)}{\text{Re } f(0)}\right|^{2\ cex}_{t=0} \leq .02 \pm .4.$$

The disappearance of the imaginary part in the forward direction had important theoretical implications for the ρ, A_2 exchange degeneracy problems.

The dominance of the real part in K^+n charge exchange amplitude has been observed earlier at lower energies: at 2.3 GeV/c by Butterworth et al[8], and later Goldschmidt-Clermont et al confirmed it at 3 GeV/C[13]. The same has been observed by Cline et al at 5.5[16] GeV/c.

B. Regge Pole Formalism

A considerable amount of work has been done attempting to analyze the high-energy data from the reactions

$$\pi^- p \to \pi^0 n, \tag{1}$$

$$\pi^- p \to \eta^0 n, \tag{2}$$

$$K^- p \to \bar{K}^0 p, \tag{3}$$

$$K^+ n \to K^0 p\,. \tag{4}$$

When analyzed from the Regge pole phenomenological point of view, these reactions are of special interest because they allow a few high-lying Regge trajectories to be exchanged.

All reactions have the form pseudo-scalar + nucleon → pseudo-scalar + nucleon. In the t-channel description of the reaction, the quantum numbers of exchanged particles are restricted to I = 1, $C = P = (-1)^J = (-1)^I G$. G-parity restricts reaction 1) and reaction 2) to G = +1 and G = -1 respectively for the exchanged particles. In general we can write the t-channel helicity-nonflip ampltitude as

$$A(\pi^- p \to \pi^0 n) = A_\pi^-,$$

$$A(\pi^- p \to \eta^0 n) = A_\pi^+,$$

$$A(K^- p \to \bar{K}^0 n) = A_k^+ + A_k^-,$$

$$A(K^+ n \to K^0 p) = A_k^+ - A_k^-\,.$$

The amplitude $A^\pm = \Sigma A_i^\pm$ where $A_i^\pm$ are the contributing Regge trajectories.

From the factorization theorem we get a relation between the amplitudes when they connect to a π, K at the top vertex

$$\frac{A_i(\pi)}{A_i(K)} = F_i(t).$$

If SU(3) symmetry is unbroken and if all contributing trajectories are

octet members, we also have the relations

$$F_i(t) = F^+ = (2/3)^{1/2} \quad C_i = +1$$

$$F^- = -\sqrt{2} \qquad C_i = -1,$$

where C_i is the charge conjugation quantum number defined for the neutral member of the SU(3) octet. Similar relations exist for the spin-flip amplitude.

In the Regge pole model, each amplitude is given by the expression

$$A_i = \gamma_i(t) \frac{e^{-i\pi\alpha_i(t)} + \tau}{\sin\pi\alpha_i(t)} \; S^{\alpha_i(t)-1},$$

where γ_i = residue function,

α_i = trajectory parameter,

τ = signature.

The only well-known trajectory to satisfy the conditions are ρ, A_2 for the A^-, A^+ amplitudes, respectively.

If one considers the model with only the ρ, A_2 trajectories, there are some features which cannot be explained. First, the model predicts zero polarization for the $\pi^+ p \to \pi^0 n$ charge exchange reaction. (Only one trajectory, the ρ, can participate.) Experimentally, a non-zero polarization is observed. Second, the large difference between the charge exchange reactions $K^+ n \to K^0 p$ and $K^- p \to \bar{K}^0 n$ over the momentum range of 1 to 5.5 GeV/c cannot be explained by using only two trajectories. ($K^+ n$ charge exchange is larger than $K^- n$ charge exchange in this momentum interval.)

There have been different modifications of the "pure" Regge pole model in order to fit the data over all energies. A model by Rarita and Schwarzchild[14] requires the existence of an additional

trajectory, the ρ', in order to fit the data. In Fig. 10, we show their prediction for K^+n cross section at 12 GeV/c, using the parameters they attained by fitting low-energy data. The agreement is reasonably good.

Other attempts to modify the Regge pole model have been made by adding Regge cuts to the two trajectories ρ, A_2. There is no unique way of introducing Regge cuts into the theory. In Fig. 10 we show the prediction of Hartley, Moore and Moriarty[15], using Regge trajectories and cuts. The shape of the differential cross section seems to agree with the data, except for absolute normalization. However, in the forward direction the model predicts a cross section up to 60% higher than what we observe.

C. ρ-A_2 Exchange Degeneracy

The differential cross section for the K^+n and K^-p charge exchange reactions are given by

$$\frac{d\sigma}{dt}(K^+n \to K^0p) = \frac{1}{2}\left|A_s\right|^2 + \frac{3}{2}\left|A_R\right|^2 + \sqrt{3}\,\mathrm{Re}\,(A_s^* A_R),$$

$$\frac{d\sigma}{dt}(K^-p \to \bar{K}^0n) = \frac{1}{2}\left|A\rho\right|^2 + \frac{3}{2}\left|A_R\right|^2 - \sqrt{3}\,\mathrm{Re}\,(A_s^* A_R).$$

If exchange degeneracy holds, then $\alpha_\rho = \alpha_R$ and $\mathrm{Re}(A_\rho^* A_R) = 0$

$$\frac{d\sigma}{dt}(K^+n \to K^0p) = \frac{d\sigma}{dt}(K^-p \to K^0n),$$

where the A_2 trajectory has been called R. In addition, if interference term $\mathrm{Re}(A_\rho^* A_R)$ is zero, we also have the SU(3) sum rule

$$\frac{d\sigma}{dt}(K^-p \to \bar{K}^0n) = \frac{1}{2}\frac{d\sigma}{dt}(\pi^-p \to \pi^0n) + \frac{3}{2}\frac{d\sigma}{dt}(\pi^-p \to \eta^0n)$$

We have already mentioned that at lower energies there seems to be a great discrepancy between K^+ and K^- charge exchange differential cross sections. But Cline et al[16] have noticed that the two cross sections are already identical at 5.5 GeV/c. In Fig. 11 we show the differential cross section for $K^+n \to K^0p$ and $K^-p \to \bar{K}^0n$ at 12 and 12.3 GeV/c respectively. The data is from Astbury et al[17]. The agreement between K^+ and K^- data is very impressive, and it supports the notion of exchange degeneracy. Although a complicated conspiracy between residues and trajectory parameters could result in an accidental equality of K^+n, K^-p charge exchange differential cross section at some value of a and t, it is unlikely that this would be maintained over a wide range of s and t values.

The possibilities of the existence of secondary trajectories like ρ, R' have been suggested. This leads to an interference term of

$$\sqrt{3}\,\mathrm{Re}(A_\rho^* A_R + A_\rho A_{R'} + A_{\rho'}^* A_R + A_{\rho'}^* A_{R'}).$$

Assuming that ρ', R' are also exchange degenerate, we get

$$\frac{d\sigma}{dt}(K^+ n \to K^0 p) - \frac{d\sigma}{dt}(K^- p \to \bar{K}^0 n) = 2\sqrt{3}\,\mathrm{Re}(A_\rho^* A_{R'} + A_{\rho'}^* A_R),$$

which gives a sensitive way to test the existence of daughter trajectories. At our energy, the ρ', R' trajectories are expected to have only a small effect, and a set of two higher statistics experiments would be needed to detect them.

Strong exchange degeneracy relations imply that in addition to the trajectories being equal, $\alpha_\rho = \alpha_R$, the residues are also equal; that is,

$$\gamma_\rho = \gamma_R.$$

If strong exchange degeneracy holds, then the $K^+ n$ amplitude is purely real. At $t = 0$ we found

$$\left|\frac{\mathrm{Im}\, f}{\mathrm{Re}\, f}\right|^{2\mathrm{cex}}_{t=0} < .02 \pm .04,$$

which means that amplitude is mostly real. While this is true in the forward direction, we cannot determine Im f away from $t = 0$. The approximate validity of strong exchange degeneracy will explain the absence or strong suppression of Z^* resonances in the $K^+ n$ direct channel, since a purely real amplitude cannot describe a resonance.

D. Comparison with the Reaction $K^+p \to K^0\Delta^{++}$

The reaction $K^+p \to K^0\Delta^{++}$ is also dominated by ρ, A_2 exchange. In the Regge pole exchange formalism the meson vertices are identical in the two reactions, but the baryon vertices are different. On an SU(3) classification scheme the nucleons are members of an octet while the Δ is a member of a decuplet. Thus SU(3) gives us no prediction on the coupling behavior of $(p\bar{n}\,\rho)/(p\overline{\Delta^{++}}\rho)$ or $(p\bar{n}\,A_2/(p\overline{\Delta^{++}}A_2)$. It is of some interest to compare the two reactions and learn about the difference between a proton and a Δ^{++} in strong interactions.

In Fig. 12 we show the cross section for the two reactions $K^+d \to K^0pp$ and $K^+p \to K^0\Delta^{++}$ plotted against K^+ beam momentum. The cross sections for both reactions are essentially identical and fit the function of the form $\sigma(p) = A_p{}^{-n}$. The best fit parameters for p>2 GeV/c are A = 7.3 ± .2 mb, n = 2.1 ± .05 and A = 7.0 ± .2 mb, n = 2.0 ± .05 for $K^+d \to K^0pp$ and $K^+ \to K^0\Delta^{++}$ respectively. The agreement is remarkable and would imply that vertex function

$$p\bar{n}\,\rho \approx p\,\overline{\Delta^{++}}\,\rho,$$

$$p\bar{n} \approx p\,\overline{\Delta^{++}}\,A_2.$$

On the other hand, when we look at the reaction $K^-p \to \bar{K}^0\Delta^-$ as compiled by Kwan Lai and Louie[18], it indicates that from 3-5(GeV/c momentum, the cross sections for $K^-n \to K^0\Delta^-$ are only 60% of $K^+p \to K^0\Delta^{++}$. This is particularly disturbing in view of the equality of K^+p, $\bar{K}n$ elastic charge exchange cross sections. Better data at higher momenta are needed in $K^-p \to \bar{K}^0D^-$ reactions to clarify the nature of this discrepancy.

IV. K^{*0} PRODUCTION

The film has been scanned for all events which have three-prong or four-prong topologies, both with and without associated vee decays. In addition, all four-prongs measured were required to have at least one track which stopped in the bubble chamber.

All events which fit the four-constraint hupothesis, either $K^+d \to K^+\pi^- pp$ or $K^+d \to K^0\pi^+\pi^- pp$ with χ^2 probability greater than 0.1%, were accepted. The spectator proton (here defined as the slower proton in the laboratory frame) has a momentum distribution in agreement with that expected from the Hulthén wave function for momenta less than 300 MeV/c. In the subsequent analysis, only events with $P_s < 300$ MeV/c are accepted. (See Chapter II.) There are 6784 and 949 such events for the reactions $K^+d \to K^+d \to K^+\pi^- pp$ and $K^+D \to K^0\pi^+\pi^- pp$ respectively, of which 67% are three-prong and 33% are four-prong in each case. The cross sections for these reactions have been determined to be 400 ± 8 μb for $K^+D \to K^+\pi^- pp$ and 210 ± 20 μb for $K^+d \to K^0\pi^+\pi^- pp$. Here the quoted errors reflect statistical uncertainties only. Corrections for the invisible K^0 decay modes have been included.

A. General Features of the Reaction $K^+n \to K^+\pi^- p$

In Fig. 13 we show the Dalitz plot for the reaction $K^+n \to K^+\pi^- p$. The outstanding features include 1) a large low $p\pi^-$ band which we associate with several $N^*_{1/2}$ resonance present in that mass region, 2) a $K^*(890)$ band, 3) a $K^*(1420)$ band, 4) a depletion of events in the region past the $K^*(1420)$ and a wide band of events

at $M^2(K,\pi) \approx 3.0\ (GeV)^2$, 5) a general lack of background; specifically, there is no indication of a band parallel to the third Dalitz plot boundary which would correspond to a Z^* decaying in the elastic channel K^+p.

In Fig. 14a we show the Chew-Low plot $t_{K\text{-}K\pi}$ vs $M^2(K^+,\pi^-)$ for all events in this final state. In Fig. 14b we show the Chew-Low plot $t_{K\text{-}K\pi}$ vs $M^2(K,\pi)$ for events left after removing the low $p\pi^-$ enhancement [$M(p,\pi^-) < 18$ GeV]. In both figures, $K^*(890)$ and $K^*(1420)$ bands are produced mainly at low t. Depletion of events past $K^*(1420)$ can also be seen. In Fig. 15 we show the Chew-Low plot $t_{p\text{-}p\pi^-}$ vs $M^2(p,\pi^-)$. The low $p\pi^-$ mass enhancement is produced primarily at low t, but some $N^*_{1/2}$ production can be seen at higher t regions.

In Fig. 16 we show the $p\pi^-$ invariant mass plot. No details of the structure can be seen in the mass enhancement, which drops off sharply at $M(p,\pi^-) \approx 1.8$ GeV. The particle data tables[19] list seven $N^*_{1/2}$ resonances with masses less than 1.8 GeV, several of which could contribute to the low mass enhancement in the distribution. Except for the possibility of some structure at $M(p\pi^-) \approx 1.4$ GeV which is probably associated with the P_{11} Roper resonance, none of them can be resolved without t cuts. (For more detailed analysis of the N^* region, see Section H.) In Fig. 17a we show the $M(K^+,\pi^-)$ mass projection for all events. The $K^*(890)$, $K^*(1420)$, and the large enhancement at higher $K\pi$ masses can be seen. This enhancement is mostly a reflection of the low $p\pi^-$ mass enhancement. In Fig. 17b we show the $K\pi$ mass projection for events with $t' < .2(GeV/c)^2$, where t is defined as the

four-momentum transfer between beam kaon and outgoing $K\pi$. Apart from $K^*(890)$ and $K^*(1420)$, a clear enhancement above background can be seen at $M(K, \pi) \approx 1.8$ GeV.

In Fig. 18 we show the two-dimensional plot, $\cos\theta$ vs $M(K, \pi)$ for all events with $t'_{K-K\pi} < .2$ $(GeV/c)^2$. The $K^*(890)$ and $K^*(1420)$ bands stand out clearly. This will be discussed later, but note also that for the $M(K, \pi) \approx 1.8$ GeV there are many events with $\cos\theta < 0$; i.e., events which are far away from N^* reflection.

In Fig. 19a, b, c, d, e, f we show that $m = 0$ spherical harmonics moments $\langle Y_l^0 \rangle$ for all events with $t'_{K-K\pi} < .2$ $(GeV/c)^2$. In Fig. 20a, b, c, d, e, f we show $N\langle Y_l^0 \rangle$ where N is the number of events in a given bin for the same sample of events. The spherical harmonics moments are defined as

$$\langle Y_l^0 \rangle = \sum_{l=1}^{N} \frac{X_n}{N},$$

where X_n is the value of Y_l^0 $(\cos\theta)$ for the nth event. The errors quoted above are RMS and are given by

$$\delta(X) = [(\langle X^2 \rangle - \langle X \rangle^2)/N]^{1/2}.$$

The general features of the distributions are as follows:

At low $k\pi$ mass S- and P-waves are dominant. In the $K^*(1420)$ region D-wave becomes important, and at $M(K, \pi) \approx 1.75$ GeV, $\langle Y_5^0 \rangle$ and $\langle Y_6^0 \rangle$ become important. This suggests the presence of an F-wave in that region. A more detailed analysis will be given as we study the $K\pi$ meas spectrum later on in this chapter.

B. General Features of the Reaction $K^+n \to K^0\pi^+\pi^-p$

In Fig. 21 we show the invariant mass of $M(K^0\pi^+\pi^-)$. A clear $K^*(1420)$ signal can be seen. There is no low $K^0\pi^+\pi^-$ mass enhancement corresponding to the Q^+ produced in non-charge exchange reactions. In Fig. 22 we show the $p\pi^+\pi^-$ invariant mass plot. The shaded regions are for events in the Δ^{++} region, and we see that they are associated with low $p\pi^+\pi^-$ mass. In Fig. 23 we show a two-dimentional plot of $M(K^0, \pi^+)$ vs $M(p, \pi^-)$. There is a clear enhancement of events which corresponds to the reactions $K^+n \to K^*(890)\,\Delta^0$ and $K^+n \to K^*(1420)\,\Delta^0$. In Fig. 24 we show the projections for the $K^0\pi^+$ mass combination and $p\pi^-$ mass. A clear $K^*(890)$, $K^*(1420)$ signal can be seen in the invariant mass plot. A clear low mass enhancement can be seen in $p\pi^-$ mass corresponding to Δ^0 and low mass $N^*_{1/2}$ production. In Figs. 25 and 26 we show the two-dimensional plot $M(K^0, \pi^-)$ vs $M(p, \pi^+)$ and the invariant mass plot for $M(K^0, \pi^-)$, $M(p, \pi^+)$. No structure is seen in the $M(K^0\pi^-)$ mass plot. There is some Δ^{++} production, which is associated with the low $p\pi^+\pi^-$ invariant mass.

In Fig. 27 we show the two-dimensional mass plot $M(K^0, \pi^+)$ vs $M(\pi^+, \pi^-)$ for this reaction. Clear $K^*(890)$, $K^*(1420)$ bands can be seen in the $K\pi$ mass distribution. In the $\pi\pi$ mass distribution there is an excess of events in the ρ and f regions, especially in the cross-over region between the ρ, f, and K^* bands. In Fig. 28 we show the $\pi^+\pi^-$ mass distribution in which a clear ρ signal centered at $M(\pi\pi) = 740$ MeV can be seen.

C. $K^*(890)$ Production in the Reaction $K^+n \to K^+\pi^-p$

Events referred to here as $K^*(890)$ come from the reaction

$$K^+n \to K^*(890)\,p$$
$$\qquad\quad \big|\to K^+\pi^-$$

where all events with $K^+\pi^-$ invariant mass between 840 MeV and 940 MeV are taken as $K^*(890)$ events. In this reaction a total of 505 $K^*(890)$ events were found corresponding to a cross section of 45 ± 2.5 μb, taking into account the $K^0\pi^0$ decay mode of the $K^*(890)$.

In Fig. 19a, b we showed the Chew-Low plot t_{K-K} vs $M^2(K,\pi)$ and noted that $K^*(890)$ is produced primarily at low t. In Fig. 29 we show the differential cross section, $\frac{d\sigma}{dt}$ for $K^*(890)$ production. The distribution cannot be fitted to a single function of the form $A\,e^{-Bt}$. But if we fit the distribution separately in the two regions $t < .1\ (GeV/c)^2$ and $t > .1\ (GeV/c)^2$ we get the following values: $t < .1\ (GeV/c)^2$, $A = 550 \pm 15$, $B = 20 \pm 2$ with $\chi^2 = 2$ for one degree of freedom; $t > .1\ (GeV/c)^2$, $A = 122$, $B = 4.5 \pm .5$, with $\chi^2 = 2.3$ for 3 degrees of freedom.

The steepness of the momentum transfer distribution in the forward direction indicates that the reaction is dominated by one-particle exchange. In this reaction t_{min} for $K^*(890)$ production is $.005\ (GeV/c)^2$. There is no substantial difference between $\frac{d\sigma}{dt}$ and $\frac{d\sigma}{dt'}$ distribution (where $t' = t - t_{min}$). The turnover in the forward direction persists after a correction is made to compensate for the suppression of the cross section due to Pauli exclusion principle. The pion exchange contribution to the cross section is expected to go to zero at $t = 0$. We cannot determine from our

data whether the effect we are seeing is due to Fermi motion of the target and peculiarities in the kinematic fitting or to a real effect of vanishing cross section at t = 0.

Decay distribution of $K^*(890)$

In Fig. 19a, b we showed the $\langle Y_1^0 \rangle$ moments and noted that the region of $K^*(890)$ is completely dominated by S- and P-waves. There are no indications that any higher waves are present. In Fig. 30 we show the polar and azimuthal decay angular distribution for $K^*(890)$ for events with $t' < .2$ $(GeV/c)^2$. θ, ϕ are defined as the Jackson decay angle for the $K\pi$ system. The polar decay angular distribution has a large $\cos^2\theta$ component, which suggests predominance of pseudo-scalar exchange. The distribution is peaked in the forward direction, which indicates the presence of S-wave in this region. Note also that the asymmetry is not a reflection of the $N^*_{1/2}$. This can be seen clearly from the Dalitz plot shown in Fig. 13, where the asymmetry extends well beyond the $N^*_{1/2}$ band. We have fitted the data to a function of the form $\sum_n a_n P_n(\cos\theta)$, where P_n are the Legendre polynomials of order n. We obtain a good fit to the data with a χ^2 of 18 for 17 degrees of freedom. The parameters of the best fit are

$$a_0 = 1, \quad a_1 = .7 \pm .1, \quad a_2 = .89 \pm .1.$$

The azimuthal decay distribution is not isotropic, which indicates the presence of some non-pseudo-scaler contribution to the exchange process even at low t.

Assuming the $K^*(890)$ region is dominated by P wave, the density matrix elements are given by[37]

$$W(\cos\theta, \phi) = \frac{1}{4\pi}\left[\frac{3}{2}(1 - \rho_{00}) + \frac{3}{2}(3\rho_{00} - 1)\cos^2\theta - 3\rho_{1-1}\sin^2\theta \cos 2\phi - 3\sqrt{2}\, \mathrm{Re}\,\rho_{10} \sin^2\theta \cos\phi\right].$$

In Fig. 3a, b, c we show the density matrix element ρ_{00}, σ_1^+, σ_1^- are defined as

$$\sigma_1^+ = \rho_{11} + \rho_{1-1} \qquad \sigma_1^- = \rho_{11} - \rho_{1-1}$$

at high energy. σ_1^+, σ_1^- measure the relative contribution of natural and unnatural parity exchange.[19] From Fig. 31 we see that $K^*(890)$ is dominated by pion exchange in the forward direction, but at large t both vector and pseudo-vector exchange become important.

It is difficult to calculate the absolute phase of the S-wave in the $K^*(890)$ region. However we can get an estimate of the S-wave phase shift from the fact that $\langle Y_1^0 \rangle$ goes to zero near $M(K, \pi) \approx 1$ GeV. Assuming P wave has a Breit-Wigner shape centered at 890 MeV with a width of 50 MeV, then the P-wave phase is $\beta_p \approx 150°$ at 1 GeV. Since

$$\mathrm{Re}\,\langle Y_1^0 \rangle \propto \cos(\beta_p - \beta_s) \approx 0$$

implies that $\beta_s \approx 60°$ or $210°$.

Since $\langle Y_1^0 \rangle$ is positive shortly after 1 GeV, it is plausible to assume that $\beta_s \approx 60°$ and is increasing in that region.

The phase shift analysis performed on the world tape for the $K\pi$ mass spectra for the reaction $K^+p \to K^+\pi^-\Delta^{++}$ has shown a similar effect.[39,44]

One-Particle Exchange Model Prediction

The steepness of the four momentum transfer distributions suggests that $K^*(890)$ production can be described by a one-particle exchange model. As has been shown, the reaction is dominated by pion exchange. We have used a model suggested by G. S. Abrams and V. Maor[21] to predict the forward differential cross section.

The model uses an evasive Reggeized one-pion exchange model which smoothly reduces to the Born term at the pion pole. The Born term for OPE for the process $a+b \to c+d$ is calculated to be

$$\sigma_0^- = \frac{2\pi}{3s\,q^2} G^2 \left|\frac{1}{t-m_\pi^2}\right|^2 \frac{a_c^2 b_d^2}{m_\pi^2} [(m_b+m_d)^2 - t],$$

where $\sigma_0^- = \rho_{00} \left|\frac{d\sigma}{dt}\right|$ is the natural parity contribution to the exchange process.

$$q^2 = [s - (m_a - m_b)^2]\,[s - (m_a + m_b)^2]/4s,$$

$$a_c^2 = [t - (m_a - m_c)^2]\,[t - (m_a + m_c)^2]/4m_c^2,$$

$$b_d^2 = [t - (m_b - m_d)^2]\,[t - (m_b + m_d)^2]/4m_d^2.$$

The coupling constant is $G^2 = (g^2_{K\pi K^*}/4\pi)\,(g^2_{pn\pi}/4\pi)$. To Reggeize this expression the pion propagator $1/t-m_\pi^2$ is replaced by

$$\pi\alpha(0)\ \frac{1+e^{-i\pi\alpha}}{2\sin\pi\alpha}\ \frac{(1+2\alpha)(1+2\alpha/3)\,\Gamma(\alpha+1/2)}{\Gamma(1/2)\Gamma(\alpha+1)} \left(\frac{s-u}{2s_0}\right),$$

where $\alpha = \alpha'(0)\,(t - m_\pi^2)$ $\alpha'(0) = 1$.

In Fig. 32 we show the natural parity contribution to the differential cross section $\rho_{00} \left|\frac{d\sigma}{dt}\right|_{Kn \to K^*(890)p}$. The differential

cross section has been corrected in the forward direction to compensate for the suppression in production due to the Pauli exclusion principle. The correction was made assuming 100% spin-flip amplitude. The curve plotted in Fig. 32 is an absolute prediction of the Abrams-Maor model. It fits the data fairly well, both in shape and in absolute normalization.

D. $M(K^+\pi^-)$ Between 1 and 1.3 GeV

In Fig. 17 we showed the $K^+\pi^-$ mass distribution for all events in the reaction $K^+n \to K^+\pi^-p$. We noted that there are a large number of events in the region between the $K^*(890)$ and $K^*(1420)$ regions. When the sample is restricted to events with $t < .1$ $(GeV/c)^2$ (see Fig. 33), a sharp spike is seen at $M(K,\pi) \approx 1250$ MeV. The statistical significance of the peak is critically dependent on the way in which the background is determined in this region. The whole region between 1 and 1.3 GeV is dominated by S-wave, but some P-wave is needed to explain the angular distribution. (See $\langle Y_1^0 \rangle$ moments shown in Fig. 19.) If the enhancement we observe at 1250 MeV corresponds to a specific resonant state, the angular distribution is consistent with the $J^P = 0^+$ or 1^- produced for an enhancement in this region. In a compilation by Dodd et al.[22] a K^* resonance at $M(K^+,\pi) = 1250$ MeV was indicated, which is in fair agreement with our observations. Other enhancements in this region have been reported: a $K^*(1080)$ by De Bare et al. and a $K^*(1160)$[24] by Crennell et al.[23] We have found some indication of structure in both these regions, but the statistical significance of any peak in these two regions is marginal in the present experiment.

E. $K^*(1420)$ Region

Evidence for an additional resonance. In the $K^+\pi^-$ mass distribution (see Fig. 17) we observe an unusually broad signal from 1.3 to 1.5 GeV which appears at first sight to be due to the $K^*(1420)$ with fitted parameters $M = 1413 \pm 5$ MeV and $\Gamma = 143 \pm 12$ MeV. We note, however, that the character of the $K^*(1420)$ decay angular distribution changes sharply at 1.4 GeV. Figure 34 shows the $\cos\theta$, ϕ distributions in (K^+, π^-) mass regions, where θ, ϕ are the Jackson decay angles for the $K\pi$ system. The distribution in $\cos\theta$ for the high-mass region, 1.4 to 1.5 GeV, is just the angular distribution expected from the decay of a $J^P = 2^+$ resonance produced by pion exchange. There is no evidence for a significant asymmetry, and the distribution may be fitted with D-waves with a substantial S-wave background. The $\cos\theta$ distribution for the low-mass region, 1.3 to 1.4 GeV, however (see Fig. 34a), requires no powers of $\cos\theta$ greater than 2 to achieve an excellent fit. The parameters for the fits to the angular distributions in Legendre polynomials $\sum_n a_n P_n(\cos\theta)$ are as follows: In the $M(K,\pi)$ region between 1.3-1.4 GeV (a_1/a_0) $= .36 \pm .11$ $(a_2/a_0) = .76 \pm .12$ with $\chi^2 = 17.8$ for 17 degrees of freedom. In the $M(K, \pi)$ region between 1.4-1.5 GeV $(a_1/a_0) = .09 \pm .1$, $(a_2/a_0) = 2 \pm .1$ $(a_3/a_0) = -.05 \pm .15$ and $(a_4/a_0) = 1.18 \pm .17$ with $\chi^2 = 10$ for 15 degrees of freedom.

In order to demonstrate the inconsistency of the angular distributions in the two mass regions, we have tried to fit the theoretical angular distribution expected from the fit to the entire region, 1.3 to 1.5 GeV, renormalized to the actual number of events in each region, to the observed angular distributions. This fit has a confidence

level of 0.0005 in the 1.3- to 1.4-GeV region and 0.0001 in the 1.4- to 1.5-GeV region; thus, the two angular distributions are clearly inconsistent with being flat both mass regions (see Fig. 34).

We have considered the effect of the low (p, π^-) mass enhancement on the angular distributions. The low $M(p, \pi^-)$ band on the Dalitz plot (Fig. 13) appears to be modulated by the $K^*(890)$ and $K^*(1420)$ bands. There is some evidence indicating superposition of $N^*(1520)$ and $N^*(1680)$ in the $K^*(1420)$ band. The excess of events in the overlap of the $K^*(1420)$ band with the $N^*(1520)$ and the $N^*(1680)$ can be seen on the Dalitz plot in Fig. 13. If we subtract the events attributable to these two N^*'s, the character of the $K\pi$ angular distributions is not significantly changed, although the forward peak in the 1.3- to 1.4-GeV region is slightly reduced and a small backward asymmetry is introduced into the angular distribution in the 1.4- to 1.5-GeV region.

As an alternate way of presenting the data, we plot the $K\pi$ mass distribution for two regions of $\cos\theta$ (see Fig. 34): $|\cos\theta| > .7$ (polar region), and $|\cos\theta| < .7$ (equatorial region). In the polar region the "$K^*(1420)$ peak" is fitted with parameters $M = 1439 \pm 5$ MeV and $\Gamma = 105^{+13}_{-12}$ MeV, while in the equatorial region the parameters are $M = 1373^{+6}_{-5}$ MeV and $\Gamma = 150^{+5}_{-14}$ MeV. This large (66-MeV) shift in the central value of the "$K^*(1420)$" with decay angle is obvious from Figs. 36a and 36b.

The possibility that a sharp change at 1.4 GeV in the character of the exchange mechanism producing a <u>single</u> resonance, produced by two different exchange mechanisms, e.g. π and ρ exchanges, would show a decay angular distribution characteristic of the particular mix of exchange mechanisms, but that distribution is not

expected to be a function of (K^+, π^-) mass, as in the case here.

Other decay modes. In a search for possible alternative decay modes of the $K_N^*(1370)$, we have studied the charge exchange reaction $K^+n \to K^0\pi^+\pi^-p$ in which the K^0 decays visibly in the bubble chamber. In the $K^0\pi^+\pi^-$ mass distribution, shown in Fig. 21, the $K^*(1420)$ signal is particularly clean, and it has been fitted with parameters $M = 1440 \pm 5$ MeV and $\Gamma = 109 \pm 24$ MeV. These parameters are consistent with the parameters obtained for the fit in the polar region in the reaction $K^+n \to K^+\pi^-p$. There is thus no evidence for any $K^0\pi^+\pi^-$ peak on the low-mass side of the $K^*(1420)$, and hence the $K_N^*(1370)$ has no strong three-body decay mode and probably is not associated with the structure in the Q at about this mass.

Discussion of the $J^P = 0^+$ hypothesis. The main effect observed here is the striking change in the character of the decay angular distribution at a mass of about 1.4 GeV. The distributions in ϕ, the decay azimuth in the Jackson frame, are consistent with being flat throughout the $K^*(1420)$ region, as they are expected to be for pion-exchange processes.

If we assume pion exchange and normalize to the number of observed events in each mass region, we calculate an average of 356 ± 27 S-wave and 19 ± 6 D-wave events in the 1.3- to 1.4-GeV region, and 234 ± 20 S-wave and 191 ± 22 D-wave events in the 1.4- to 1.5-GeV region. The amount of D-wave in the 1.3- to 1.4-GeV region is entirely consistent with that expected from the tail of a Breit-Wigner centered at 1440 MeV with width 100 MeV. Although the hypothesis of S- and D-waves results in an expected angular distribution symmetric about $\cos\theta = 0$, it is clear from Fig. 34

that the data is asymmetric. Aside from the effects of the crossing N^* bands, an admixture of as little as 1% P-wave to the S- and D-waves is sufficient to explain the observed asymmetry in this region completely.

We have also performed a similar analysis on the neighboring (K, π) mass regions assuming S- and P-waves in $M(K, \pi) < 1.3$ GeV. In Fig. 37 the number of S-wave events in each region are plotted as a function of $K\pi$ mass. The rise in the S-wave in the region 1.3 to 1.4 GeV is more than four standard deviations above the level in the two neighboring regions. The data thus consistent with a D-wave resonance of $M = 1439$ MeV, $\Gamma \approx 105$ MeV, $K^*(1420)$ and an S-wave resonance of $M = 1370$ MeV, $\Gamma < 150$.

The apparent absence of a three-body decay mode for $K_N^*(1370)$ mentioned above might be taken as evidence favoring the $J^P = 0^+$ interpretation since such a resonance cannot decay into three pseudo-scalars.

Discussion of the $J^P = 1^-$ hypothesis. The data in the region 1.3 to 1.4 GeV may also be fitted entirely with S- and P-waves, ignoring any D-wave tail of the $K^*(1420)$, with an average of 247 ± 40 S-wave and 128 ± 20 P-wave events. The asymmetry in this region requires the presence of at least a small admixture of P-waves; however, because of the intrinsic ambiguity between a P-wave and an S-D interference term, the actual amount of P-wave present is unknown. Thus there is no conclusive evidence for a resonant P-wave, although this possibility cannot be ruled out. Antich et al.[25] have previously suggested the presence of a $J^P = 1^-$ state, or at least an increase in the 1^- contribution to background, in the vicinity

of the $K^*(1420)$. These authors observed an asymmetry in the decay distribution of the $K^+\pi^-$ system in the reaction $K^+p \to K^+\pi^- \Delta^{++}$ at 5.5 GeV/c, from which they inferred the presence of P-wave and D-wave interference. In addition, the presence of a large S-wave signal in the region of the dominant D-wave has been observed at the $K^*(1420)$ in the similar reaction $K^+p \to K^+\pi^- \Delta^{++}$ at 9 GeV/c,[26] and at the f^0 in the reaction $\pi^+p \to \pi^+\pi^- \Delta^{++}$ at 8 GeV/c,[27] although in neither case was there strong evidence for an appreciable P-wave amplitude.

Discussion of the $J^P = 2^+$ hypothesis. If the $K_N^*(1370)$ were $J^P = 2^+$, its spin density matrix elements have been calculated by the method of moments to be $\langle \rho_{00} \rangle = 0.45 \pm 0.05$, $\langle \rho_{11} \rangle = 0.23 \pm 0.02$, and $\langle \mathrm{Re}\, \rho_{1-1} \rangle = -0.06 \pm 0.05$. The other spin density matrix elements e.g., ρ_{22}, are consistent with zero. As in the $J^P = 0^+$ case, the expected angular distribution is symmetric in $\cos\theta$, and therefore a small P-wave background must be invoked to explain the asymmetry. The angular distribution, folded about $\cos\theta = 0$ to eliminate the asymmetry, may be fitted with the distribution expected from the spin density matrix elements, but the confidence level for this fit is less than 5%. However, this fit may be markedly improved by the addition of a substantial S-wave background. Furthermore, the expected distribution in the Treiman-Yang angle, ϕ, differs only weakly from isotropy, and within the present statistics, no discrimination between the various hypotheses may be made on the basis of the distribution. The similarity of the t-distributions in the two regions (Figs. 35a, b) suggests similar production mechanisms and argues to some extent against the substantial vector exchange,

which is required to explain the observed angular distribution with a $J^P = 2^+$ object.

$K^*(1420)$ Branching Ratios

A clear $K^*(1420)$ signal is present in both the $K^+n \rightarrow K^+\pi^-p$ and $K^+n \rightarrow K^0\pi^+\pi^-p$ final states. (See Figs. 17 and 21.) The three-body decay of $K^*(1420)$ has limited statistics, but it has the advantage of being free from Q^+ background which is so overwhelmingly produced in non-charge exchange reactions. In order to determine the three-body to two-body ratio, we have to determine the $K^*(890)\pi/K\rho$ branching ratio of the three-body decay. The number of $K^*(1420)$ resonance events was obtained by fitting the mass spectra to a Breit-Wigner line shape and a polynomial background.

In Fig. 38 we show the $K^*(1420)$ decay Dalitz plot and $K^0\pi^+, \pi^+\pi^-$ invariant masses for the $K^*(1420)$region. The outstanding feature of the Dalitz plot is the large accumulation of events in the $K^*(890)$, ρ overlap region. This concentration is a result of the $\sin^2\theta$ helicity angular distribution of the vector mesons decay from a parent $J^P = 2^*$ meson.

Apart from this, there is the possibility of $K^*(890)$, ρ interference which might enhance or deplete the events in the overlap region. With the statistics available in this experiment, we cannot determine whether any interference effect is present.

To determine the relative amount of $K^*(890)$, ρ we have fitted the decay Dalitz plot of the $K^*(1420)$ region by a maximum-likelihood method with the following probability density:

$$|M|^2 = \epsilon\,|M_{1420}|^2 + (1-\epsilon)\,|M_{back}|^2,$$

where

$$|M_{1420}|^2 = \alpha_1 \frac{|f_{BW}(K^*)|^2 \sin^2\theta_{K^*}}{\Sigma\int |f_{BW}(K^*)|^2 \sin^2\theta d\phi} + \alpha_2 \frac{|f_{BW}(\rho)|^2 \sin^2\theta_\rho}{\Sigma\int |f_{BW}(\rho)|^2 \sin^2\theta_\rho d\phi},$$

$$|M_{back}|^2 = \beta_1 \frac{|f_{BW}(\rho)|^2}{\Sigma\int |f_{BW}(\rho)|^2 d\phi} + \beta_2 \frac{|f_{BW}(K^*)|^2}{\Sigma\int |f_{BW}(K^*)|^2 d\phi} + \frac{1-\beta_1-\beta_2}{\Sigma\int d\phi},$$

ϵ is the fraction of $K^*(1420)$ resonance above background,

α_1, α_2 are the branching fraction of $K^*(890)\pi$, ρK respectively for $K^*(1420)$ resonance decay,

β_1, β_2 are the brancing fractions of $K^*(890)\pi$, ρK for the background under the $K^*(1420)$,

$\theta_{K^*}, \theta_\rho$ are the helicity angle of the $K^*(890)$ and ρ respectively,

$$|f_{RN}| = \frac{m}{q} \frac{\Gamma}{(m^2 - m_0^2) + m^2\Gamma^2},$$

$$\Gamma = \Gamma_0 (q/q_0)^{2\ell+1},$$

$m_{K^*} = 890$ MeV, $\Gamma = 50$ MeV,

$M_\rho = 760$ MeV, $\Gamma = 130$ MeV.

The value of ϵ was determined from a fit to the three-meson mass spectra. The result of the fit was $\epsilon = .67$.

The values of β_1, β_2 were determined by fitting the region adjacent to the $K^*(1420)$ to a background amplitude only, $\epsilon = 0$.

The results were $\beta_1 = 0.6$, $\beta_2 = 0.3$. Then a fit of the decay Dalitz plot was performed to give the following values

$$\alpha_1 = .76 \pm .1,$$
$$\alpha_2 = .24 \pm .1.$$

In comparing the $K^*(1420)$ produced in the reactions $K^+n \to K^+\pi^-p$ and $K^+n \to K^0\pi^+\pi^-p$, we must avoid the problems caused by the second object observed on the low side of the $K^*(1420)$ in the $K^+\pi^-p$ final state. To this end we have calculated the branching ratios in two ways. One, we restricted our events to the region above 1400 MeV in both the $K^+\pi^-p$ and $K^0\pi^+\pi^-p$ final states. Thus we eliminated most of the events associated with the second object at low $K\pi$ mass. Two, ignoring the object at 1370 MeV, we evaluated the branching ratios of all events in the $K^*(1420)$ peaks.

The three-body to two-body branching ratio is given by the following equations:

$$R\left(\frac{K\pi\pi}{K\pi}\right) = \frac{9/4\ f_{K^*\pi} + 9/3\ f_{k\rho}}{3/2\ f_{k\pi}}$$

where $f_{K^*\pi}$, $f_{K\rho}$, $f_{K\pi}$ are the observed branching ratios. The fractions 9/4, 9/3, and 3/2 are the Clebsch-Gordan coefficients. The results obtained are

	$K\pi\pi$/all	$K^*\pi/K\pi$
$M > 1.4$	$.47 \pm .025$	$.88 \pm .04$
$M < 1.4$	$.40 \pm .03$	$.68 \pm .04$

The branching ratios $K^*(890)/K$ obtained in this experiment are lower in magnitude than results obtained in recent experiments by

Bishop et al.[28] and Bassompierre et al.[29]; they reported a ratio of $R(K^*\pi/K\rho) = .93 \pm .11$ and $.9 \pm .2$, respectively. Another experiment done by Aguilar-Benitz[30] et al. on the charge-symmetric reaction $K^- p \to K^-\pi^+ n, \bar{K}^0\pi^+\pi^-$ obtained a ratio $R(K^*\pi/K\rho) = .44 \pm .09$. We note that our results are consistent with the prediction of unbroken SU(3) symmetry.[31] The ratio $K\pi$: $K\rho$ is expected to be 50: 16: 7. Our results are 50: 33: 4.

F. Interference Effects at $M(K^+, \pi^-) \approx 1.85$ GeV

From the Dalitz plot (Fig. 13) and the scatter plot of $\cos\theta$ vs $M(K^+, \pi^-)$ (Fig. 18) we see that in addition to the $K^*(890)$, the $K^*(1420)$, and the low mass enhancement, there is additional structure at

$$M(K^+, \pi^-) \approx 1.85 \text{ GeV}. \quad [M^2(K^+, \pi^-) \approx 3.4 \text{ (GeV)}^2].$$

In the scatter plot, the structure is a concentration of events in the region $-.8 < \cos\theta < -.2$ at this mass region. In Fig. 17b we show the $M(K^+, \pi^-)$ mass projection for events with $t' < .2$ $(\text{GeV}/c)^2$. Besides the $K^*(890)$ and $K^*(1420)$, a clear broad enhancement is seen at $M(K^+, \pi^-) \approx 1.85$ GeV.

In Fig. 20 we show a distribution of $N\langle Y_\ell^0 \rangle$ as a function of $M(K, \pi)$ mass for all events with $t' < .2$ $(\text{GeV}/c)^2$. In the region $M(K^+, \pi^-) \approx 1.85$ GeV we observe a substantial increase in the values of $\langle Y_3^0 \rangle$ and $\langle Y_4^0 \rangle$. These increases occur over a mass range of about 150 MeV. In addition, $N\langle Y_6^0 \rangle$ begins to show significant non-zero value at this mass region. There is no evidence for an appreciable deviation from zero by $N\langle Y_\ell^0 \rangle$ where $\ell > 6$ for $K\pi$ masses < 2 GeV. Thus, if we consider only waves with $j \leq 3$, these sharp

increases are most naturally attributed to the interference of a rapidly increasing F-wave amplitude at a Kπ mass value of about 1.85 GeV, with waves of opposite parity; e.g., S- and D-waves.

Since the existence of F-wave in this mass region appears to be necessary, we may further investigate this effect with a judicious cut on the angular distribution to enhance the F-wave signal. Since $|Y_3^0|^2$ has zeroes at $\cos\theta = 0$ and $\cos\theta = \pm .775$ and reaches maximum at $\cos\theta = \pm 45$ and $\cos\theta = \pm 1$, we have divided the data into four regions in $\cos\theta$ as follows: a) $\cos\theta < .775$, b) $0 < \cos\theta < .775$, c) $-.775 < \cos\theta < 0$, d) $-1 < \cos\theta < -.775$. The resulting distributions are shown in Figs. 40a, b, c, d. The outstanding feature of this distribution is a mass enhancement at $M(K, \pi) \approx 1.85$ GeV with a width of 300 MeV/c in Fig. 40c. In Fig. 39 we show the $\cos\theta$ distribution for the four mass regions of $M(K, \pi)$: a) 1.5- 1.6 GeV, b) 1.6- 1.75 GeV, c) 1.75- 2 GeV, d) 2- 2.25 GeV. The change in angular distribution across this mass region is striking. The smooth curve in each figure is the result of a fit to the sum of Legendre polynomials up to the sixth order; i.e., $\sum_{n=0}^{N_{max}} a_n P_n(\cos\theta)$, where $N_{max} = 6$. The χ^2 and resulting parameters are shown in Table I. With the present statistical accuracy we cannot determine with precision the relative amounts of each wave present.

It should be noted that in the angular distributions of Fig. 39, the large forward peak is a consequence of the strong production of low-mass N^*'s. It might appear that some or all of this contribution should be considered as a background to Kπ scattering which ought to be subtracted out. However, the duality picture, as applied by Chew and Pignotti,[41] regards scattering in this reaction as dual to N^* and argues against such a subtraction. Since extrapolation to the

pion pole should in principle give the correct Kπ scattering distribution, we have examined the t-dependence of the ratio of the forward peak to the remainder of the angular distribution in this Kπ mass region. We find that there is no significant variation of this ratio with t', for $|t'| < 0.2$ $(GeV/c)^2$, consistent with the view that the angular distributions of Fig. 39 in fact represent Kπ scattering.

We have also fitted the angular distribution of Fig. 39c by using only the region $\cos\theta < 0.7$ to a sum of Legendre polynomials, and have found excellent agreement with the results of the fit to the entire distribution; i.e., the forward peak is reasonably well reproduced. However this truncated distribution may also be fitted with reasonable χ^2 with a sum of Legendre polynomials only up to the fourth order; i.e., no F-wave is required. In this case, however, the predicted forward peak is only about one-fourth of the observed peak, and thus the bulk of the events in this forward peak would not reflect Kπ scattering. Such a view would contradict the notion of duality discussed above.

It must be emphasized that if the L meson, as seen in a reaction like $K^+p \to K^+\pi^+\pi^-p$, is in fact produced by a diffraction process, as is generally supposed (and hence has unnatural spin-parity), then the enhancement observed in this charge-exchange reaction cannot be the L meson.[32] Preliminary results from a study of the K^+d reaction at 9 GeV/c showing an effect similar to the one observed here have been reported by the Purdue-Davis collaboration.[42]

In conclusion we have observed a rapid change in the Kπ scattering angular distribution in the mass region around 1.85 GeV. This effect can be most simply interpreted in terms of a rapid increase of an F-wave amplitude, which interfere with several other waves

present. If interpreted as a resonance, this $J^P = 3^- K^*$ could belong to the same SU(3) octet as the g-meson. Because of the strong interference effects observed in this experiment we cannot obtain precise values for the mass and width.

TABLE I

	1.5-1.6 GeV	1.6-1.75 GeV	1.75-2GeV	2-2.25 GeV
(A_1/A_0)	2.21 ± .04	1.25 ± .12	1.73 ± .07	2.2 ± .06
(A_2/A_0)	2.84 ± .07	2.27 ± .11	2.62 ± .08	2.99 ± .07
(A_3/A_0)	2.63 ± .09	1.18 ± .19	2.76 ± .10	3.02 ± .08
(A_4/A_0)	1.89 ± .11	.99 ± .06	1.64 ± .12	2.29 ± .10
(A_5/A_0)	1.00 ± .10	.04 ± .17	.94 ± .10	1.46 ± .09
(A_6/A_0)	.26 ± .10	.29 ± .219	.72 ± .11	.46 ± .10
χ^2/DOF	25/13	15/13	10/13	20/13

G. Comparison with $K^+p \to K^+\pi^-\Delta^{++}$ Reactions

There have been a large number of bubble chamber experiments which studied the reaction $K^+p \to K^+\pi^-\Delta^{++}$.[26] The reaction has the same general properties we found in the reaction $K^+n \to K^+\pi^-p$. Apart from the difference in coupling constant for the exchange particle at the baryon vertex, the two reactions are identical. There is, however, an important difference: the ratio of the $K^*(890)/K^*(1420)$ production cross sections.

$\frac{K^*(890)}{K^*(1420)} \approx 1$ in K^+n reactions; R $\frac{K^*(890)}{K^*(1420)} \approx 2$ in K^+p reactions.

But there is an important kinematical distinction between the two reactions which we believe can explain some of the difference.

In Fig. 41 we show the Chew-Low boundary for the reactions a) $K^+p \rightarrow K^+\pi^- \Delta^{++}$, where the mass of Δ^{++} is taken as 1240 MeV. The accessible region for the two reactions is nearly the same as low $K\pi$ mass, but as we go to higher mass the difference becomes very pronounced. Since the dominant exchange in the production of K^*'s in these charge exchange reactions is pseudo-scalar, this difference has an important effect on the cross-section. To illustrate this point, we took the events in the $K^+n \rightarrow K^+\pi^-p$ channel and separated them into events produced with t accessible to the $K^+p \rightarrow K^+\pi^- \Delta^{++}$ reaction and events with inaccessible t. (See Fig. 42.) It is clear that at low $K\pi^-$ mass the difference is insignificant, but as we go to higher mass this difference becomes increasingly important. We note that if we restrict ourselves to events in the accessible t region, the $K^*(890)/K^*(1420)$ ratio is in good agreement with the $K^*(890)/K^*(890)/K^*(1420)$ ratio found in Δ^{++} reactions. Since cross section for K^{*0} production tends to fall off rapidly with increasing energies and usually are produced in the low-t region, the neutron target seems to be better than the proton for a search for mesons in the high-mass regions.

H. N^* Production in the Reaction $K^+n \rightarrow K^+\pi^-p$

The $p\pi^-$ invariant mass distribution in the reaction $K^+n \rightarrow K^+\pi^-p$ is dominated by low mass, $M(p\pi^-) < 1.8$ GeV. (See Fig. 16.) In Fig. 15 we show the Chew-Low plot t_{K-K} vs $M^2(p\pi^-)$ and note a large low mass $p\pi^-$ band produced primarily at low t but extending to higher t values as well. In order to study possible structure in the $p\pi^-$ mass enhancement we plot $M(p, \pi^-)$ for three different t' regions: (see Fig. 43) a) $t' < .1(\text{GeV}/c)^2$, b) $.1(\text{GeV}/c)^2 < t' < .4(\text{GeV}/c)^2$, c) $t' > .4(\text{GeV}/c)^2$.

The low-t' region is dominated by a low $p\pi^-$ enhancement centered at $M(p, \pi^-) \approx 1340$ MeV; this is well below the first known I = 1/2 isobar. A similar effect has been seen in a $\pi^+ p$ experiment at 8 and 16 GeV/c.[33] As t' increases, the average value of $M(p, \pi^-)$ increases. At large t' we can see a separation between $N^*_{1/2}(1550)$ and $N^*_{1/2}(1668)$.

To study the decay angular distribution for the $p\pi^-$ system we plot in Fig. 44 the Y_ℓ^0 moments of $p\pi^-$ decay. We note that the angular distribution changes rapidly across the low $p\pi^-$ enhancement. For $M(p, \pi^-) < 1.8$ GeV, only S-P waves are necessary to describe the data. But at $M(p, \pi^-) > 1.8$ GeV higher waves become important.

The $p\pi^-$ mass peak at 1.3 GeV cannot be attributed to Δ^0 production. Using the isotropic spin relation and the result of the $K^+p \to K^0\Delta^{++}$ experiment at 12.7 GeV/c[45], we estimate the cross section for the reaction

$$K^+n \to K^+\Delta^0 \Big|_{\to p\pi^-}$$

in the region of interest ($t' < .2$ (GeV/c)^2) to be 4-5 μb, which can explain only 70 of the peak's several hundred events.

V. COHERENT PRODUCTION OF $K^+\pi^+\pi^-$.

A. Selection of Events, $K^+\pi^+$ Ambiguity

The film has been scanned for all events which have three-prong or four-prong topologies. The three-prong events have assigned to them a particle of zero momentum in the initial approximation to the kinematic fit. For the deuteron hypothesis $K^+d \rightarrow K^+\pi^+\pi^-$ this missing recoil deuteron has momenta errors of $\Delta p_x = \Delta p_y = 40$ MeV/c and $\Delta p_z = 50$ MeV/c assigned to it in the initial approximation. These errors reflect the fact that a deuteron momentum less than 110 MeV/c does not leave a visible track in the bubble chamber.

A total of 5834 events satisfying the hypothesis $K^+d \rightarrow K^+\pi^+\pi^-d$ found in both three- and four-prong topologies. The treatment of invisible deuteron in the three-prong events and the problem identifying coherent events are discussed in Chapter II. All coherent events with χ^2 confidence level greater than .1% were accepted.

At high incident momenta, this reaction has a disadvantage: it is often difficult to determine the correct premutation of masses among the outgoing positive meson tracks. At our energy, 57% of the four-prong events and 75% of the three-prong events remain ambiguous after kinematic fitting. We point out that the typical momentum of the outgoing meson tracks in 3 to 4 GeV/c; thus, ionization information is of no help in resolving this ambiguity.

The ambiguous events can be separated into two categories. The class of events where the chi-square difference between the two ambiguous hypotheses is large, defined here as $|\chi_1 - \chi_2| > 3$, or small, $|\chi_1 - \chi_2| < 3$. The events with large χ_2 difference constitute 22% of the four-prong events and 11% of the three-prong events. The remaining 35% of the four-prong events and 64% of the three-prong

events have chi-square difference smaller than three. For the events with the large χ^2 difference, selecting the events with lower χ^2 chooses the right interpretation for nearly all events.

In Fig. 45a, b we show the $D\pi^+$ and the $K^+\pi^-$ mass plots for unambiguous events. By and large these events correspond to π^+ mesons with fairly low laboratory momenta. In view of the fact that the D is very slow in the laboratory system, as required by the low momentum transfer for coherent events, it follows that these events correspond to low $D\pi^+$ masses. The mass is dominated by $K^*(890)$ production, but there is also a clear $K^*(1420)$ signal. In Fig. 46a, we show the mass plot for the events with χ^2 difference greater than three. Note that the average $D\pi^+$ mass has shifted to a higher mass, as expected. In Fig. 46b, we show the two-dimensional plot $M_1(K_1^+, \pi^-)$ vs. $M_2(K_2^+, \pi^-)$, where the subscripts 1 and 2 refer to the accepted and rejected hypotheses respectively. In Fig. 46c, d we show the $M(K^+, \pi^-)$ projections of both selected and rejected hypotheses. We note that the sample of selected events is dominated by $K^*(890)$ production while only a small $K^*(890)$ signal occurs in the rejected events. These come mostly from the overlap region, for which both interpretations give a $K^*(890)$. Thus large χ^2 difference provides a good selection criterion.

In order to resolve the ambiguity for events with small χ^2 difference, we utilize the fact that the $K^+\pi^-$ mass is dominated by $K^*(890)$ production and, to a lesser extent, by $K^*(1420)$. We thus select events according to the following criteria, where we designate events with $M(K^+, \pi^-)$ 890 to 940 MeV as $K^*(890)$ and $M(K^+, \pi^-)$, (1320-1480) MeV as $K^*(1420)$:

a) If one interpretation falls in the $K^*(890)$ band and the other does not, we select the former interpretation as the correct one for this event.

b) If one interpretation falls in the $K^*(1420)$ band and the other does not fall in either the $K^*(890)$ band or the $K^*(1420)$ band, we select the former.

c) If both interpretations fall in the $K^*(890)$ band, we select the one with $M(K^+\pi^-)$ closer to 890 MeV.

d) If both interpretations have a $K^*(1420)$, we select the one with $M(K^+\pi^-)$ closer to 1420 MeV.

e) Otherwise, we select the interpretation with $M(K^+\pi^-)$ closest to 890 MeV.

In Fig. 47a we show the $D\pi^+$ invariant mass plot for events selected as above. We note that the average value of $D\pi^+$ mass has moved higher; i.e., the ambiguity problem is a strong function of the π^+ momentum. Thus as the π^+ momentum increases, the ambiguity problem becomes more serious.

In Fig. 47b we show the two-dimensional plot $M_1(K^+, \pi^-)$ vs. $M_2(K^+, \pi^-)$. Here again one combination (M_1) corresponds to the accepted interpretation, while the other (M_2) corresponds to the rejected interpretation. In Fig. 47c, d we show the mass projections of the $K^+\pi^-$ mass for the two hypotheses. Note that the selected events are dominated by $K^*(890)$ and to a lesser extent by $K^*(1420)$ production, while, as expected, the rejected events have no $K^*(890)$ or $K^*(1420)$ signal.

We can estimate the number of mis-assigned events by the size of the dip in the $M_2(K, \pi)$ distribution. We estimate this mis-assignment to be 15% in this subsample of events.

B. General Features of the Data

The cross section for the reaction $K^+D \rightarrow K^+\pi^+\pi^-D$ is 331 ± 8 μb. The errors quoted are purely statistical. The error in the cross section is dominated by the selection criteria used to separate $K\pi\pi d$ and $K\pi\pi pn$ final states. We estimate the systematic error to be 30 to 40 μb. In Fig. 48 we show the Chew-Low plot t_{d-d} vs. $M^2(K, \pi, \pi)$. The events are concentrated at low t. In Fig. 49 we show the differential cross section, $\frac{d\sigma}{dt}\Big|_{KD \rightarrow K\pi\pi D}$ for all events in the reaction. The data can be described by an exponential function of the form $e^{-\alpha t}$ with $a = 25 \pm 2\ (GeV/c)^2$. In Fig. 50 we show the three-meson invariant mass plot $M(K, \pi^+, \pi^-)$ for all events in the reaction. The shaded region is for events left after $D\pi^+$ in the D^{*++} region are removed $[M(D, \pi^+) < 2320\ MeV]$. The reaction is dominated by low $K\pi\pi$ invariant mass $M(K, \pi, \pi)$ 1.5 GeV, but there are a substantial number of events in the L region, $M(K, \pi, \pi) \approx 1.7$ GeV.

In Fig. 51 we show the $M(K, \pi, \pi)$ invariant mass plot for all events. The shaded region represents the four-prong events, events with visible detuerons. It is clear that three-prong events, those with an invisible deuteron, make an important contribution only in the Q region but do not make a contribution in the high mass region. This is expected, since three-prong events are restricted to the very low t region $t < .015\ (GeV/c)^2$, and the Chew-Low boundary makes the high-mass region inaccessible to events with such low t.

In Fig. 52 we show the various two-body invariant mass distributions. In Fig. 52a we show the $K^+\pi^-$ invariant mass distribution. The distribution is dominated by $K^*(890)$. A clear signal can be seen at K*(1420). In Fig. 52b we show $D\pi^+$ invariant mass plot, which is

dominated by low-mass $D\pi^+$, D^{*++} production. In Fig. 52c, d, e, f we show the $K^+\pi^+$, $D\pi$, DK^+, and $\pi^+\pi^-$ invariant mass distribution. There is no distinctive structure in any of these distributions. In particular, the $D\pi^-$ shows no significant D^{*0} production. This effect will be discussed in more detail in Section Vd. The lack of ρ signal in the $\pi^+\pi^-$ system is partly due to the fact that the low $K\pi\pi$ mass restricts $\pi^+\pi^-$ invariant mass to be low. Since this channel is dominated by low $K\pi\pi$ mass, it restricts the $\pi\pi$ mass to be mainly below the ρ mass. A more detailed analysis done in Section Vc reveals that there is ρ production in this channel.

In Fig. 53 we show the two-dimensional plot $M^2(K, \pi, \pi)$ vs. $M^2(D, \pi^-)$. Clear $Q+$, D^{*++} bands can be seen. We note that a clear concentration of events in the L region can also be seen, especially at the overlap region with low $D\pi^+$ mass. In the next few sections we will discuss $Q+$, D^{*++}, and L production in more detail.

C. Q^+ Production

The reaction $K^+D \to K^+\pi^+\pi^-D$ is dominated by the production of low $K\pi\pi$ mass. (See Fig. 50.) To investigate the possibility of structure in the Q region, we plot the $K\pi\pi$ mass distribution with D^{*++} removed. (See Fig. 50.) We note that the removal of the D^{*++} has little influence on the shape of the Q, but the removal of D^{*++} has a strong effect on the high $K\pi\pi$ mass region near the L region. In Fig. 54 we show the $K^*(890)$, π distribution. The shaded region corresponds to events with D^{*++} events removed. Their removal has little effect on the distribution. Note that the distribution is inconsistent with a single Breit-Wigner line shape. The mass distribution can be fitted to a two Breit-Wigner line shape with the following para-

meters: $m_1 = 1240 \pm 10$ MeV, $\Gamma_1 = 180 \pm 20$ MeV,

$m_2 = 1360 \pm 10$ MeV, $\Gamma_2 = 200 \pm 20$ MeV.

These values are consistent with those observed in high-energy K^+p experiments[34]. But we notice that the values for m_1, m_2 are lower than the one obtained in the K^+p experiments where $m_1 \approx 1260$ to 1280 MeV, $m_2 \approx 1380$ - 1400 MeV.

Reactions on deuterium are characterized by a steep momentum transfer distribution. This effect, coupled with the Chew-Low boundary, can have an important effect on the mass of the three mesons. If the production differential cross sections differ as a function of $K\pi\pi$ mass, it can result in serious differences between the mass spectra observed in K^+d or K^+p experiments. In Fig. 55 we show the $K\pi\pi$ mass for all events weighted by the deuteron form factor. $1/H(t)$. Thus events with low t have a lower weight than events with higher t. This correction takes into account both the differences in production differential cross section introduced by deuteron break-up and the Chew-Low boundary effect. Weighting the events shows that the average $K\pi\pi$ mass moves higher and is now practically identical to the K^+p mass spectra in the Q region. Note that weighting has a proportionally greater effect on events with large $K\pi\pi$ mass.

To investigate the production mechanism as a function of the Q mass further, we plot the differential cross section $d\sigma/dt$ for events in four sections of the Q^+ regions: a) $M(K, \pi, \pi)$ 1-1.2 GeV, b) $M(K, \pi, \pi)$ 1.2-1.3 GeV, c) $M(K, \pi, \pi)$ 1.3-1.4 GeV, d) $M(K, \pi, \pi)$ 1.4-1.5 Gev. The differential cross sections are shown in Fig. 56. A fit of the differential cross section to a function of the form e^{-Bt} yields the

values of B in $(GeV/c^{-2}$ for the four regions as follows: a) $B = 29 \pm 1.5$, b) $B = 27.5 \pm 1.5$, c) $B = 25 \pm 2$, d) $B = 26 \pm 2$. It appears that the events in the low $K\pi\pi$ mass regions have slightly steeper differential cross sections than those in the higher $K\pi\pi$ mass regions. The same effect has been noticed in K^+p experiments. The cross section for Q^+ production with $M(K^+, \pi^+, \pi^-)$ 1-1.5 GeV is 212 $\pm$ 15 μb; the cross section for the $K^{*0}(890)\pi^-$ in the Q^+ region is 150 $\pm$ 10 μb.

The absence of Q^+ decay into two mesons, the lack of Q^+ production in charge exchange reactions, and the slope of four-momentum transfer distribution $\frac{d\sigma}{dt} \propto e^{-28}$ all suggest that the Q is produced by diffraction dissociation. Thus we expect the Q to belong to the spin-parity series 0^-, 1^+, 2^-, etc.

In order to study the decay angular distributions we restrict ourselves to the subsample of $K^*(890), \pi$ events only.

In the following paragraphs we will discuss the angular distributions observed for $K^*(890), \pi$ events in the following four regions in $K\pi\pi$ mass: a) 1.1.2 GeV, b) 1.2-1.3 GeV, c) 1.3-1.4 GeV, and d) 1.4-1.5 GeV. The shaded regions in cosine distributions correspond to the subsample of events in which the K^+, π^+ ambiguity were resolved on the basis of K^+, π^- mass, as discussed in Section Va. These ambiguous events are mainly events in the K^*, ρ overlap region, events with a fast π^+. The curves on the angular distribution plots are a result of a fit to the function

$$f(\cos\theta) = a_0 + a_1 P_1(\cos\theta) + a_2 P_2(\cos\theta).$$

The numerical results of the fit are given in Table II.

Table II

		$\cos\theta$ KK	$\cos\theta$ K, K^*	$\cos(\beta)$	$\cos(\xi)$
A	(a_1/a_0)	.52 ± .07	.24 ± .06	.007 ± .05	-.23 ± .06
	(a_2/a_0)	1.72 ± .05	.024 ± .07	-.75 ± .07	07 ± .08
	χ^2/DOF	17/17	12/17	11/17	12/17
B	(a_1/a_0)	.46 ± .06	-.35 ± .06	.007 ± .04	-.34 ± .06
	(a_2/a_0)	1.5 ± .06	.4 ± .07	-.88 ± .05	.431 ± .08
	χ^2/DOF	18/17	19/17	15/17	10/17
C	(a_1/a_0)	.48 ± .07	.57 ± .07	-.015 ± .07	-.4 ± .07
	(a_2/a_0)	1.39 ± .07	.53 ± .08	-.73 ± .06	.48 ± .86
	χ^2/DOF	15/17	28/17	29/17	14/17
D	(a_1/a_0)	.3 ± .1	-.6 ± .1	-.07 ± .06	.45 ± .1
	(a_2/a_0)	1.4 ± .06	.55 ± .1	-.7 ± .07	.4 ± .11
	χ^2/DOF	42/17	25/17	35/17	13/17

Decay analysis. In order to study the decay features of the Q^+ a function of $M(K, \pi, \pi)$, we have divided the Q region into four parts: a) 1 to 1.2 GeV, b) 1.2 to 1.3 GeV, c) 1.3 to 1.4 GeV, and d) 1.4 to 1.5 GeV. In Fig. 55 we show the decay Dalitz plot for each region. A clear $K^*(890)$ band can be seen in each region. In regions b, c, and d, a concentration of events can also be seen clearly in the ρ band, especially in the $K^*(890)$, ρ overlap region. (See also the mass projections.) In Fig. 56 we show the $K^+\pi^-$ invariant mass distribution for each of the four regions in $M(K, \pi, \pi)$. All distributions are

dominated by $K^*(890)$ production.

In Fig. 57 we show the $\pi^+\pi^-$ invariant mass plot for each of the $M(K, \pi, \pi)$ regions. Note that some ρ signal can be seen as we move to higher $M(K, \pi, \pi)$. Because our selection criteria are biased in favor of $K^*(890)$ events, we do not think that this is a good sample of events for determining the exact $K^*(890)\pi/K\rho$ branching ratio of the Q^+. We have raised the possibility of a $K\epsilon$ decay mode of the Q earlier [35, 36]. The need for ϵ decay ($J^P = 0^+$) arises when one compares $R(K^0\pi^+\pi^0/K^+\pi^+\pi^-)$. Experimentally, a ratio of 1 is observed, while a factor of 2 would be derived from using I-spin relations. The discrepancy can be explained in terms of a $K\epsilon$ decay mode which contributes to the $K^+\pi^+\pi^-$ final state but not to the $K^0\pi^+\pi^0$D events, so we cannot compare the two samples in the present experiment. Thus our present data cannot support or reject the $K\epsilon$ decay mode of the Q^+.

Angular Distributions. To make a model-independent analysis of the spin-parity of the $K\pi\pi$ system as a function of mass, we have examined the angular distributions of the following angles.

a) $\cos\theta_{K,K}$ ϕ where θ, ϕ are defined as the Jackson decay angles of $K^*(890)$.

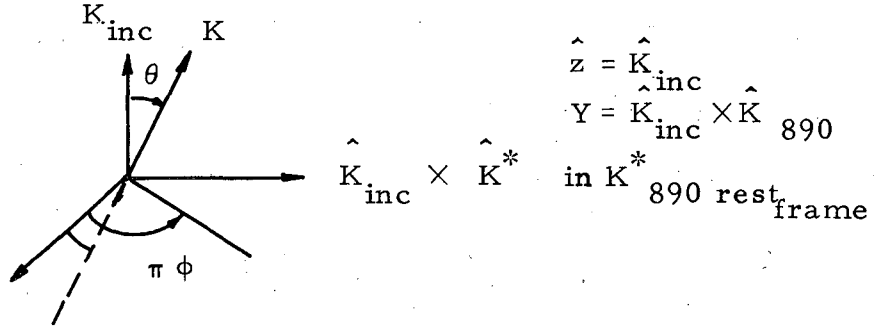

b) $\cos\theta_{K,K^*}$ where θ is defined as the Jackson decay angle of Q in the Q rest frame.

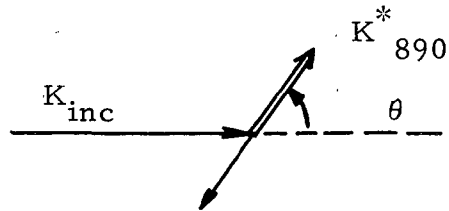

c) $\cos\beta$, ϕ are the decay angles between the normal to the K decay plane and the beam direction in the Q rest frame.

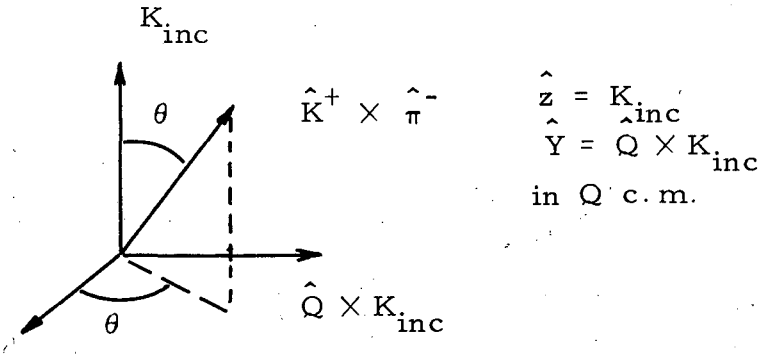

d) $\cos\xi$, where ξ is defined as the $K^*(890)$ helicity angle in the Q rest frame.

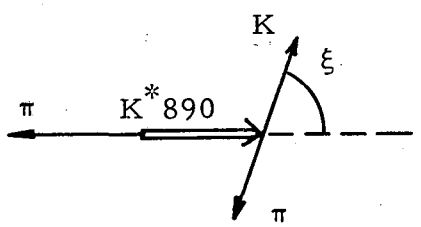

Assuming a given J^P value produced by a 0^+ exchange (Pomeranchuk exchange), the expected angular distributions are shown in Table III.

Table III

J^P	$\cos\theta_{K,K}$	$\cos\theta_{K,K^*}$	$\cos\beta$	$\cos\xi$
0^-	$1+3\sin^2\theta$	$1+3\sin^2\theta$	1	$\cos^2\xi$
1^+	$\cos^2\theta$	1	$\sin^2\beta$	1
2^-	$1+3\cos^2\theta$	$1+3\cos^2\theta$	$1-3\sin^2\beta+(9/4+K)\sin^4\beta$ *	$3+\cos^2\xi$

* K is a kinematical constant. See Ref. 43.

We note that by selecting $K^*(890)$ events we are also including ρ events from the K (890), ρ overlap region. These events contribute to different angular distributions in a biased fashion, and to determine the spin-parity one has to take this effect into account. The angular distributions are also particularly sensitive to the problem of K^+, π^+ ambiguity, and despite the fact that we believe our selection criteria to be good in 90% of the events, the misidentified events could lead to a bias in the angular distributions. To investigate the effect of ρ contamination in the angular distribution, we have examined the angular distribution for the subsample of events in the K^*, ρ overlap region. In the following section we discuss these effects on the different angular distributions.

In Figs. 60 and 61 we show the angular distribution in $\cos\theta_{K,K}$ and ϕ for the $K^*(890)$ decay. $\cos\theta, \phi$ are defined as the decay angles in the Jackson frame. The $\cos\theta$ distributions in all four regions in $K\pi\pi$ mass have a strong $\cos^2\theta$ component. The forward asymmetry exhibited by the distributions could be explained by the contribution of ρ events from the K^*, ρ overlap region. The distribution throughout the Q region is consistent with being pure 1^+, but we cannot exclude some 2^- terms. The ϕ distribution shown in Fig. 61 is consistent with being flat for the whole Q^+ region, as expected for a $J^P = 1+$ produced by 0^+ exchange.

In Fig. 62 we show the angle $\cos\theta_{K,K^+}$ which is the Jackson decay angle of the Q meson. A pure $J^P = 1^+$ is expected to have an isotropic distribution in $\cos\theta_{K,K^*}$. The $\cos\theta_{K,K^*}$ is largely isotropic at low $K\pi\pi$ mass but at high $K\pi\pi$ mass has a considerable backward asymmetry. From the shaded region we note that the asymmetry is associated with the ambiguous events. This is partly a reflection of the kinematic

effect of ambiguous events. Events with fast π^+ in the laboratory system are also events with backward K^* in c.m. We also note that ρ events will similarly tend to give a backward peak in this distribution. The asymmetry could also result from the presence of a 0^- background, where $0^- \rightarrow 1^- 0^-$ decay via a P wave and Y_1^0 term can interfere to produce the observed asymmetry. This angle is particularly sensitive to the ambiguity problem, and we do not believe the different effect can be separated.

In Figs. 62 and 64 we show the $\cos\beta$ and ϕ distribution for the normal to the $K\pi\pi$ decay plane. The distribution is strongly $\sin^2\beta$ throughout the Q^+ region. We note that this angle is not very sensitive to the ambiguity problem of $K^*\pi$, ρK decay of Q^+. Deviations from pure $\sin^2\beta$ in this angle, especially at high $K\pi\pi$ mass, are indicative of the presence of non 1^+ background, probably 0^- and/or 2^-. With present statistics, the relative contribution of each background term cannot be determined. The ϕ distribution is consistent with being flat, as expected for an unnatural parity series produced by Pomeranchuk exchange.

In Fig. 65 we show $\cos\xi$, the helicity decay angle of $K^*(890)$ in the Q rest frame. The distribution at low $K\pi\pi$ mass is consistent with being flat. At higher $K\pi\pi$ mass, the backward asymmetry is due to the excess of events in the K^*, ρ overlap region.

In conclusion, we note that the Q^+ produced off deuterium is mainly 1^+, but some evidence for $J^P = 0^-$ and/or 2^- background exists in this region. The K^+, ρ overlap and K^+, π^+ ambiguity problem make it difficult to determine the intensity of the non $J^P = 1^+$ background in this region.

Possible interpretations and conclusions. The fact that Q^+ is produced in coherent reactions confirms its I-spin assignment of $I = 1/2$. The production mechanism is believed to be the diffraction type, Pomeranchuk exchange. This is supported by the differential cross section distribution $(\frac{d\sigma}{dt} \propto e^{-28t})$ and spin-parity analysis of Q^+. The spin-parity of Q^+ is consistent with being $J^P = 1^+$ with 0^- and/or 2^- background. The Q decays predominantly into $K^*(890)\pi$. The $K\rho$ decay mode is important mainly at high Q regions.

Extensive work has been done attempting to understand the nature of Q. Is it a double peripheral process, a Deck effect, or is it a resonance or a cluster of resonances? As for the distinction between resonances and Deck effect, the concept of duality, as interpreted by Chew and Pignotti, suggests that they are identical. To explain a Deck type enhancement, a resonance must be present in this region. In high-energy K^+p experiments, in particular the 9-GeV/c experiment of Alexander et al[35] and the 10-GeV/c experiment of Barnham et al[36], significant structure was seen in the Q mass, which suggests the presence of at least two resonances in this region apart from K*(1420). We note that in our channel the $K^*(1420)$ contribution calculated from $K^+D \rightarrow K^0\pi^+D$ is consistent with being zero, and it cannot account for more than 20 to 30 events. A model proposed by G. Goldhaber[38] to explain the structure in the Q region suggests the presence of two interfering resonances in the Q region. The two states must have the same spin-parity to show interference effects on the mass plot. The quark model predicts the existence of two $J^P = 1^+$ states, $^3P_1$ and $^1P_1$. The physical 1^+ states can be a mixture of the two quark states and can also interfere through a common decay channel[40]. If we

denote the "unmixed" state as

$$K_A: J^{PC} = 1^{++}(^3P_1),$$
$$K_B: J^{PC} = 1^{+-}(^1P_1),$$

the physical states are related to the unmixed state by

$$|K_1^{++}\rangle = |K_A\rangle \cos\phi + |K_B\rangle \sin\phi,$$
$$|K_2^{**}\rangle = -|K_A\rangle \sin\phi + |K_B\rangle \cos\phi,$$

where ϕ is the mixing angle.

If the states were unmixed, $\phi \approx 0$. We would expect only K_1^{**} to be produced off deuterium. If ϕ is large, that is, maximum mixing, we would expect by both K_1^{**} and K_2^{**} to be produced in K^+D interactions, and the mass spectrum is expected to be similar to K^+p mass spectrum. In this experiment the $K\pi\pi$ mass spectrum is consistent with the one seen in K^+p experiments. This supports the notion of considerable mixing between the two K^{**} quark states.

D. D^* Production

In Fig. 50b we show the $D\pi^+$ invariant mass distribution where a clear low-mass $D\pi$ enhancement can be seen at $M(D,\pi) = 2150$ MeV, $\Gamma = 150$ MeV. We observe that this mass is consistent with the sum of a nucleon mass and the mass of the $\Delta^{++}(1238)$. In Fig. 58a we show a $\cos\theta$ distribution for events in the D^* region, $\left[M(D,\pi) < 2320 \text{ MeV}\right]$. Here θ is defined as the Gotfried-Jackson angle for a D^* resonance. The strong backward peaking is not characteristic of a resonance decay, as it requires a large number of partial waves. We conclude that the D^{*++} low-mass enhancement is not a well-defined resonance but rather a kinematical reflection of the reaction described in Fig. 58b. The reaction proceeds in two stages: 1) $K^+d \rightarrow K^+\pi^-\Delta^{++}n$, where the neutron is a spectator, and then (p, n) recombine to form a deuteron after the Δ^{++} decays.

In Fig. 59a, b we show the $\cos\theta$ and ϕ decay angular distributions

for $K^*(890)$ recoiling against the D^{*++}. The $\cos\theta$ angular distributions has a strong $\cos^2\theta$ component and the ϕ distribution is consistent with being flat. Both distributions indicate that the $K^*(890)$ is produced predominantly by pion exchange.

In Fig. 50d we show the $D\pi^-$ mass distribution. There is no evidence for strong D^{*0} production. The suppression of D^{*0} production can be understood if we assume that the process described in Fig. 58b dominates in D^{*++} production. A similar diagram producing D^{*0} will be suppressed by the ratio of the $K^+\pi^+$ and $K^+\pi^-$ elastic scattering cross sections. This is the ratio between an exotic and a resonant nonexotic channel -- a rather small number.

In Fig. 60 we show a differential cross section for the events $K^+D \to K^+\pi^-D^*$, where t is defined in 60a as t_{D-D} and in 60b as t_{D-D^*}. Both distributions can be fitted to a function of the form Ae^{-bt}, where $B = 18 \pm 2$ for t_{D-D} and $B = 14 \pm 2$ for t_{D-D^*}. Note that the value of B in Fig 55a is considerably lower than the value calculated for Q events (B = 29).

In Fig. 61 we show the $K\pi$ mass recoiling against D^{*++}. We observe a strong $K^*(890)$, $K^*(1420)$ production and note that the relative production of $K^*(1420)$ to $K^*(890)$ has increased compared to all events. (See Fig. 50a.)

In Fig. 62 we show the $K\pi\pi$ mass associated with D^{*++} events. The overlap between Q and D^* events is small, but as has already been mentioned, the low $D\pi$ mass events seem to be associated with L production. (See Fig 51) The cross section for D^{*++} production in $K^+D \to K^+\pi^-D^{*++}$ is $30 \pm 8\mu b(D^{*++} \to D\pi^+)$.

E. L^+ Production

In Fig. 53 we showed the two-dimensional correlation plot $M^2(K,\pi,\pi)$ vs. $M(D,\pi)$ in which L enhancement was seen to be associated mainly with low $D\pi$ mass. In Fig. 70 we showed $K\pi\pi$ events associated with D^{*++} events $\left[M(D,\pi) < 2.32\ \text{GeV}\right]$ where a clear L signal can be seen. In Fig. 71 we show the $K\pi\pi$ mass plot for events with $M(D,\pi) < 3\text{GeV}$ where a clear L signal can be seen. We fitted this distribution to a Breit-Wigner with constant background and have attained as the best parameter for the fit $M(K,\pi,\pi) \approx 1720$ MeV, $\Gamma \approx 190$ MeV. The concentratration of L levels at low $D\pi$ mass is not well understood. There are a number of possible explanations. One is that at low $D\pi$ mass $K^+\pi^+$ ambiguity is minimized. (see Section VA). Thus L, Q are well separated. At high $D\pi$ mass, problems of $K^+\pi^+$ ambiguity are more serious and might explain the smearing of the L signal. This is very unlikely as the effect is quite pronounced. The effect is probably real, and the excess of events at low $D\pi$ mass could be a result of the D^{*++} interference effect.

The concentration of L at low $D\pi$ mass can be a result of the following effect. Assuming L production is dominated by the multipheral diagram described in Fig 66b, the top vertex is dominated by $K^*(1420)$ and the bottom vertex is dominated by π^+D scattering. The deuteron has a higher probability of breaking up as $D\pi^+$ mass increases. The cross section for coherent L production is proportional to the product of the π^+D. cross section and the probability of the deuteron staying together. Since both cross section and break-up probability favor low $D\pi$ mass, L events are concentrated there.

It is interesting to note that $L^\pm$ production in the K^+p, K^-p

experiment seem to have a different cross section; L^- production cross section is larger than L^+.[32] The cross section for L^+, L^- is expected to be the same if L is produced by Pomeranchuk exchange. But if on the other hand L production is dominated by the Deck-type mechanism described in Fig. 66b, the difference between the L^+ and L^- cross sections can be explained in terms of the difference between π^+p, ρ^+p and π^-p, ρ^-p elastic scattering. To check this hypothesis, an accurate measurement of L^+, L^- cross section as a function of $p\pi^+$ or $p\pi^-$ mass respectively is needed.

L-decay. In Fig. 72 we show the decay Dalitz plot associated with the events in L region with low $D\pi$ mass, $\left[M(D,\pi) < 3 \text{ GeV}\right]$. In Fig. 65a we show the $K\pi$ invariant mass for these events. Clear $K^*(890)$ and $K^*(1420)$ bands can be seen in both plots. In Fig. 65b we show the $\pi^+\pi^-$ mass distribution for these L events. A clear ρ signal can be seen at $M(\pi,\pi) \approx 720$ MeV.

VI. THE REACTION $K^+D \to K^0\pi^+D$

A total of 133 events satisfying the hypothesis $K^+D \to K^0\pi^+d$, $K^0 \to \pi^+\pi^-$ were found in both one-prong plus vee (40%) and two-prong plus vee (60%) topologies. All events satisfying the multivertex seven constraint fit with chi-square probability greater than .1% were accepted as this hypothesis, provided that the invariant mass of the proton and neutron in the corresponding reaction $K^+d \to K^0\pi^+pn$ is less than 1886 MeV. Reliability of coherent fits is discussed in Chapter II, Section E.

In Fig. 73a, b, c we show the invariant mass for $D\pi^+$, DK^0, $K^0\pi^+$ systems. No evidence for structure can be seen in either $M(D, \pi^+)$ or $M(D, K^0)$ invariant mass. In particular, there is no evidence for D^{*++} production. In Fig. 73c we see a strong $K^*(890)$ signal in the K^0, π^+ invariant mass spectrum. There is little if any $K^*(1420)$ signal in this channel.

The cross section for $K^*(890)$ production in the reaction $K^+D \to K^*(890)D$ as $20 \pm 4\,\mu b$ after correcting for K^0 decay and $K^0\pi^0$ decay mode of $K^*(890)$. The $K^*(1420)$ cross section is consistent with being zero, and an absolute upper limit for $K^*(1420)$ production cross section is $8\,\mu b$ correcting for three-body decay mode and K^0 neutral decay. This corresponds to an upper limit of 30 $K^*(1420)$ events in the reaction $K^+D \to K^+\pi^+\pi^-D$.

In Fig. 74a we show the differential cross section for the reaction $\left.\frac{d\sigma}{dt}\right|_{KD \to K^*\,890D}$. If we parametrize the momentum transfer distribution in the functional form $\frac{d\sigma}{dt} \propto e^{Bt}$, a least-square fit to to the data points yields the slope $B = 17 \pm 2\ (\mathrm{GeV/c})^{-2}$ with $\chi^2 = 5$ for 6 degrees of freedom. We note that this slope is not as steep as in the coherent reaction $K^+D \to Q^+D$, where $B = 28 \pm 2$. In Fig. 75a, b

we show the decay angles for $K^*(890)$. θ and ϕ are the usual Gotfried-Jackson decay angles. The density matrix elements are calculated to be $\rho_{00} = .15 \pm .1$, $\rho_{1-1} = .1 \pm .1$, $\rho_{11} = .42 \pm .05$, which are consistent with being pure vector exchange.

ACKNOWLEDGMENTS

I wish to express my gratitude to Professor Gerson Goldhaber for his guidance, teaching, and advice during the years I have studied under him. Special thanks are due to Dr. Alexander Firestone for his close collaboration and guidance in the analysis of this experiment.

I would like to thank Professor George H. Trilling for his advice and interest and for many useful discussions.

Many other people have made essential contributions to this experiment: Robert Watt and the 82" bubble chamber crew at SLAC; the scanning and measuring staff of the Trilling-Goldhaber group; Howard S. White and the Data Handling Group; and the computing staff attached to the Trilling-Goldhaber group. All their help is gratefully acknowledged.

This work was supported by the U. S. Atomic Energy Commission.

APPENDIX: EXPERIMENTAL DETAILS AND CROSS SECTION CALCULATIONS

A. Experimental Details

The experiment was performed at the SLAC 82" bubble chamber. The deuterium-filled chamber was exposed to an r-f separated K^+ meson beam with 12-GeV/c incident momentum. The K^- transport beam was designed by J. Murray and S. Flatté[1]. Detailed information on the beam can be found elsewhere in the literature. A momentum resolution of $\Delta p/p = .2\%$ was achieved by using known correlations between beam momentum and transverse position in the bubble chamber. Pion contamination was reduced essentially to zero through the use of a gas Cerenkov counter. There was a 4.5% hydrogen contamination in the chamber.

A total of 500,000 bubble chamber pictures were taken with the 12-GeV/c K^+ beam with an average of 7.5 K^+ mesons incident/pulse. This corresponds to an average of 1.7 interactions per frame. Thus a total of 850,000 interactions were recorded on film. To reduce the measurement load, we restricted the measurement to the following topologies, marked by *.

Table I.

Event type	% in film	No events measured	No events remeasured
10. One-prong	9.3	N.M.[a]	N.R.M.[b]
17. One-prong + vee	1.1	7874	1145
20. Two-prong	22.6	N.M.[a]	N.R.M.[b]
27. Two-prong + vee	3.8	30,143	5316
30. Three-prong	8.2	67,578	8033
37. Three-prong + vee	1.4	13,698	2192
40. Four-prong Stop	8.2	50,819	6123
40. Four-prong No stop	14.8	N.M.[a]	N.R.M.[b]
Four-prong + vee	4.2	31,685	6182
50. Five-prong	4.7	-	N.R.M.[b]
57. Five-prong + vee	.53	-	N.R.M.[b]
60. Six-prong	10.9	N.M.[a]	N.M.[a]
67. Six-prong + vee	1.5	N.M.[a]	N.M.[a]
All rest.	8.8	N.M.[a]	N.M.[a]

* [a] N.M. = Not measured.

[b] N.R.M. = Not remeasured.

The events were scanned and roughly digitized on a road-making table at a rate of about 14-15 events per hour. The events were then measured on the FSD (Flying Spot Digitizer), which is a rapid automatic film plane digitizer. It has a measuring rate of about 100-120 events per hour. Remeasurements were carried out on the conventional digitizing machine, Frankenstein. We measured 50% of the film in order to study possible biases. Details on the number of events measured and remeasured are given in Table I.

The events were then subjected to the kinematical fitting program SIOUX. To be accepted at this stage, events had to have a confidence level greater than .1%. Stopping tracks were required to be either a proton or a deuteron. The treatment of invisible spectators and the reliability of the deuteron fits are discussed in Chapter II.

Remeasurements were carried out on 50% of the film. All events which failed kinematic reconstruction and events which failed 4c fits but had missing momenta for visible tracks of less than 1 Gev/c were candiates for remeasurement. The number of remeasured events contributed to each channel is less than 10%, and the distributions do not seem to indicate any gross systematic bias.

B. Cross Section Calculations

The cross section for a particular channel can be expressed as

expressed as $\sigma(K^+D \rightarrow x) = \frac{N_x}{N_{(total)}} \sigma \text{ total},$

where σ_{total} = total K^+D cross section at 12 GeV/c,

N_x = number of events in the channel,

N_{total} = total number of interactions in film.

σ total has been determined from measurement by Galbraith et al[9]

to be 33.9 ± .3.

In order to determine N_x, the number of events in a given channel, we have to determine scanning efficiencies, measurement efficiencies, and K^0 escape probability whenever we have a K^0 in the final state.

Scanning efficiencies were determined by a special rescan on a sample of rolls comparing the number of events found in scan and rescan. The results are shown in Table I. The measurement of efficiencies were determined by comparing events failing geometric reconstruction with those passing. The results of measurement efficiencies are given in Table I.

Table I

ET	Scan eff.	Meas. eff.	Eff. for event to pass system
17	87.5%	81.5%	71.5%
27	84.5%	77.5%	65.5%
30	91 %	83.5%	76 %
37	89.5%	76. %	68 %
40	87.5%	87.5%	76.5%
47	89 %	73 %	65 %

The total number of events in the film was determined by counting the number of interactions on a subsample of the film and comparing it to the total number of events scanned in the subsample and then renormalizing the total number of interactions.

The total number of interactions in the subsample was 7845 events. The total number of scanned events in the subsample was 2067 events. The total number of recorded events was 222,850, which corresponds

to a total of 746, 700 interactions in the film.

Escape probability for each K^0 event has been weighted according to the probability that a K^0 of the observed momentum and production angle decays within the chosen fiducial volume. K^0 events have also been corrected for K_1 and K_2 decays.

All cross sections have been corrected for hydrogen contamination in the chamber. No corrections to the cross sections were made due to Glauber screening. But the effect is expected to be small.

REFERENCES

1. S. Flatté, LBL Berkeley, Group A Memo No. 664.
2. J. M. Blatt and V. F. Weisskopf, Theoretical Nuclear Physics (John Wiley and Sons, New York, 1952), Cahp. II.
3. Lamek Hulthen and Seso Sugawara, in Handbuch der Physik (Springer-Verlag, Berlin, 1957), Vol. 39, Chap. I.
4. R. L. Glukstern and A. H. Bethe, Phys. Rev. 81, 761 (1951).
5. M. Moravcsik, Nucl. Phys. 7, 113 (1958).
6. S. A. de Witt, Ph.D. Thesis, University of Amsterdam, 1968.
7. V. J. Stenger et al., Phys. Rev. 134B, 1111 (1964).
8. I. Butterworth et al., Phys. Rev. Lett. 15, 734 (1965).
9. W. Galbraith et al., Phys. Rev. 138B, 913 (1965).
10. R. J. Glauber, Phys. Rev. 100, 242 (1955).
11. C. Wilkins, Phys. Rev. Lett. 17, 561 (1966).
12. A. Firestone et al., Phys. Rev. Lett. 25, 958 (1970).
13. Goldschmidt-Clermont et al., Phys. Rev. Lett. 27B, 602 (1968).
14. W. Rarita and B. M. Schwarzchild, Phys. Rev. 162, 1378 (1968).
15. P. J. Hartley et al., Phys. Rev. D1, 954 (1970).
16. D. Cline et al., Phys. Rev. Lett. 23, 1318 (1964).
17. P. Astbury et al., Phys. Lett. 23, 396 (1966).
18. Kwan Lai and James Louie, Nucl. Phys. 1319, 205 (1970).
19. Particle Data Group, Rev. Mod. Phys. 42, 87 (1970).
20. J. O. Ader et al., Nuvo Cimento LVIA, 952 (1968).
21. G. Abrams and U. Maor, Phys. Rev. Lett. 25, 621 (1970).
22. W. O. Dodd et al., Phys. Rev. 171, 1991 (1969).
23. D. J. Crennell et al., Phys. Rev. Lett. 22, 487 (1969).
24. W. de Bare et al., Nuovo Cimento LIA, N2 401, (1967).

25. Antich et al., Phys. Rev. Lett. 21, 842 (1968).

26. C. Fu et al., Nucl. Phys., B18, 93,(1920).

27. J. V. Beupre et al., CERN/D. Ph. II /Phys. 70-42. (Rev. Vers.)(1970).

28. Bishop et al., Nucl. Phys., B9, 402 (1969).

29. Bassompiere et al., Nucl. Phys., B13, 198 (1969).

30. M. Aguilar-Benitz et al., Phys. Rev. Lett., 25, 1362 (1970).

31. E. Famimia et al., BNL Report No. 14572 (1970).

32. For a recent review of the L meson, see C-Y, Chien in Experimental Meson Spectroscopy, edited by C. Baltay and A. H. Rosenfeld, (Columbia University Press, New York, 1970), p. 275.

33. K. Boesebeck et al., CERN/D. Ph. II/Phys. 70-49,((Rev.-Ver.) (1971).

34. For a recent review of the Q meson, see A. Firestone in Experimental Meson Spectroscopy, edited by C. Baltay and H. Rosenfeld (Columbia University Press, New York, 1970), p. 27.

35. Alexander et al., Nucl. Phys. B13, 503 (1969).

36. K. W. J. Barnham, et al., Nucl. Phys. B25, 49 (1971).

37. K. Gottfried and J. D. Jackson, Nuovo Cimento 33 No. 2, (1964).

38. G. Goldhaber, Phys. Rev. Lett. 19, 976 (1967).

39. R. Mercer et al., Johns-Hopkins University, JHU-702.

40. R. Gatto and L. Maiani, Phys. Lett. 26B, 95 (1967).

41. G. F. Chew and A. Pignotti, Phys. Rev. Lett. 20, 1078 (1968).

42. H. W. Clopp et al., Bull. Am. Phys. Soc 16, 547 (1971).

43. S. M. Berman and M. Jacob, Phys. Rev. 139, B1023, (1965).

44. T. G. Tripp et al., Phys. Lett. 28B, 203 (1968).

45. K. Boesebeck et al., CERN/D. Ph II/Phys. 70-49.

FIGURE CAPTIONS

Fig. 1. (a) Radial Separation of the nucleons in the deuteron. (b) Momentum distribution of nucleons in the deuteron. Predicted by Hulthén wave function.

Fig. 2. Spectator momentum distributions for the reactions (a) $K^+d \to K^0pp$, (b) $K^+d \to K^+\pi^-pp$, (c) $K^+d \to K^0\pi^+\pi^-pp$. The curve is a theoretical prediction normalized to number of events.

Fig. 3. $\cos\theta$, the angle between the beam and the spectator, for the reactions (a) $K^+d \to K^0pp$, (b) $K^+d \to K^+\pi^-pp$, (c) $K^+d \to K^0\pi^+\pi^-pp$.

Fig. 4. (a) The deuteron form factor [H(t) vs. t]. (b) The correction factor for the spin-nonflip amplitude [1/1 -H(t) vs. t].

Fig. 5. M(p, n) for events with a visible proton in the reactions (a) $K^+d \to K^0\pi^+pn$ and (b) $K^+d \to K^+\pi^+\pi^-pn$. The shaded region corresponds to events satisfying the corresponding coherent reaction.

Fig. 6. $\cos\theta$, the angle between two outgoing nucleons, for events with a visible proton in the reactions (a) $K^+d \to K^0\pi^+pn$ and (b) $K^+d \to K^+\pi^+\pi^-pn$. The shaded region corresponds to events satisfying the corresponding coherent hypothesis.

Fig. 7. M(p, n) for the reaction (a) $K^+d \to K^+\pi^+\pi^-$ (p)n and (b) $K^+d \to K^+\pi^+\pi^-p_sn$. (Proton momentum less than neutron momentum.) The shaded region corresponds to coherent events.

Fig. 8. Cross section vs. incident momentum for the reaction $K^+d \to K^0pp$.

Fig. 9. $d\sigma/dt$ vs. t for the reaction $K^+d \to K^0pp$.

Fig. 10. $d\sigma/dt$ vs. t for the reaction $K^+n \to K^0p$. The smooth curves are predictions of models by Hartley et al. and Rarita and

Schwarzchild, and a result of a fit by a function of the form $\frac{d\sigma}{dt} = Ae^{bt}$.

Fig. 11. $d\sigma/dt$ vs. t for the charge exchange reactions $K^+n \to K^0 p$ and $K^-p \to \bar{K}^0 n$

Fig. 12. Cross section vs. incident momentum for the reactions $K^+d \to K^0 pp$ and $K^+p \to K^0 \Delta^{++}$.

Fig. 13. Dalitz plot, $M^2(p, \pi^-)$ vs. $M^2(K^+, \pi^-)$ for the reaction $K^+n \to K^+\pi^-p$.

Fig. 14. Chew-Low plot, $t_{K-K\pi}$ vs. $M^2(K^+, \pi^-)$ for the reaction $K^+n \to K^+\pi^-p$ (a) all events, (b) N^* events removed.

Fig. 15. Chew-Lot plot, $t_{p-p\pi-}$ vs. $M^2(p, \pi^-)$ for the reaction $K^+n \to K^+\pi^-p$.

Fig. 16. $M(p, \pi^-)$ for the reaction $K^+n \to K^+n \to K^+\pi^-p$.

Fig. 17. $M(K^+, \pi^-)$ for the reaction $K^+n \to K^+\pi^-p$: (a) all events, (b) events with $t' < .2(GeV/c)^2$.

Fig. 18. $M(K^+, \pi^-)$ vs. $\cos\theta$ for events with $t' < .2(GeV/c^2)$ in the reaction $K^+n \to K^+\pi^-p$.

Fig. 19. $M(K^+, \pi^-)$ vs. $\langle Y_\ell^0 \rangle$ for events with $t' < .2(GeV/c)^2$ in the reaction $K^+n \to K^+\pi^-p$.

Fig. 20. $M(K^+, \pi^-)$ vs. $N\langle Y_\ell^0 \rangle$ for events with $t' < 2(GeV/c)^2$ in the reaction $K^+n \to K^+\pi^-p$.

Fig. 21. $M(K^0, \pi^+, \pi^-)$ for the reaction $K^+n \to K^0\pi^+\pi^-p$.

Fig. 22. $M(p, \pi^+, \pi^-)$ for the reaction $K^+n \to K^0\pi^+\pi^-p$. The shaded region corresponds to events in the Δ^{++} region.

Fig. 23. The scatter plot $M(K^0, \pi^+)$ vs. $M(p, \pi^-)$ for the reaction $K^+n \to K^0\pi^+\pi^-p$.

Fig. 24. (a) $M(K^0, \pi^+)$, (b) $M(P,\pi^-)$ for the reaction $K^+n \to K^0\pi^+\pi^-p$.

Fig. 25. Scatter plot $M(K^0_S\pi^-)$ vs. $M(p, \pi^+)$ for the reaction $K^+n \to K^0\pi^+\pi^-p$.

Fig. 26. (a) $M(K^0, \pi^-)$, (b) $M(p, \pi^+)$ for the reaction $K^+n \to K^0\pi^+\pi^-p$.

Fig. 27. Scatter plot $M(K^0, \pi^+)$ vs. $M(\pi^+, \pi^-)$ for the reaction $K^+n \to K^0\pi^+\pi^-p$.

Fig. 28. $M(\pi^+, \pi^-)$ for the reaction $K^+n \to K^0\pi^+\pi^-p$.

Fig. 29. $d\sigma/dt$ vs. t for the reaction $K^+d \to K^*_{890}pp$.

Fig. 30. $K^*(890)$ decay angular distribution: (a) $\cos\theta$, (b) ϕ.

Fig. 31. $K^*(890)$ density matrix elements vs. t: (a) ρ_{00} vs. t, (b) σ_1^+ vs. t, (c) σ_1^- vs. t.

Fig. 32. $\rho_{00}\frac{d\sigma}{dt}$ vs. t for the reaction $K^+n \to K^*_{890}p$.

Fig. 33. $M(K^+, \pi^-)$ for events with $t < .1\ (GeV/c)^2$ for the reaction $K^+n \to K^+\pi^-p$.

Fig. 34. Decay angular distributions for $M(K^+, \pi^-)$ at I, 1.3 - 1.4 GeV: (a) $\cos\theta$, (c) ϕ and at II, 1.4 - 1.5 GeV, (b) $\cos\theta$, (d) ϕ.

Fig. 35. $d\sigma/dt$ vs. t for $M(K^+,\pi^-)$ in (a) 1.3 - 1.4 GeV, (b) 1.4 - 1.5 GeV.

Fig. 36. $M(K^+, \pi^-)$ for events with $t' < .2\ (GeV/c)^2$ and (a) $.7 < |\cos| < 1$, (b) $|\cos| < .7$.

Fig. 37 S-wave events as a function of $K^+\pi^-$ mass for the reaction $K^+n \to K^+\pi^-p$.

Fig. 38 (a) $K^*(1420)$ decay Dalitz plot, (b) $M(K^0, \pi^+)$, (c) $M(\pi^+, \pi^-)$.

Fig. 39. Decay angles for $M(K^+, \pi^-)$ mass regions: (a) 1.5 - 1.6 GeV, (b) 1.6 - 1.75 GeV, (c) 1.75 - 2 GeV, (d) 2-2.25 GeV.

Fig. 40. $M(K^+, \pi^-)$ for events with $t' < .2\ (GeV/c)^2$ and $\cos\theta$: (a) $\cos\theta > .776$, (b) $0 < \cos\theta < .775$, (c) $-.775 < \cos\theta < 0$, (d) $-1 < \cos\theta < -.775$.

Fig. 41. Chew-Low boundary for the reaction $K^+n \rightarrow K^+\pi^-p$ and $K^+p \rightarrow K^+\pi^- \Delta^{++}(1240)$ at 12 GeV/c.

Fig. 42. $M(K^+, \pi^-)$: (a) t accessible to Δ^{++} reaction, (b) t inaccessible to Δ^{++} reaction.

Fig. 43. $M(p, \pi^-)$ for the reaction $K^+n \rightarrow K^+\pi^-p$:
(a) $t_{p-p\pi} < .1$ $(GeV/c)^2$
(b) $.1 < t_{p-p\pi} < .4$, (c) $t_{p-p\pi} > .4$ $(GeV/c)^2$.

Fig. 44. $\langle Y_\ell^0 \rangle$ moments vs. $M(p,\pi^-)$ for the reaction $K^+n \rightarrow K^+\pi^-p$.

Fig. 45. $M(D, \pi^+)$, $M(K^+ . \pi^-)$ for unambiguous events in the reaction $KD \rightarrow K\pi\pi D$

Fig. 46. For ambiguous events with χ^2 difference greater than 3:
(a) $D\pi^+$ for selected events, (b) $M_1(K, \pi^-)$ vs. $M_2(K^+, \pi^-)$,
(c) $M_1(K^+, \pi^-)$, (d) $M_2(K^+, \pi^-)$.

Fig. 47. For a subsample of ambiguous events with χ^2 difference less than 3: (a) $D\pi^+$ for selected events, (b) $M_1(K^+, \pi^-)$, vs. $M_2(K^+, \theta^-)$, (c) $M_1(K^+, \pi^-)$, (d) $M_2(K^+, \pi^-)$.

Fig. 48. Chew-Lot plot, t_{D-D} vs. $M^2(K^+, \pi^+, \pi^-)$ for the reaction $KD \rightarrow K\pi\pi D$.

Fig. 49. $d\sigma/dt$ vs. t for the reaction $KD \rightarrow K\pi\pi D$.

Fig. 50. $M(K, \pi, \pi)$ shaded events with D^* out.

Fig. 51. $M(K, \pi, \pi)$ shaded events with four-prong topology.

Fig. 52. Two-body invariant masses for the reaction $KD \rightarrow K\pi\pi D$:
(a) $M(K^+, \pi^-)$, (b) $M(D, \pi^+)$, (c) $M(K^+, \pi^+)$, (d) $M(D, \pi^-)$, (e) $M(D, K^+)$, (f) $M(\pi^+, \pi^-)$.

Fig. 53. Scatter plot $M^2(K^+, \pi^+, \pi^-)$ vs. $M(D, \pi^+)$ for the reaction $KD \rightarrow K\pi\pi D$.

Fig. 54. $M(K^*(890), \pi)$, the shaded region has the D^* out.

Fig. 55. $M(K, \pi, \pi)$ weighted by $1/H(q)$.

Fig. 56. $d\sigma/dt$ vs. t for $M(K, \pi, \pi)$ mass regions: (a) 1.0 - 1/2 GeV, (b) 1.2 - 1.3 GeV, (c) 1.3 - 1.4 GeV, (d) 1.4 - 1.5 GeV.

Fig. 57. Decay Dalitz plot for $M(K, \pi, \pi)$ regions (a), (b), (c), (d).

Fig. 58. $M(K^+, \pi)$ for events in $M(K, \pi, \pi)$ regions (a), (b), (c), (d).

Fig. 59. $M(\pi^+, \pi^-)$ for events in $M(K, \pi, \pi)$ regions (a), (b), (c), (d).

Fig. 60. $K^*(890)$ decay angle Θ_{KK^*} for $K^*(890)$ events in $M(K, \pi, \pi)$ regions (a), (b), (c), (d).

Fig. 61. ϕ, $K^*(890)$ decay angle, for $K^*(890)$ events in $M(K, \pi, \pi)$ regions (a), (b), (c), (d).

Fig. 62. $K^*(890)$ decay angle $\Theta_{K,K}$ for $M(K^*(890), \pi)$ regions (a), (b), (c), (d).

Fig. 63. β normal to $K\pi\pi$ decay plane for $M(K^*890)\pi)$: (a), (b), (c), (d).

Fig. 64. ϕ, normal decay angle of 1 for $K^*(890)$ events in $M(K^*890, \pi)$ regions (a), (b), (c), (d).

Fig. 65. Cos (ξ), $K^*(890)$ helicity decay angle in the Q rest frame for $M(K^*890,\pi)$ regions (a), (b), (c), (d).

Fig. 66. (a) Cos θ; Jackson decay angle for D^{*++}, (b) Feynman diagram describing D^{*++} production.

Fig. 67. $K^*(890)$ decay angular distribution for $K^*(890)$ events recoiling against D^{*++}.

Fig. 68. $d\sigma/dt$ vs. t for D^{*++} events (a) $t_{D\text{-}D}$, (b) $t_{D\text{-}D^*}$.

Fig. 69. $M(K^+, \pi^-)$ recoiling against D^{*++}.

Fig. 70. $M(K, \pi, \pi)$ associated with D^{*++}.

Fig. 71. $M(K, \pi, \pi)$ for events with $M(D^+, \pi^-) < 3$ GeV.

Fig. 72. (a) L decay Dalitz plot. (b) $M(K^+, \pi^-)$, (c) $M(\pi^+, \pi^-)$ for L

events, L with $(D\pi^+) < 3$ GeV.

Fig. 73. Two-body invariant mass for the reaction $KD \to K^0\pi^+D$: (a) $M(D, \pi^+)$, (b) $M(D, K^0)$, (c) $M(K^0, \pi^+)$.

Fig. 74. $d\sigma/dt$ vs. t for the reaction $K^+D \to K^*_{890}D$.

Fig. 75. $\cos\theta, \phi$ for $K^*(890)$ decay in the reaction $KD \to K^*_{890}D$.

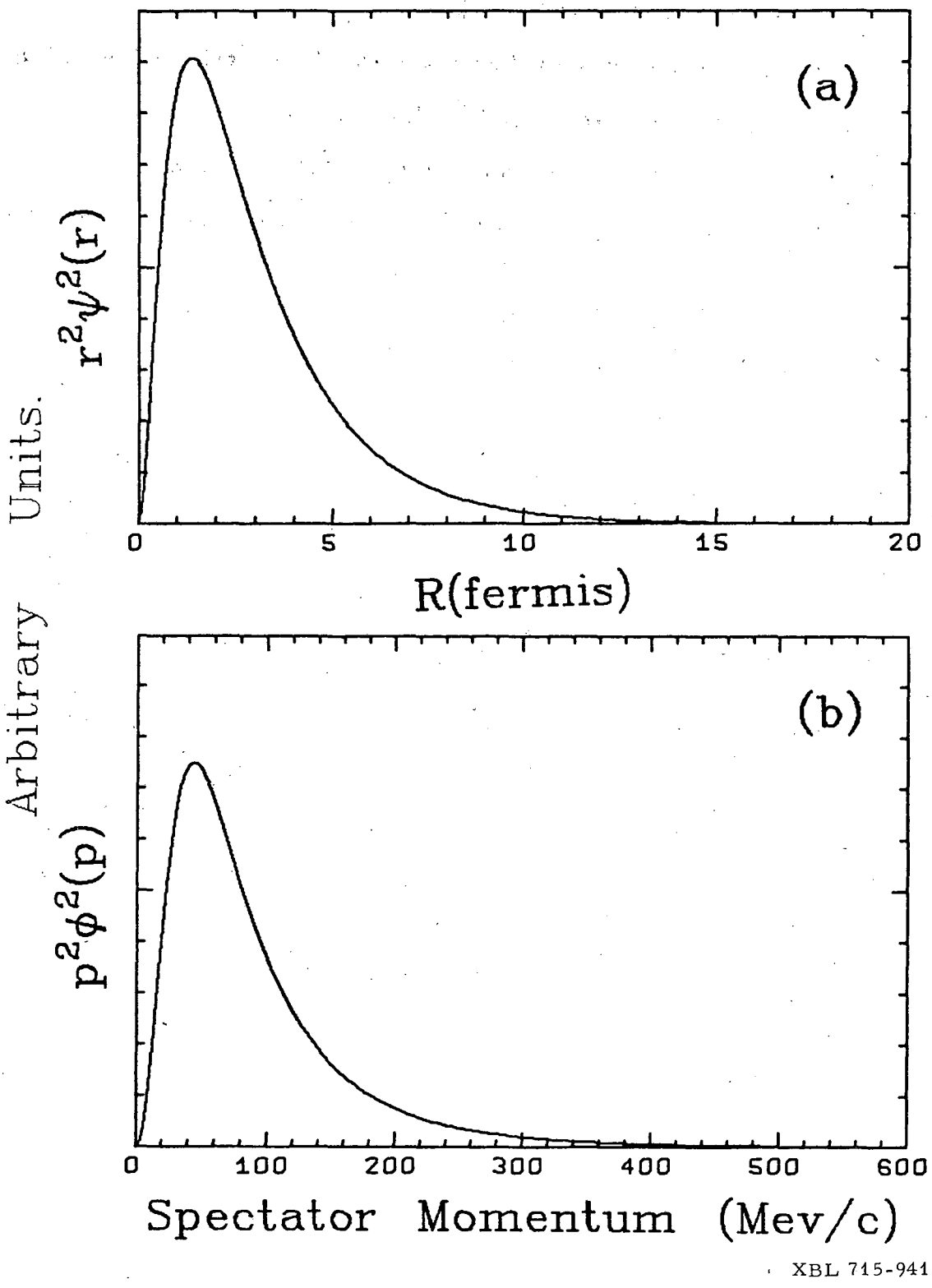
(a)
Units.
$r^2\psi^2(r)$
0
5
10
15
20
R(fermis)
(b)
Arbitrary
$p^2\phi^2(p)$
0
100
200
300
400
500
600
Spectator Momentum (Mev/c)
XBL 715-941

Fig. 1

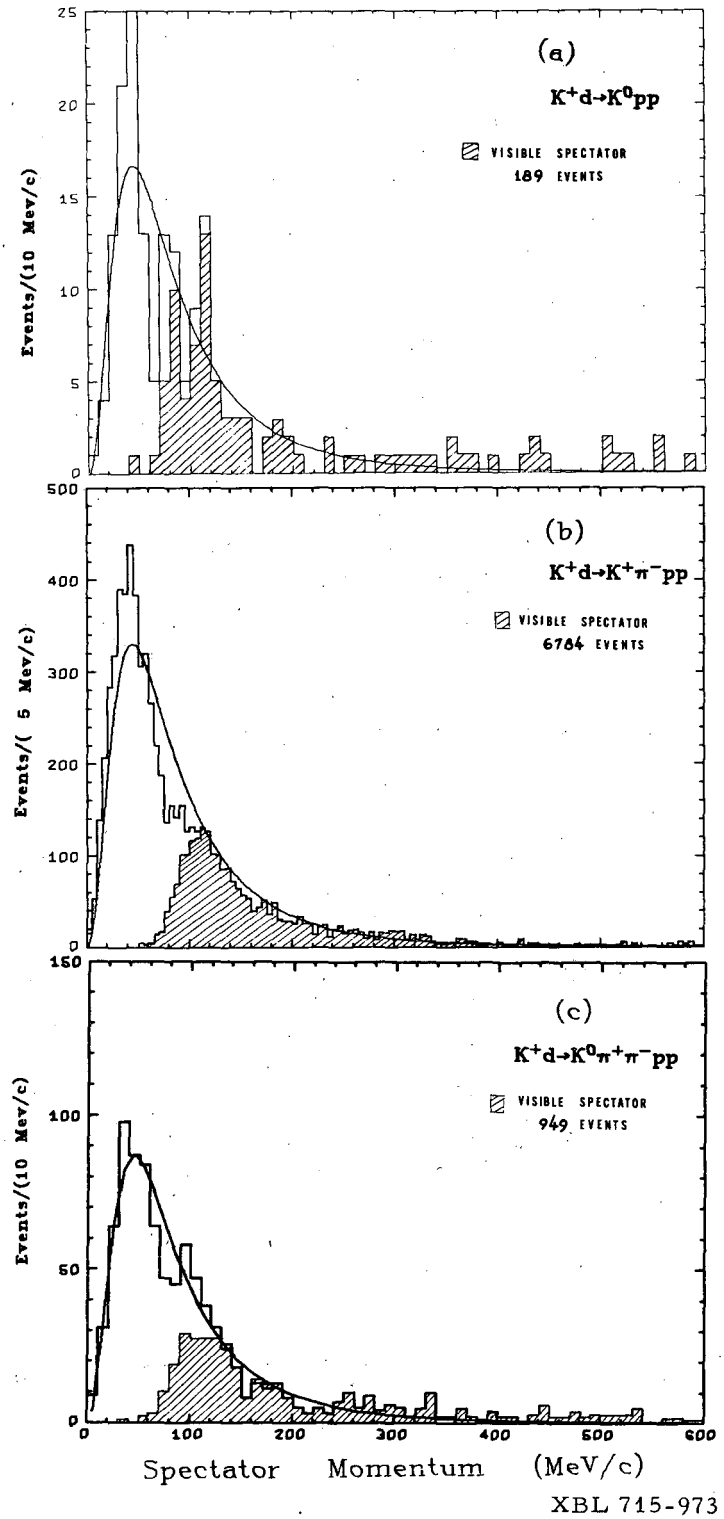
(a)
$K^+d \to K^0pp$
VISIBLE SPECTATOR
189 EVENTS
Events/(10 Mev/c)
(b)
$K^+d \to K^+\pi^-pp$
VISIBLE SPECTATOR
6764 EVENTS
Events/(5 Mev/c)
(c)
$K^+d \to K^0\pi^+\pi^-pp$
VISIBLE SPECTATOR
949 EVENTS
Events/(10 Mev/c)
Spectator Momentum (MeV/c)
XBL 715-973

Fig. 2

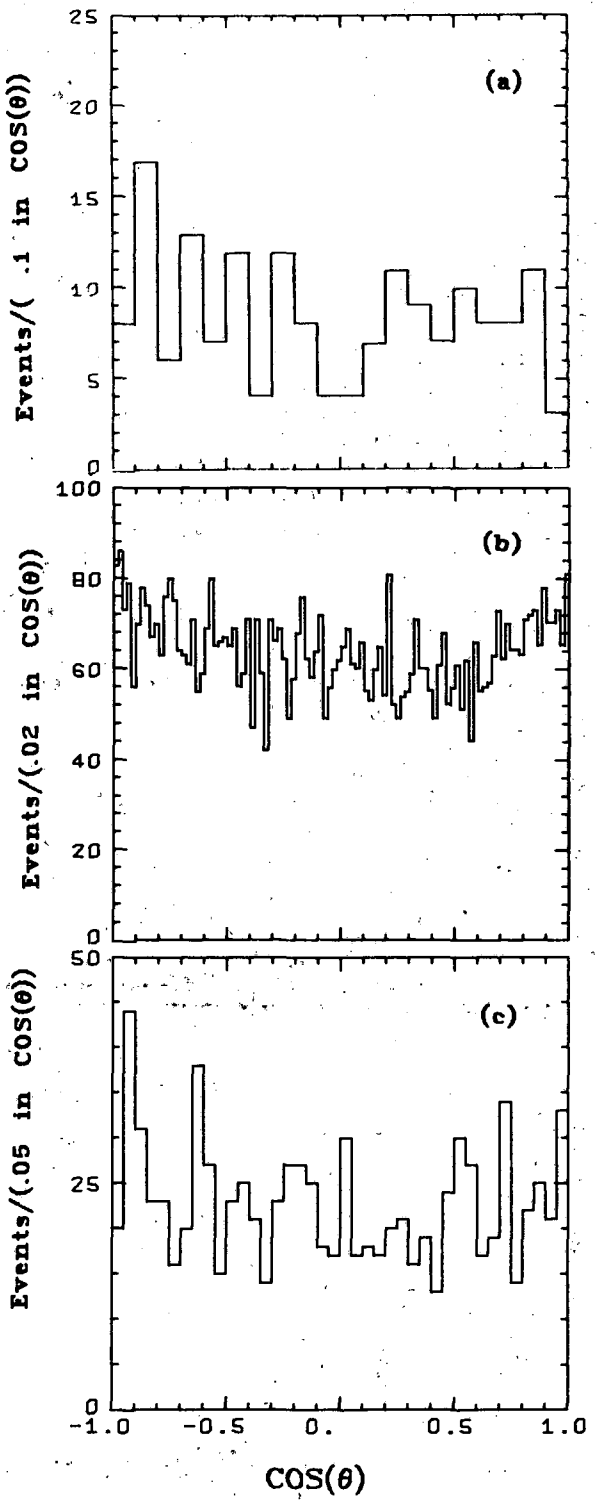
(a)
(b)
(c)
Events/(.1 in COS(θ))
Events/(.02 in COS(θ))
Events/(.05 in COS(θ))
COS(θ)
XBL 715-938

Fig. 3

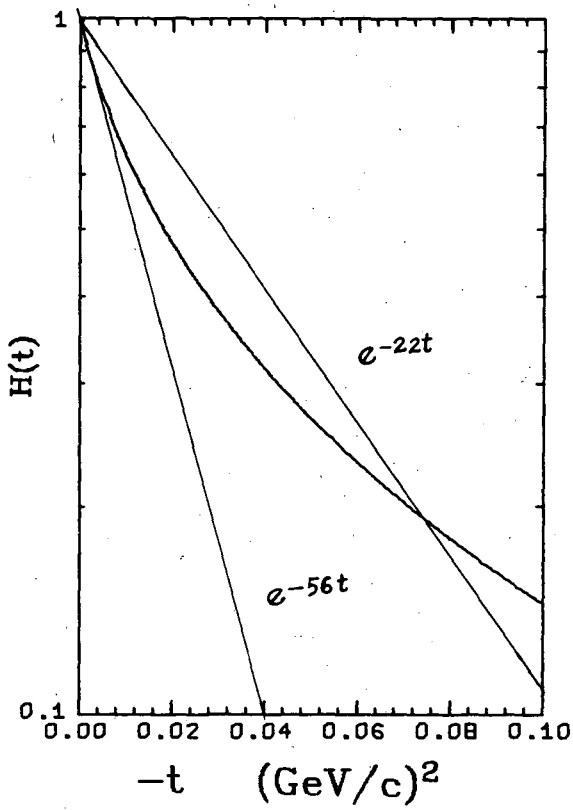

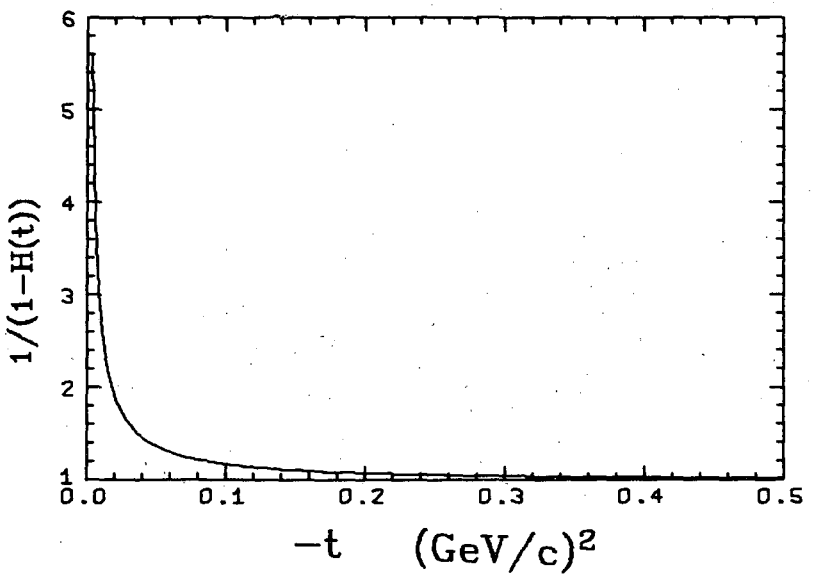

XBL 715-972

Fig. 4

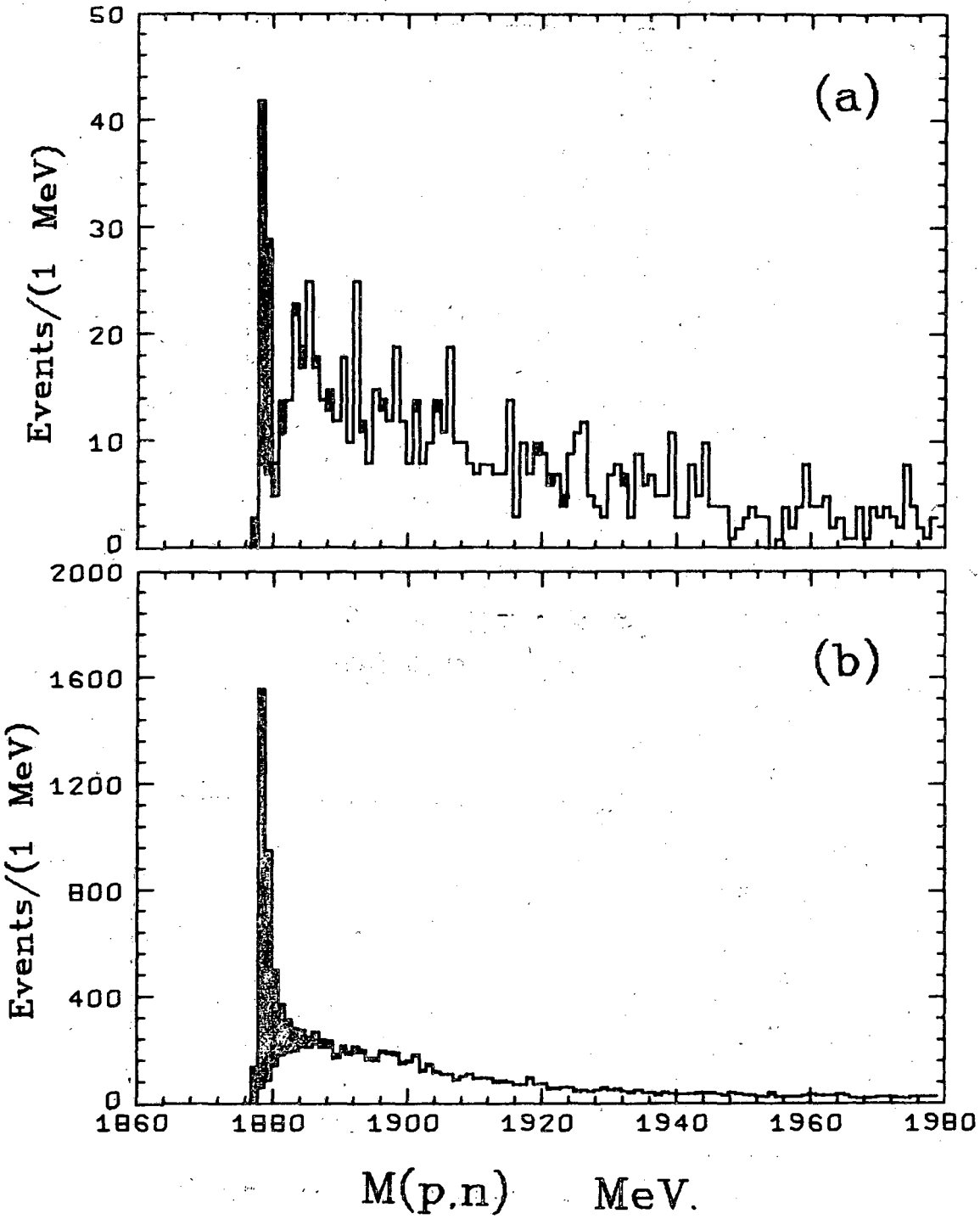

XBL 715-934

Fig. 5

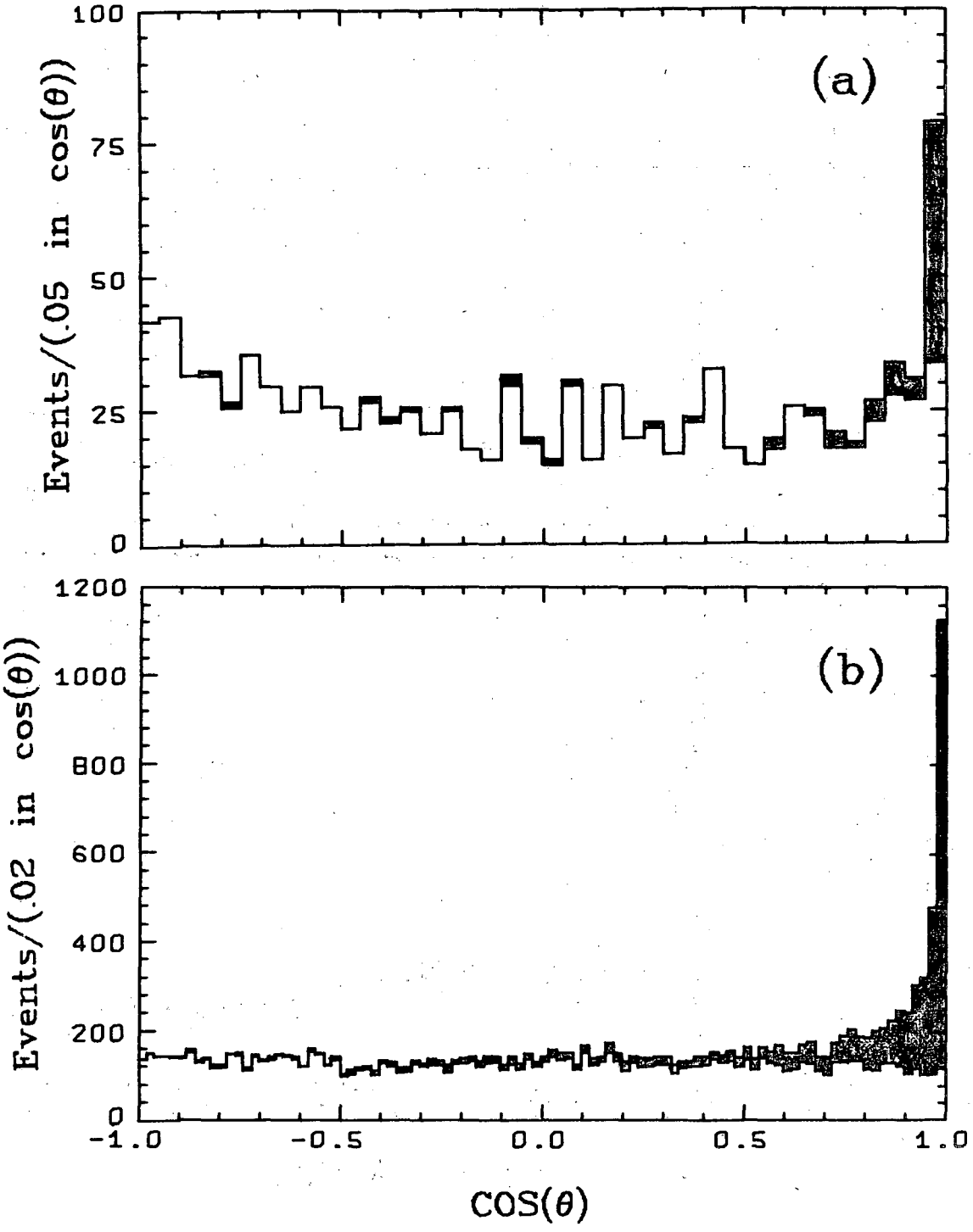
(a)
Events/(.05 in cos(θ))
100
75
50
25
0
(b)
Events/(.02 in cos(θ))
1200
1000
800
600
400
200
0
-1.0
-0.5
0.0
0.5
1.0
COS(θ)
XBL 715-936

Fig. 6

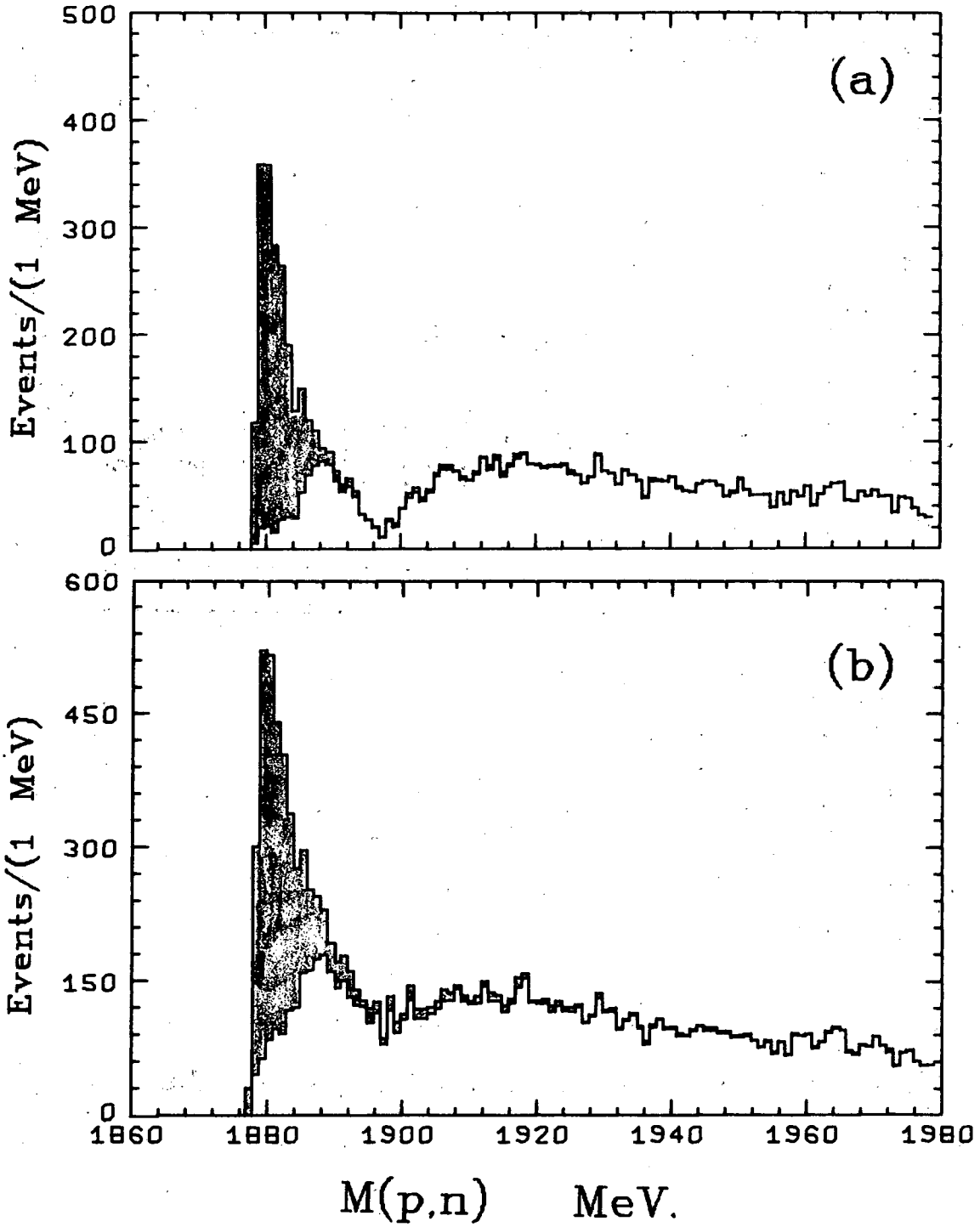

XBL 715-937

Fig. 7

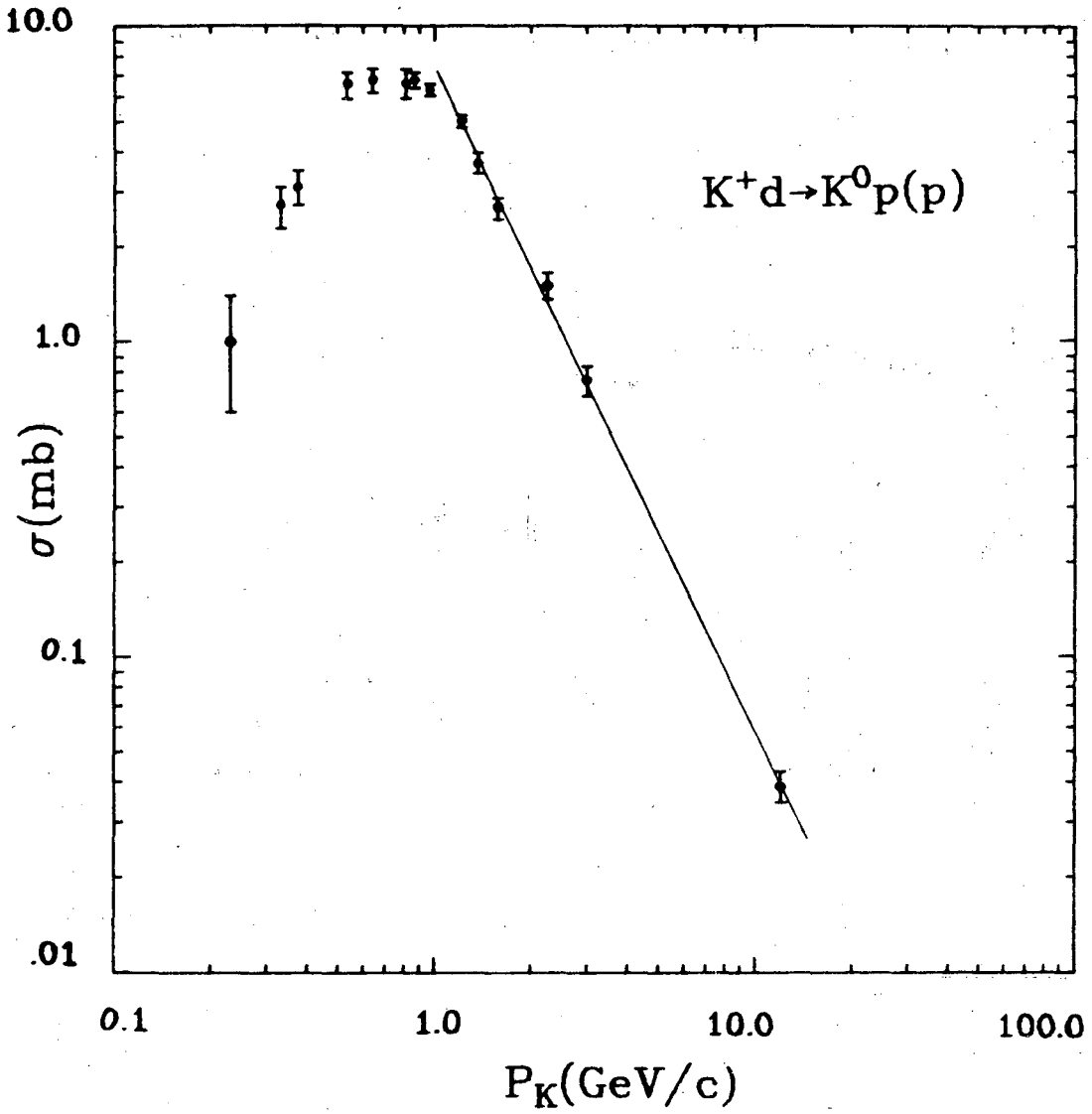

Fig. 8

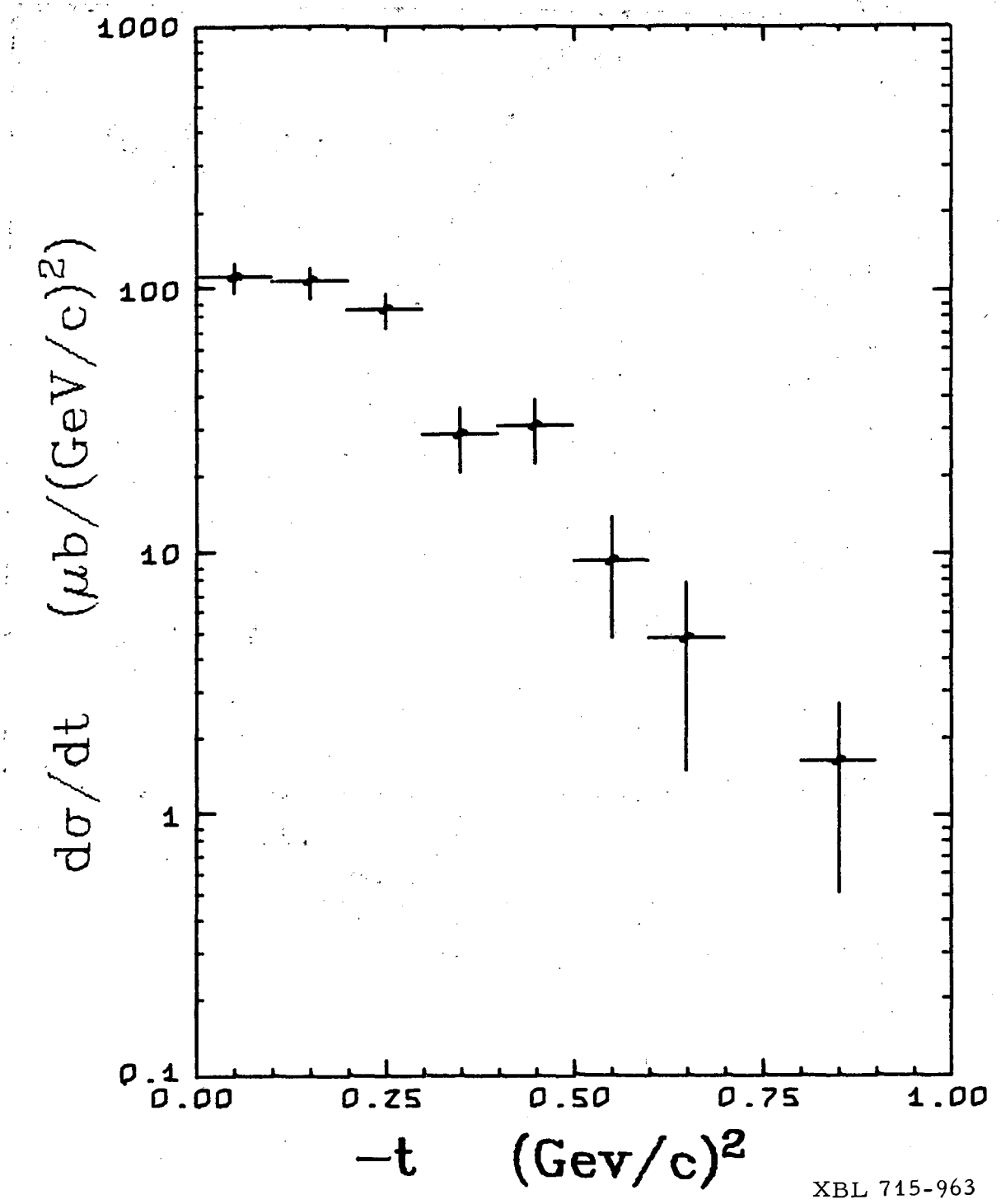
1000
100
10
1
0.1
0.00
0.25
0.50
0.75
1.00
dσ/dt (μb/(GeV/c)²)
−t (Gev/c)²
XBL 715-963

Fig. 9

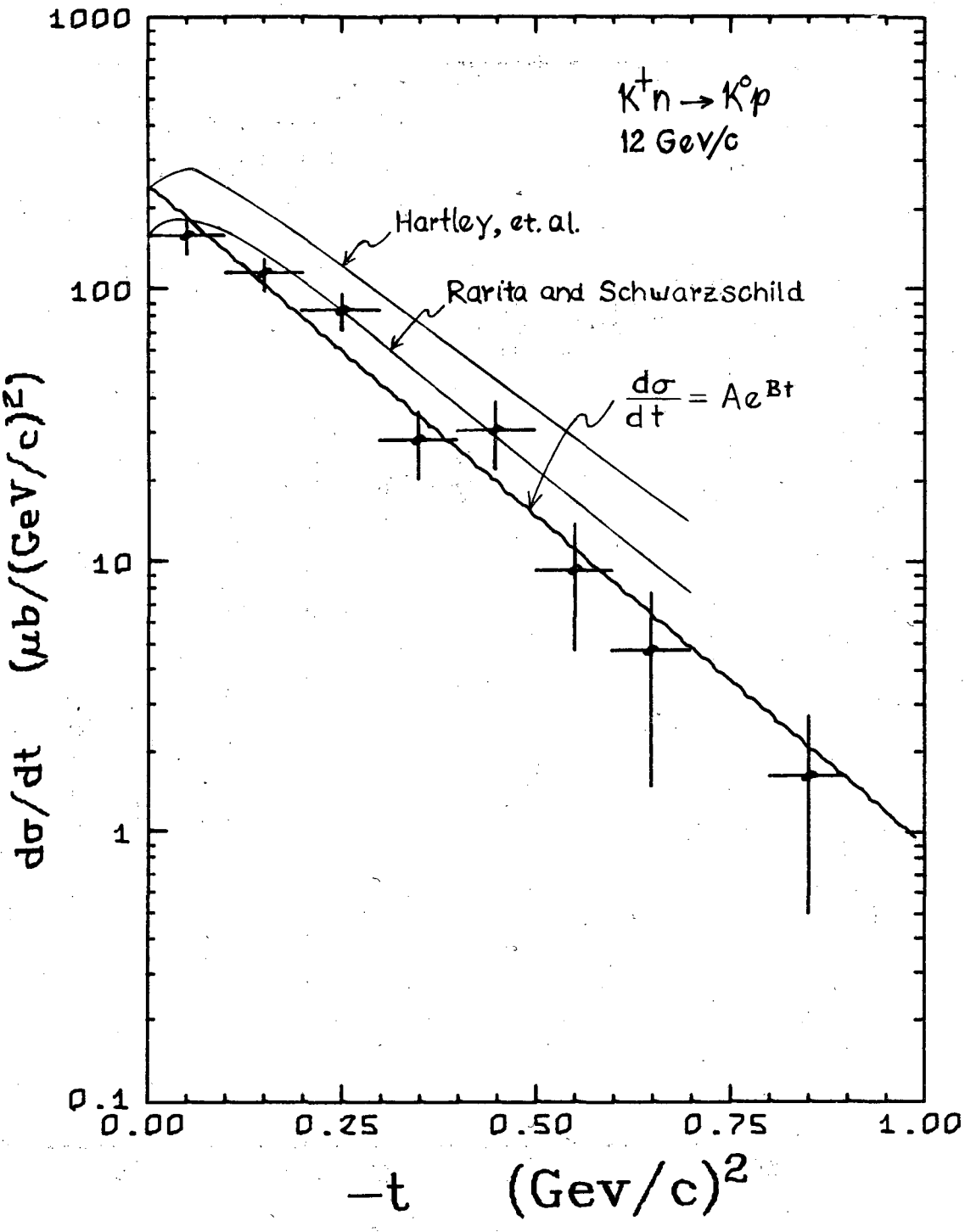

XBL 715-1014

Fig. 10

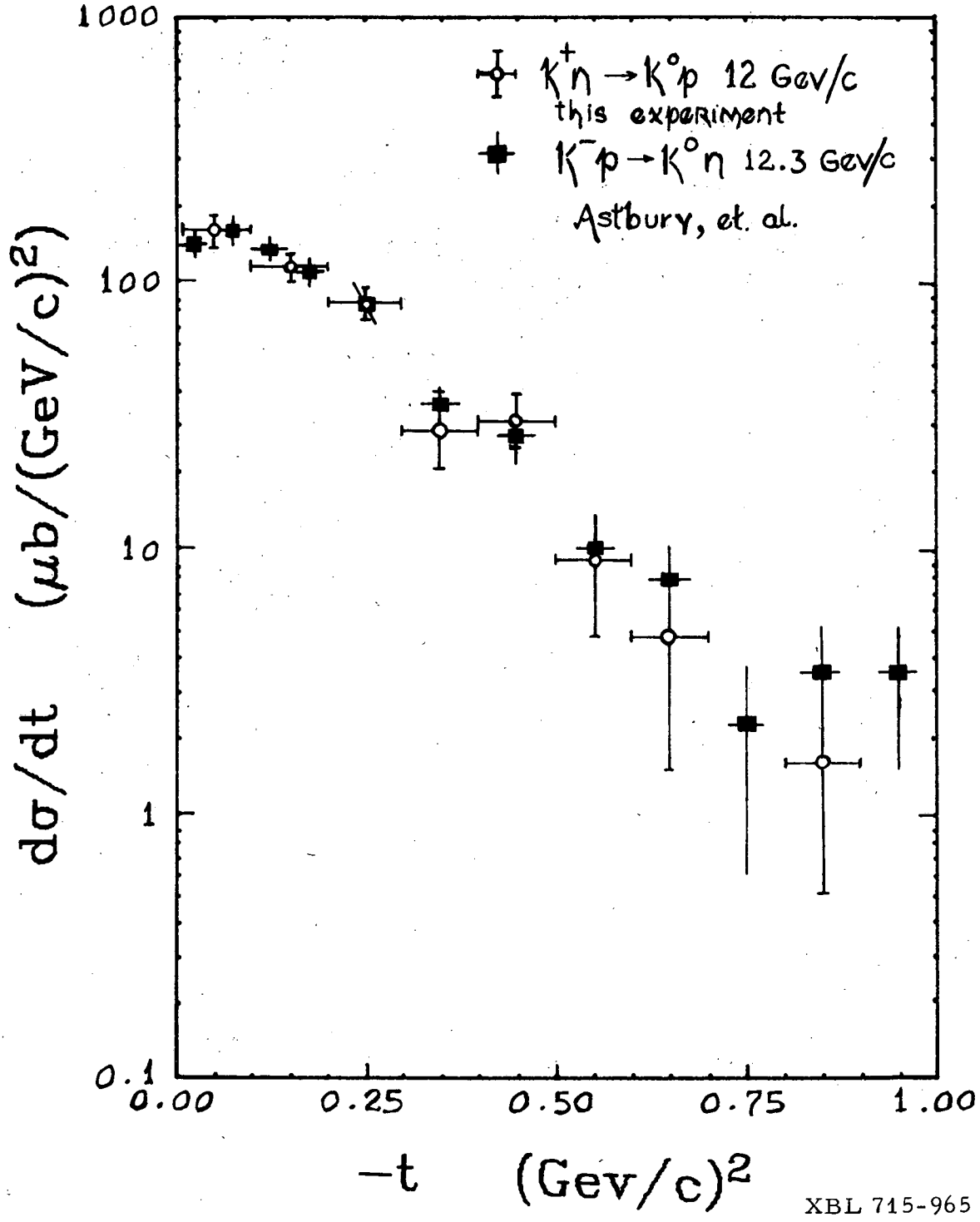
1000
100
10
1
0.1
0.00
0.25
0.50
0.75
1.00
dσ/dt (μb/(GeV/c)²)
−t (Gev/c)²
K⁺n → K°p 12 Gev/c
this experiment
K⁻p → K°n 12.3 Gev/c
Astbury, et. al.
XBL 715-965

Fig. 11

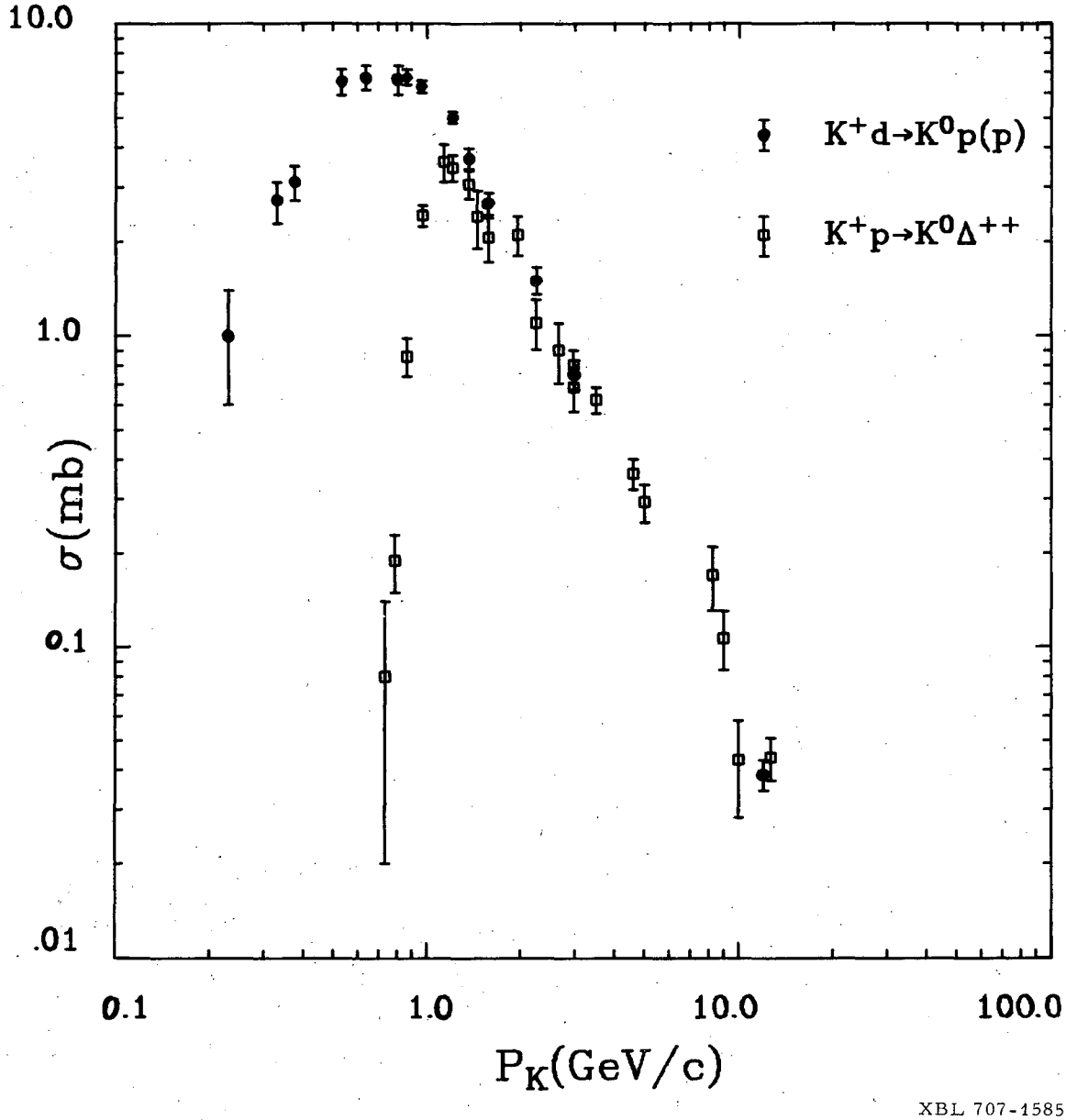

XBL 707-1585

Fig. 12

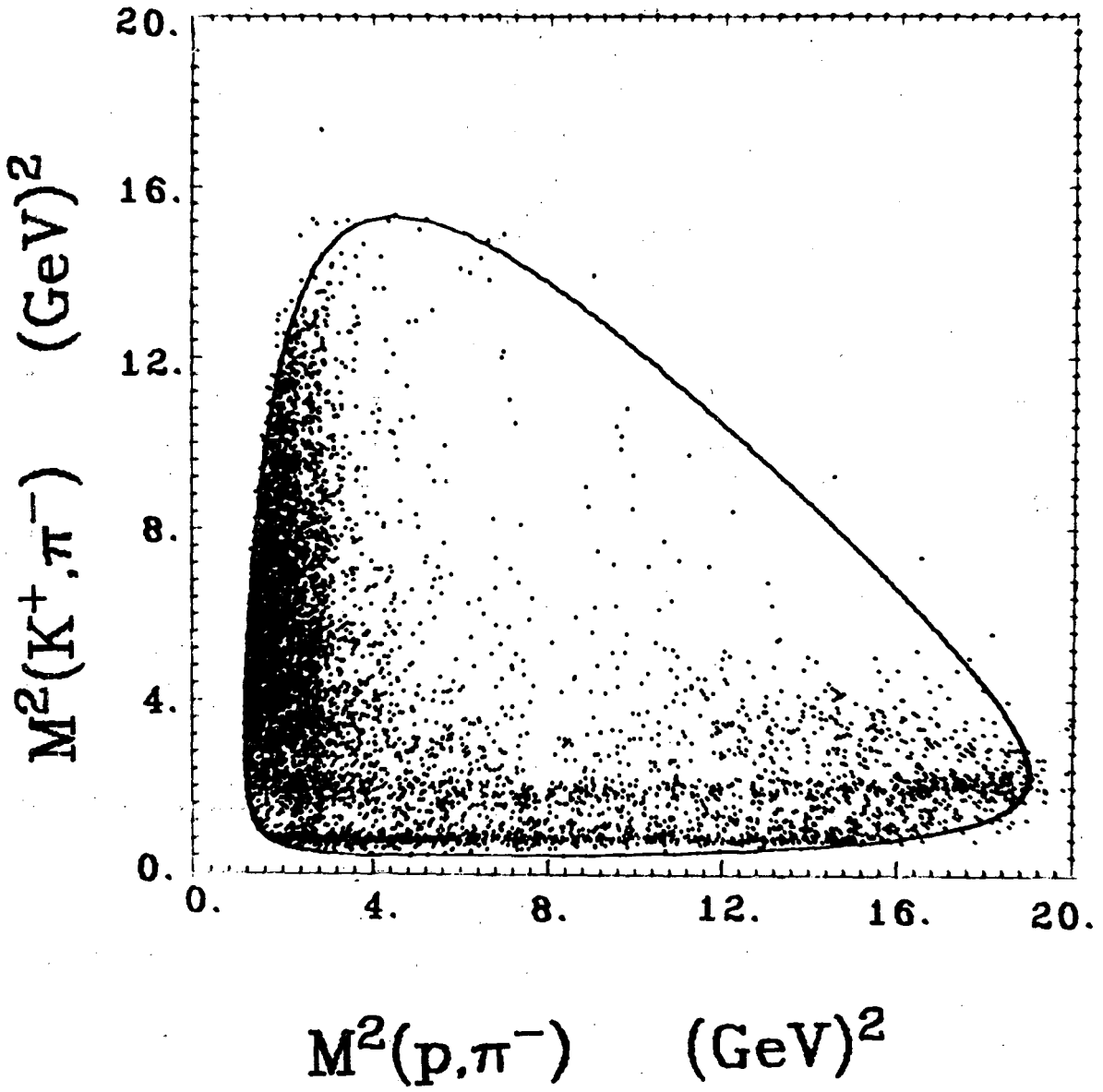

XBL 716-1119

Fig. 13

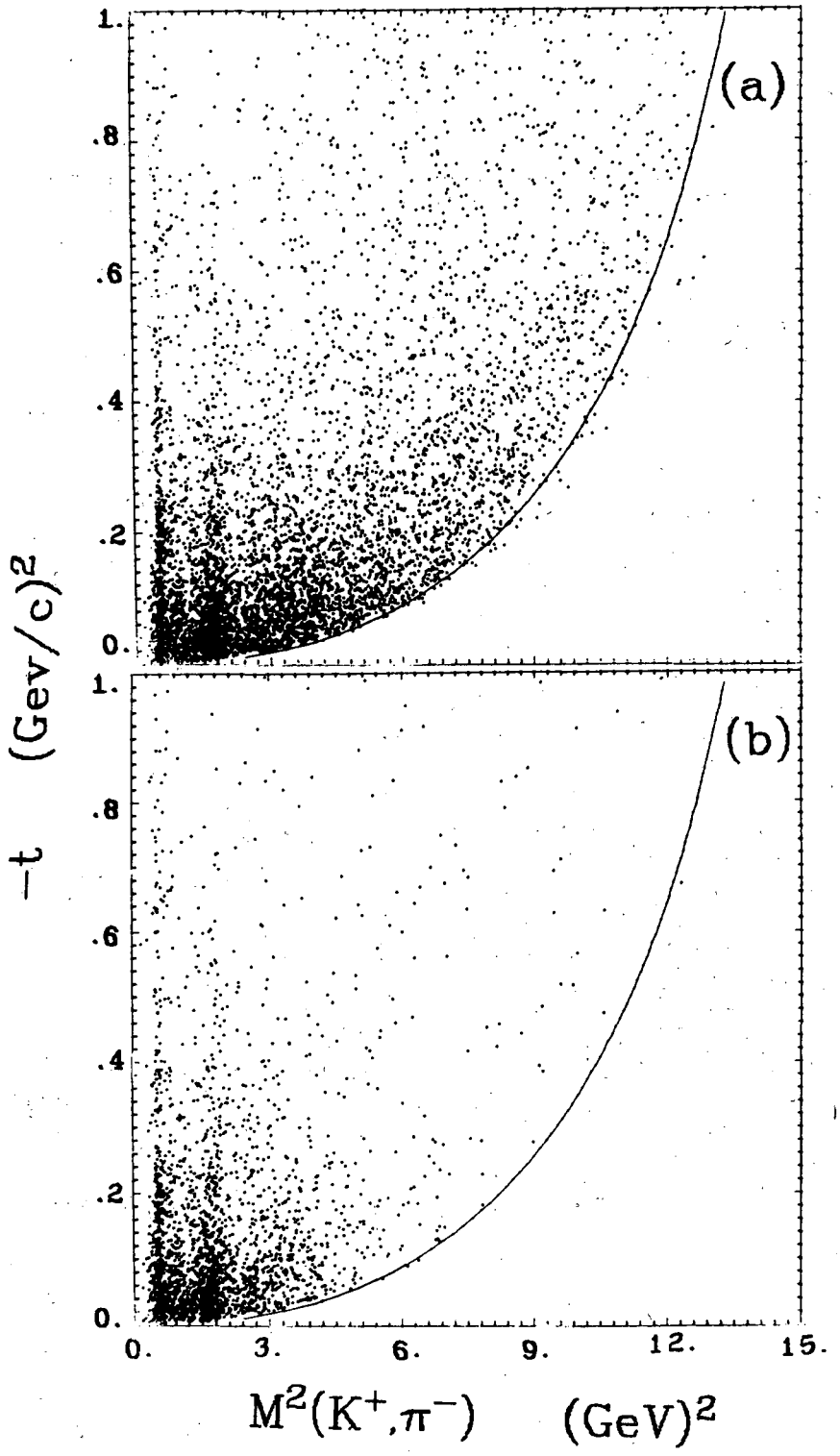

Fig. 14

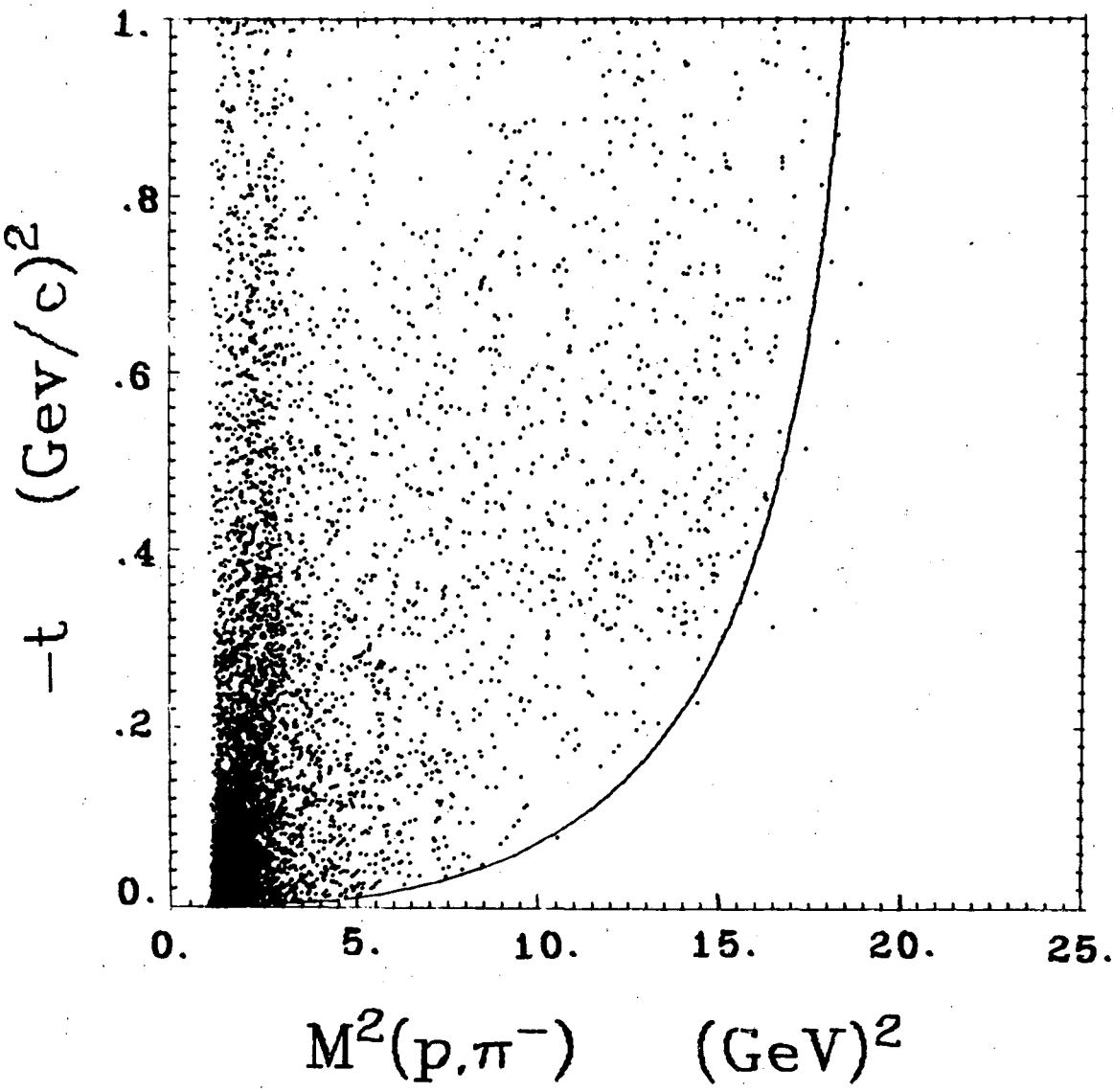

XBL 716-1118

Fig. 15

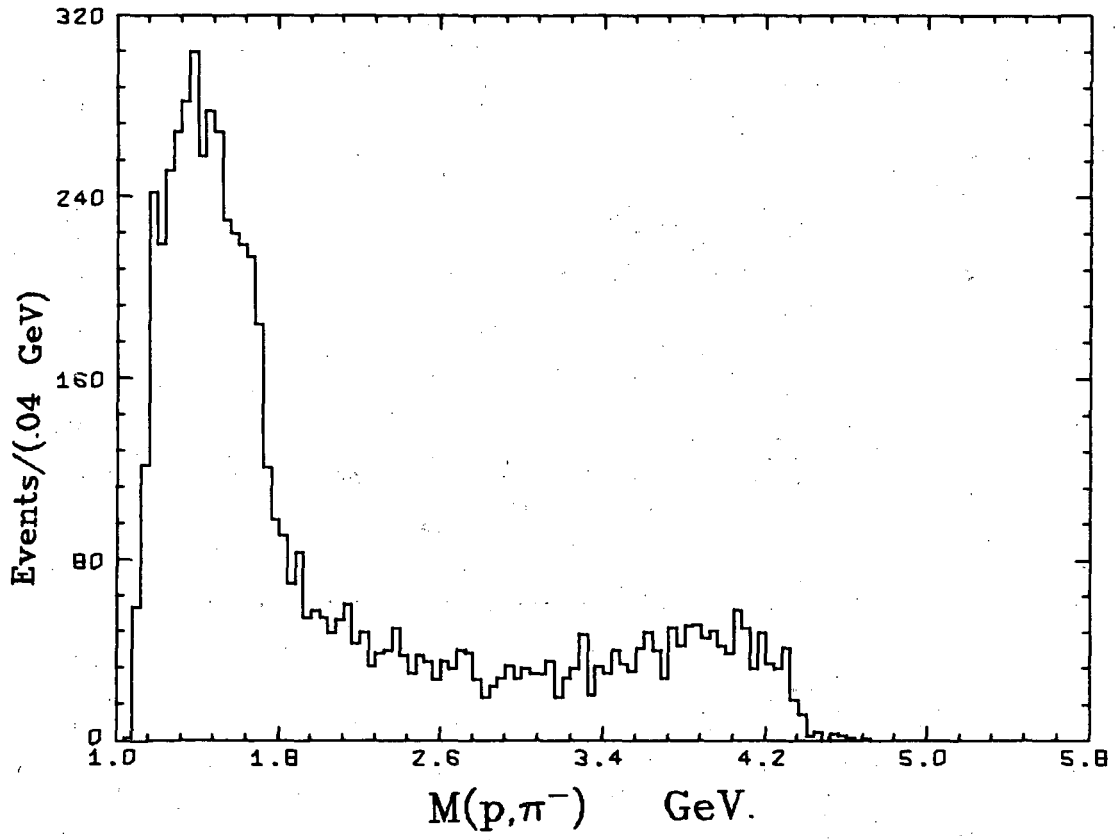

XBL 715-958

Fig. 16

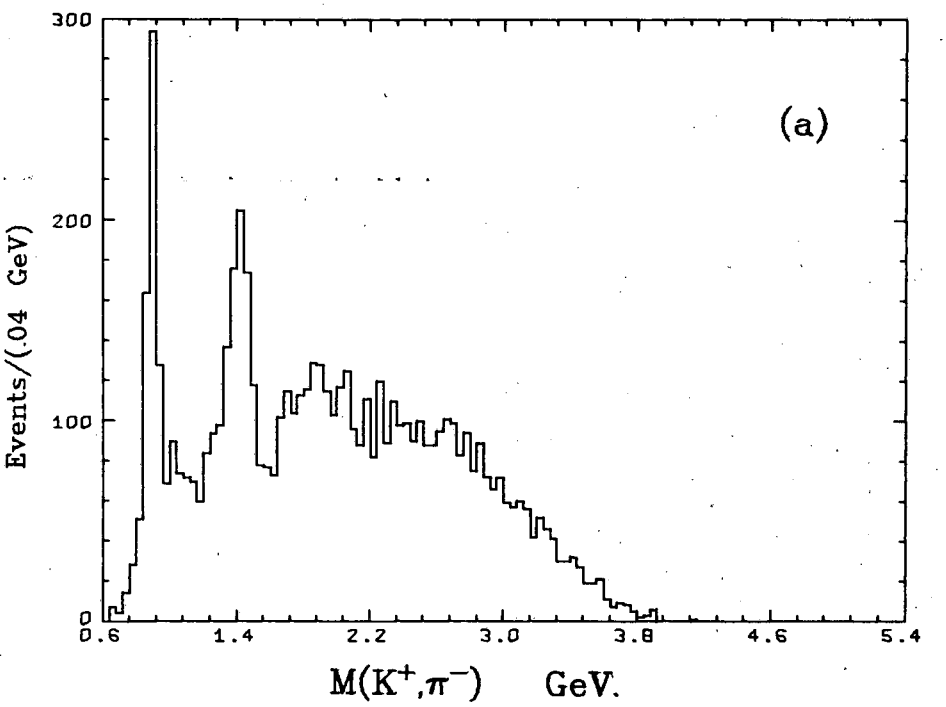

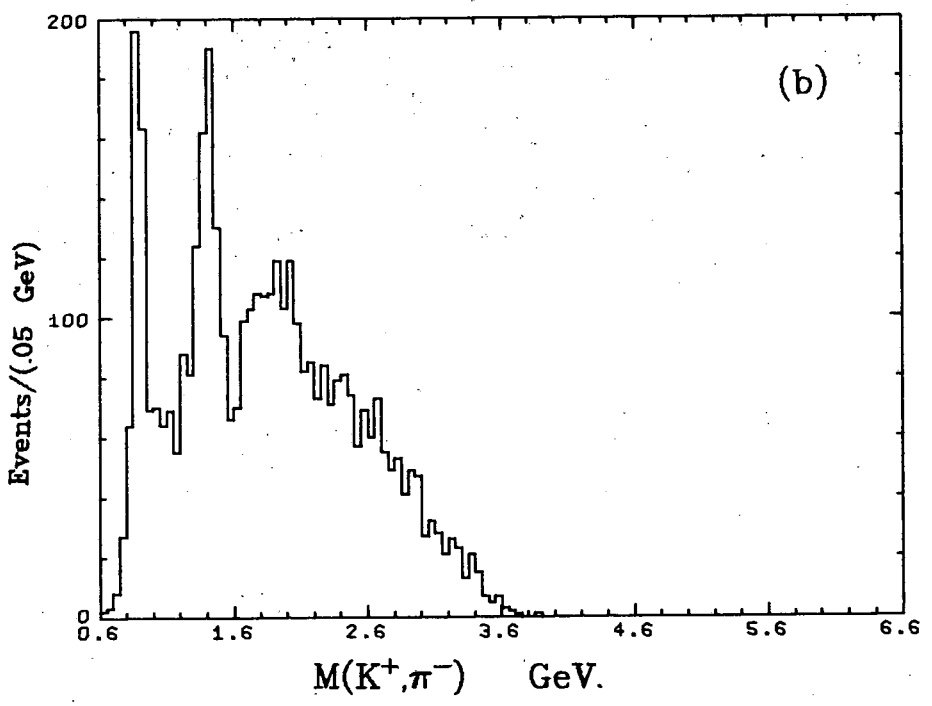

XBL 715-1013

Fig. 17

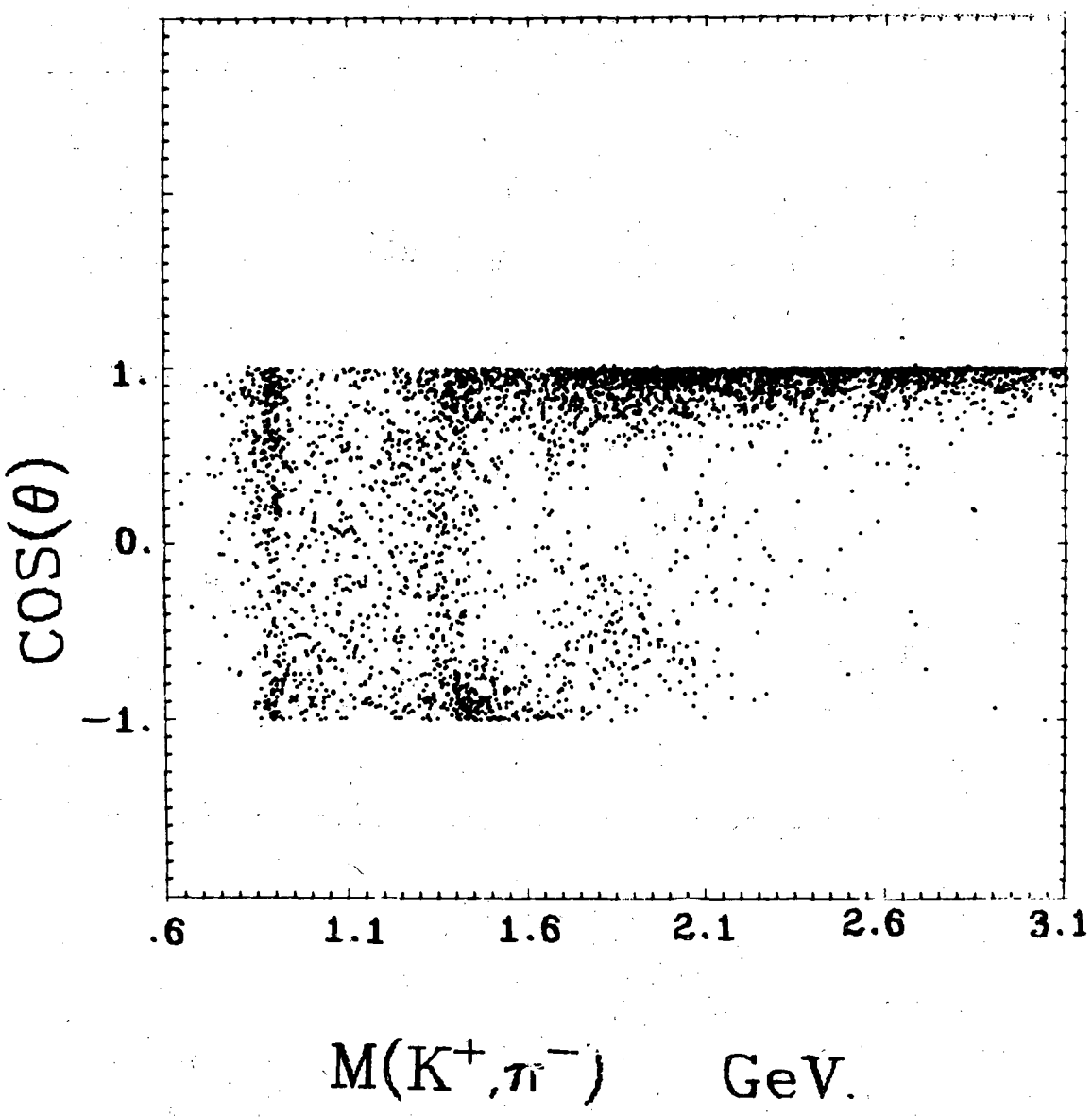

XBL 716-1117

Fig. 18

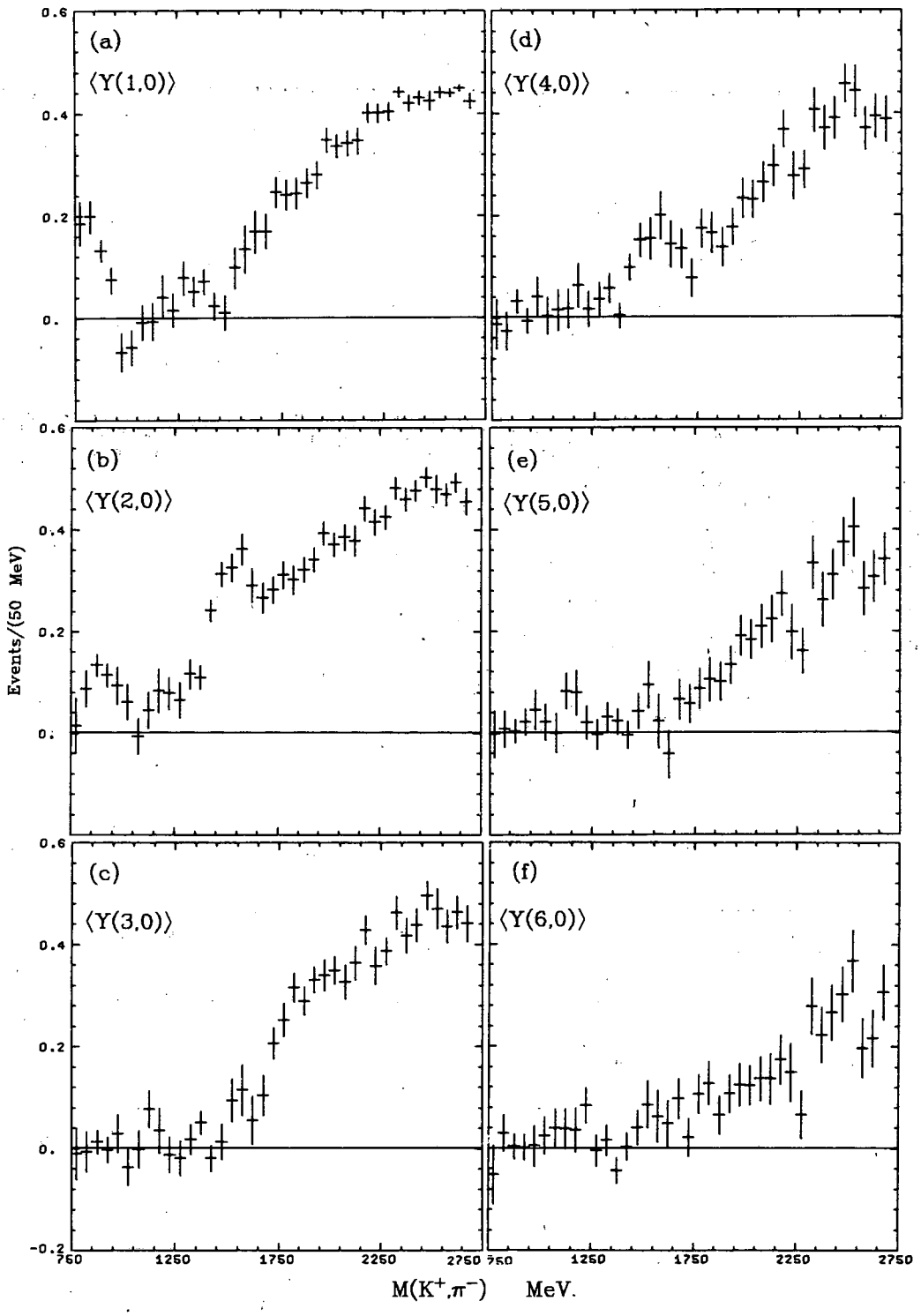
(a)
⟨Y(1,0)⟩
(b)
⟨Y(2,0)⟩
(c)
⟨Y(3,0)⟩
(d)
⟨Y(4,0)⟩
(e)
⟨Y(5,0)⟩
(f)
⟨Y(6,0)⟩
Events/(50 MeV)
M(K⁺,π⁻) MeV.
XBL 715-946

Fig. 19

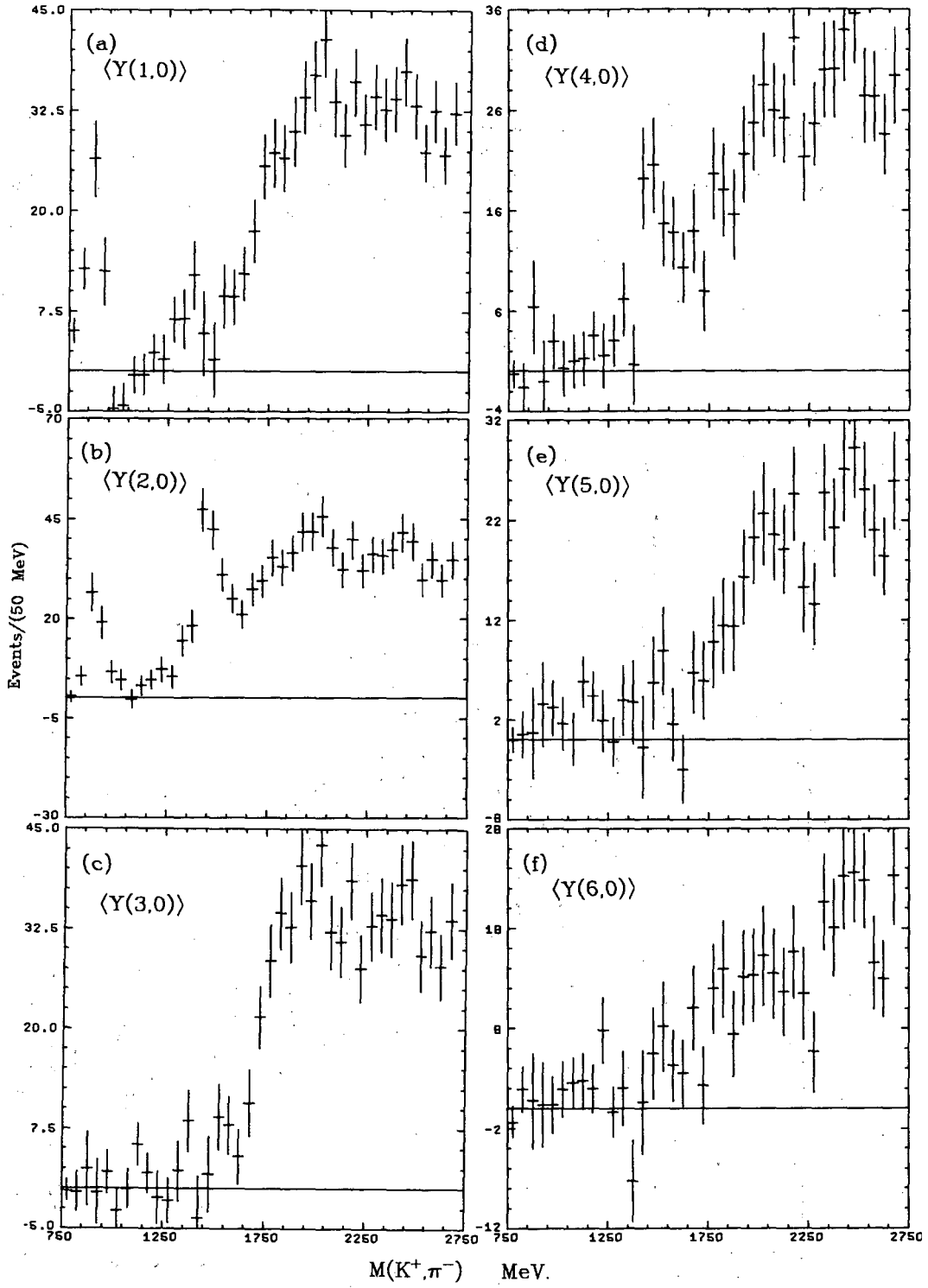

XBL 715-945

Fig. 20

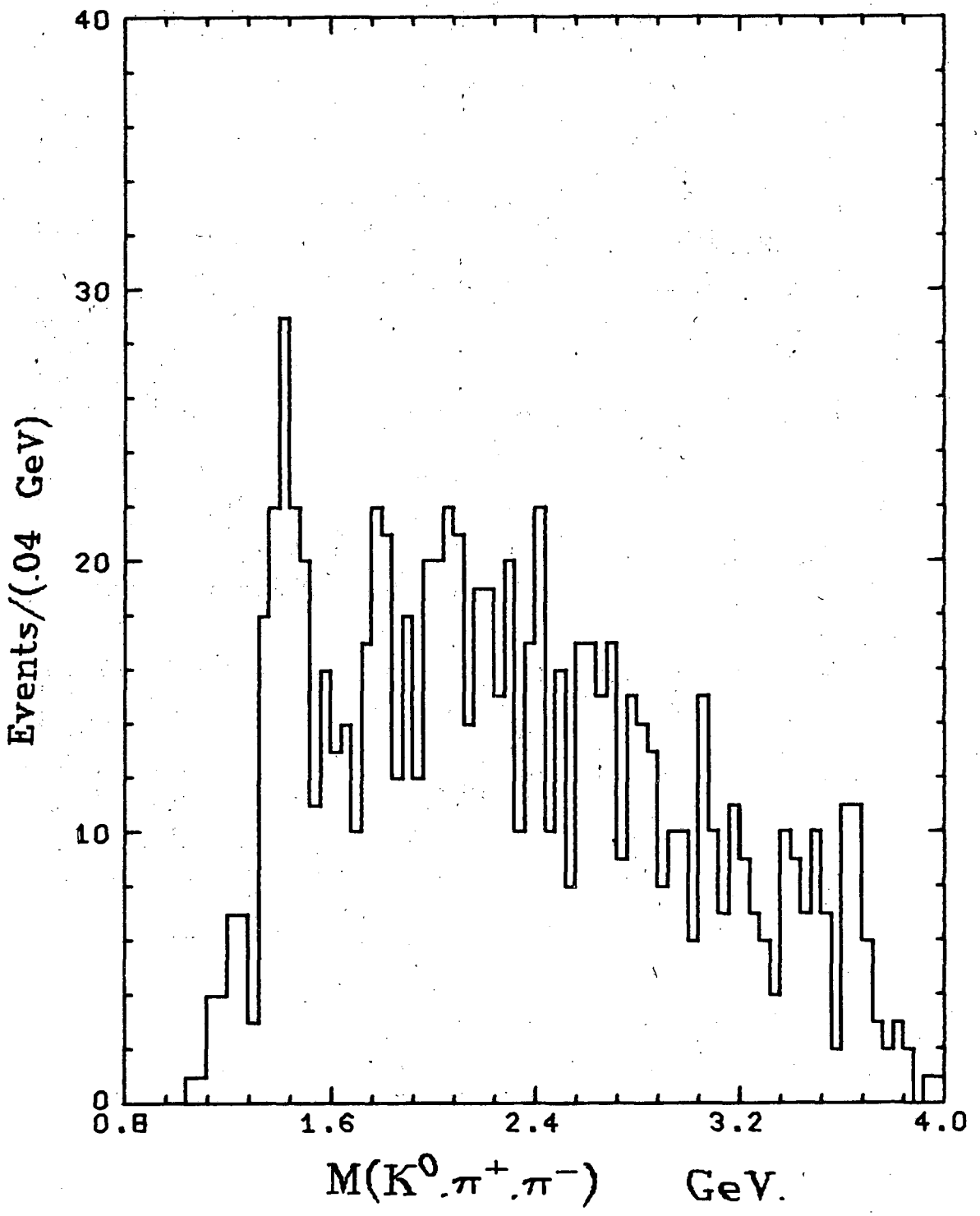

XBL 717-1219

Fig. 21

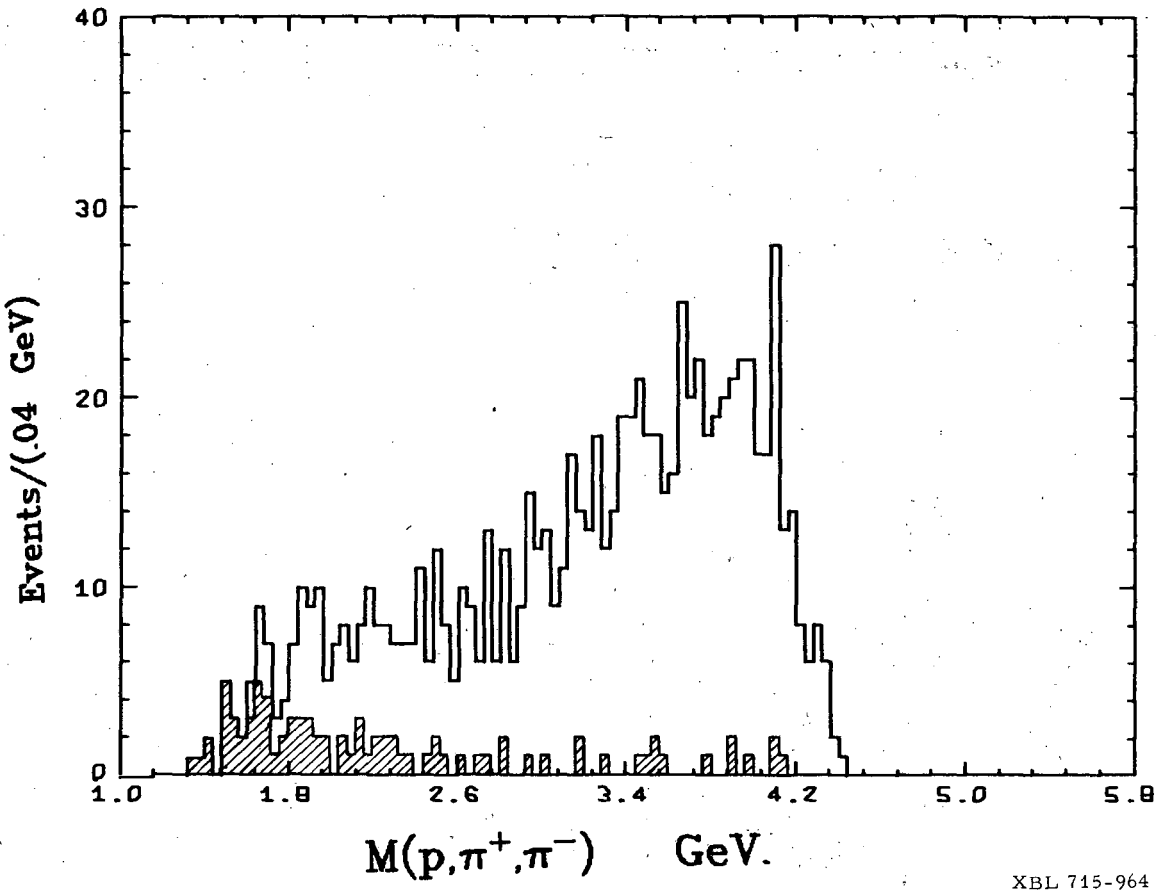

XBL 715-964

Fig. 22

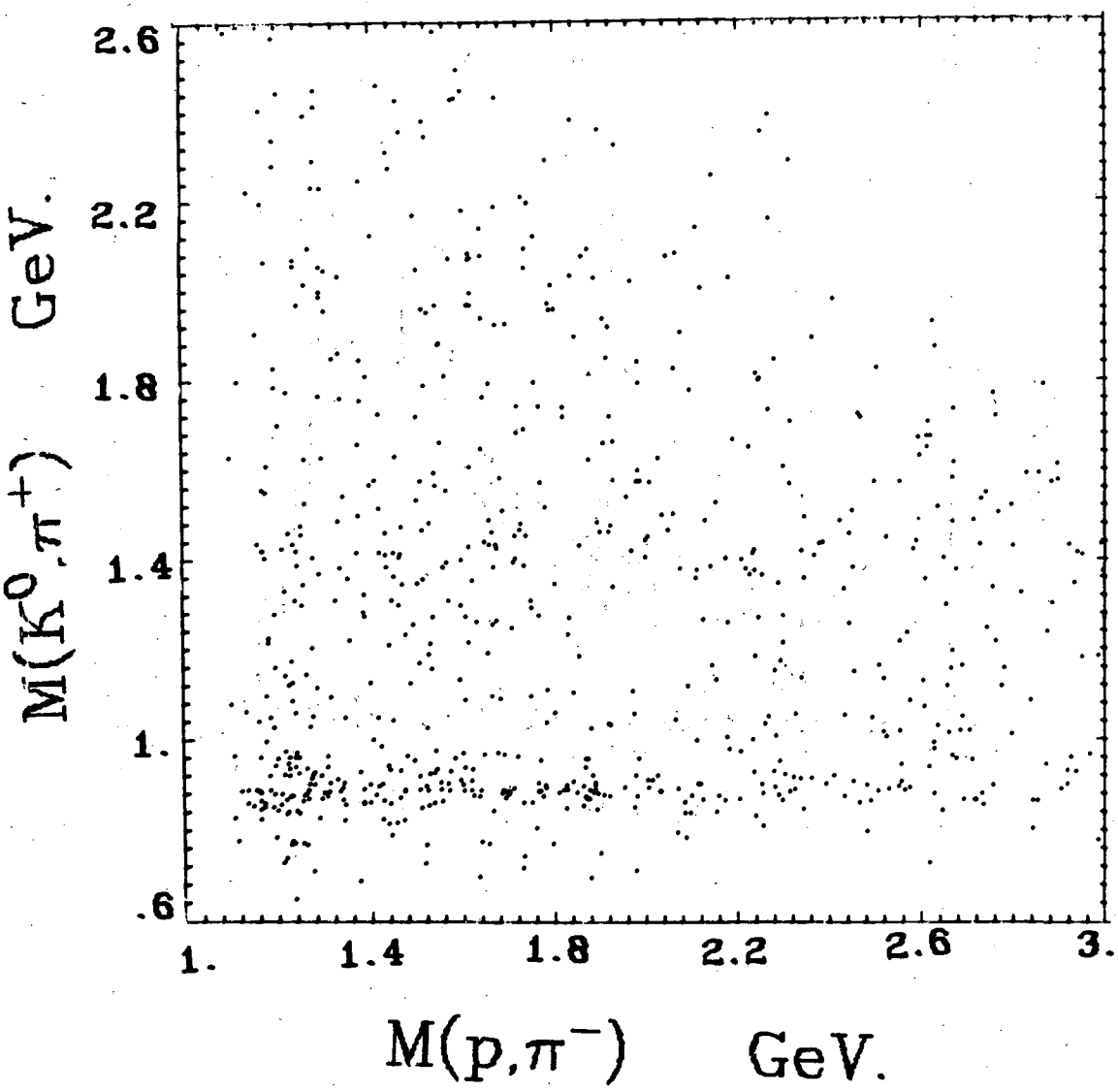

XBL 716-1122

Fig. 23

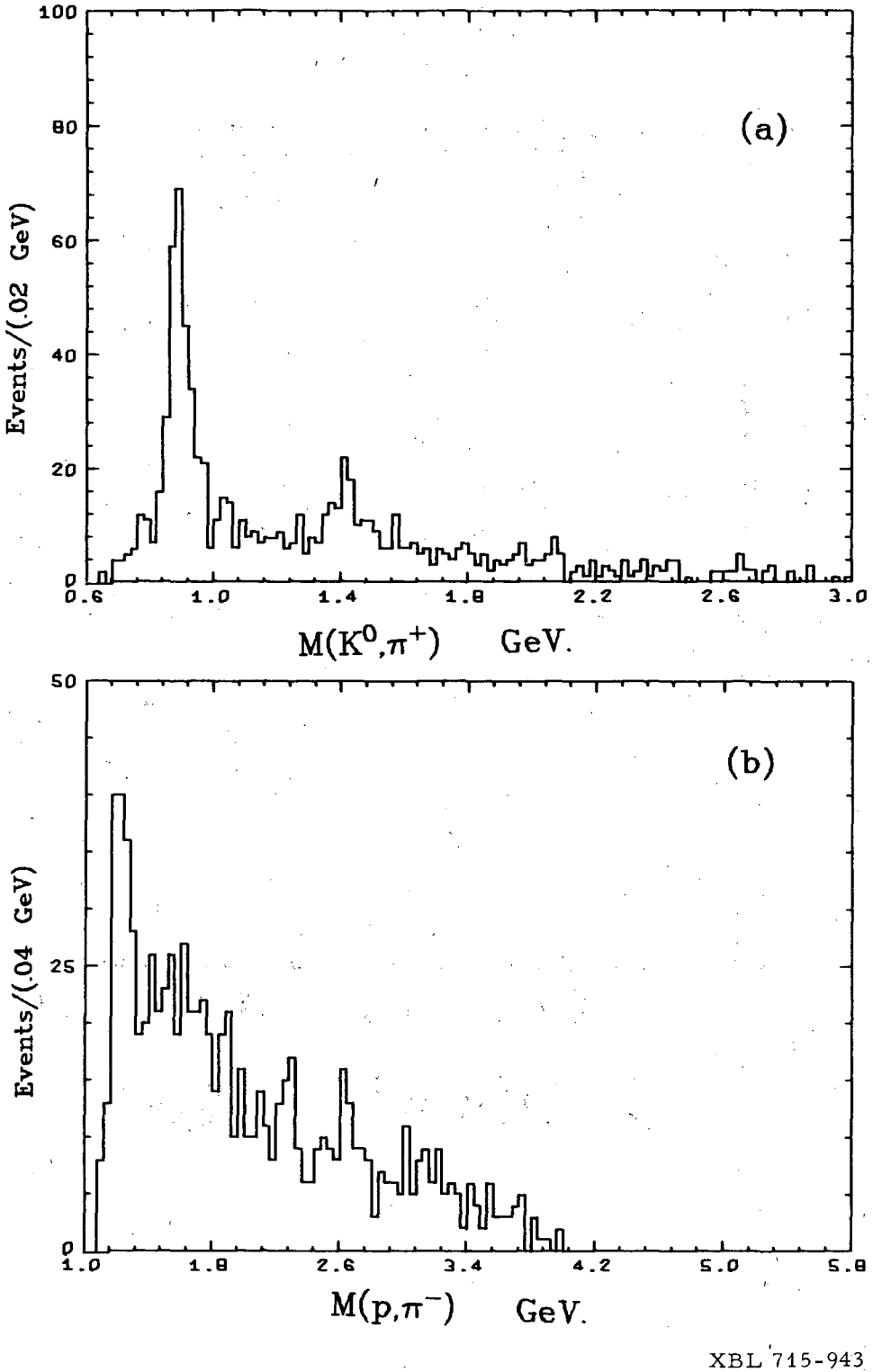
(a)
Events/(.02 GeV)
100
80
60
40
20
0
0.6
1.0
1.4
1.8
2.2
2.6
3.0
M(K⁰,π⁺) GeV.
(b)
Events/(.04 GeV)
50
25
0
1.0
1.8
2.6
3.4
4.2
5.0
5.8
M(p,π⁻) GeV.
XBL 715-943

Fig. 24

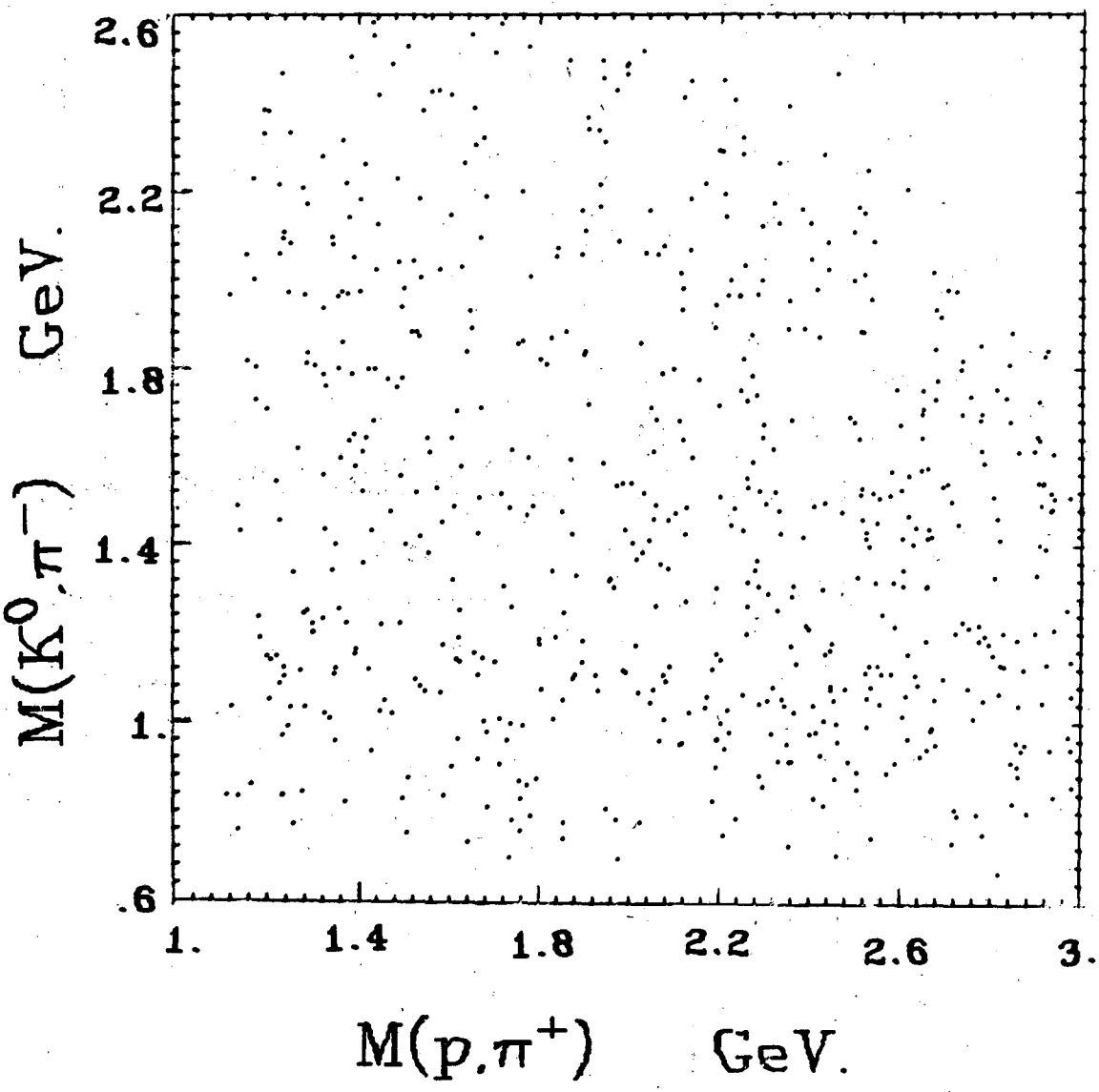

XBL 716-1121

Fig. 25

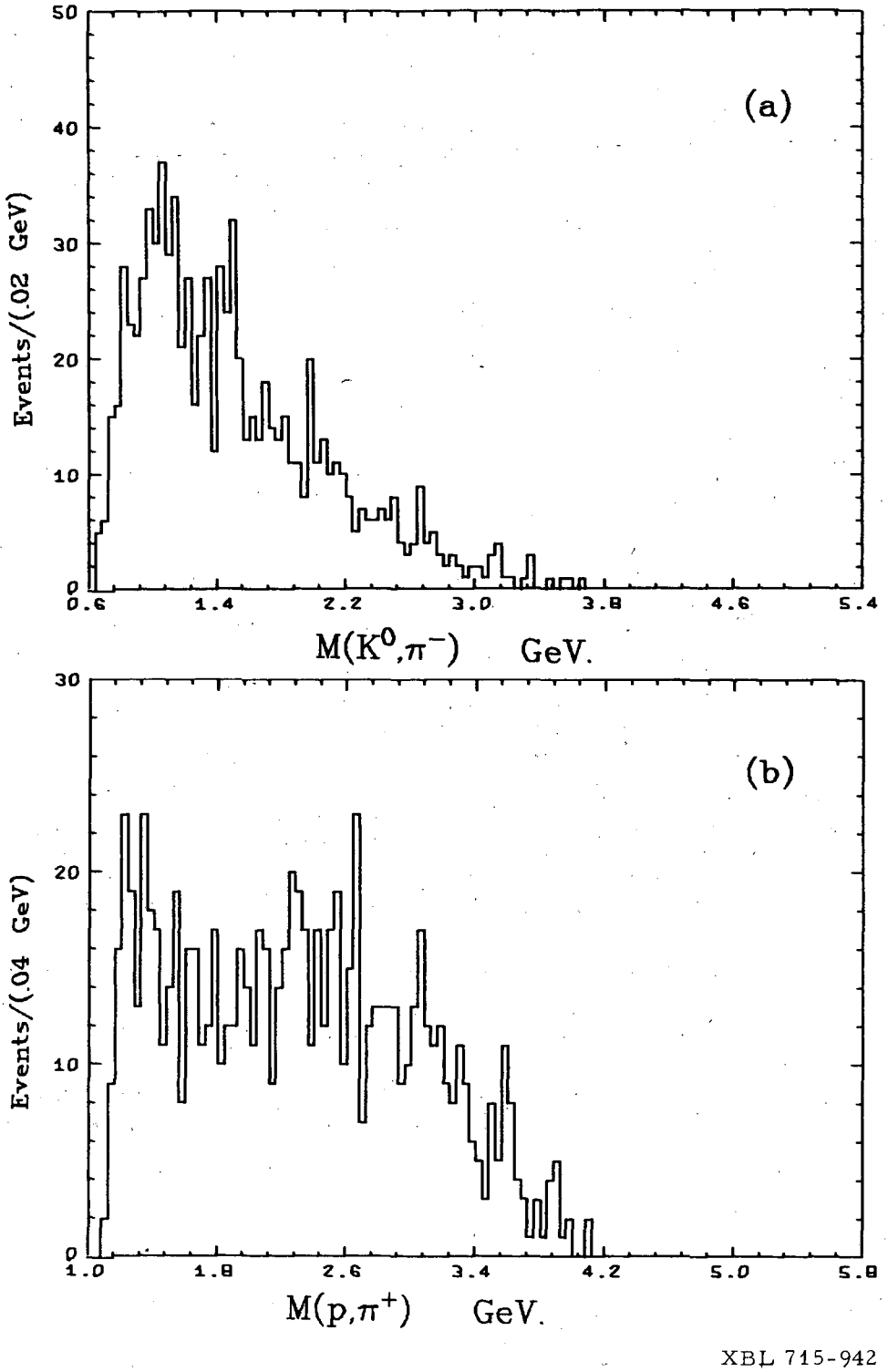

Fig. 26

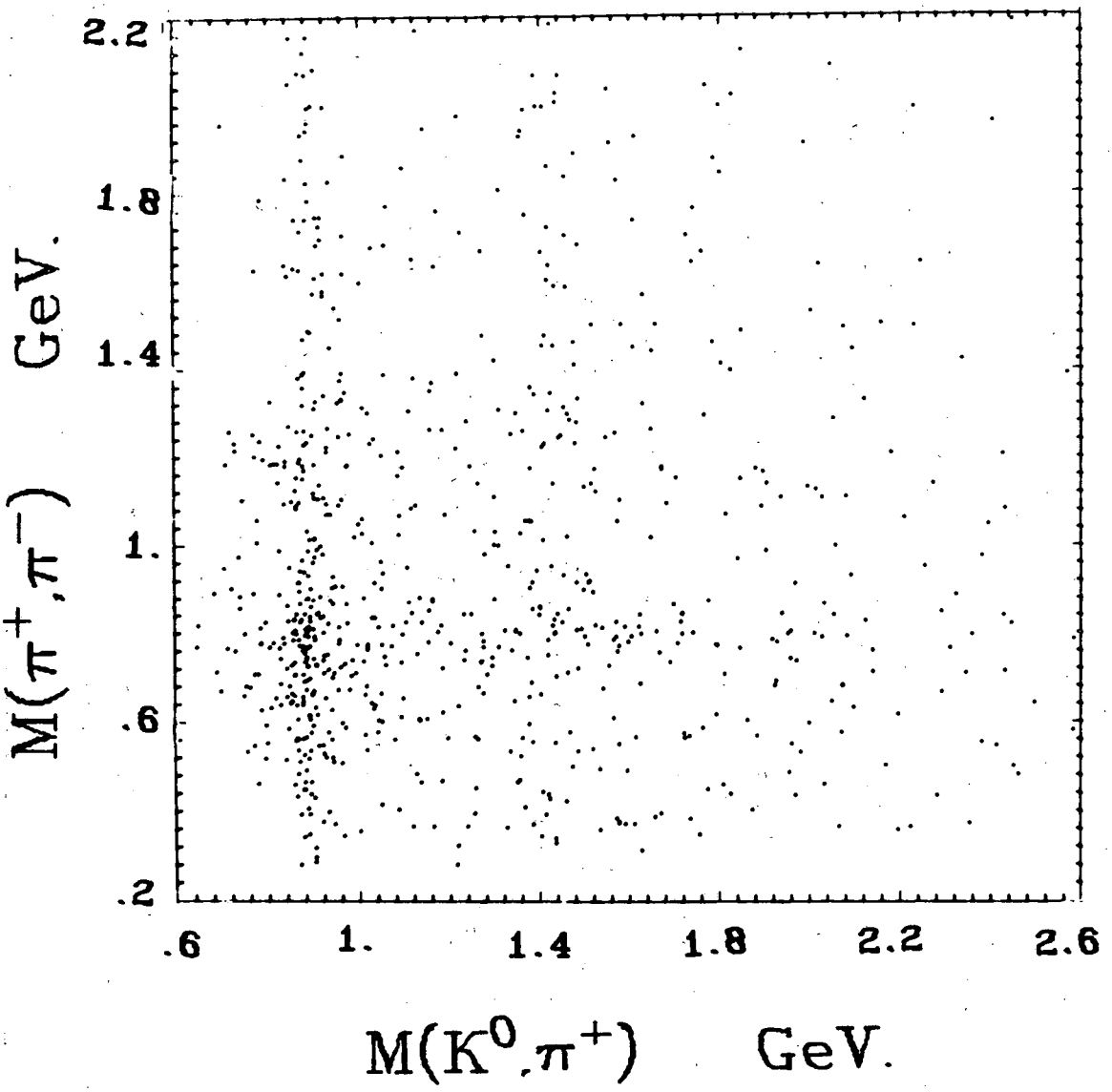

XBL 716-1120

Fig. 27

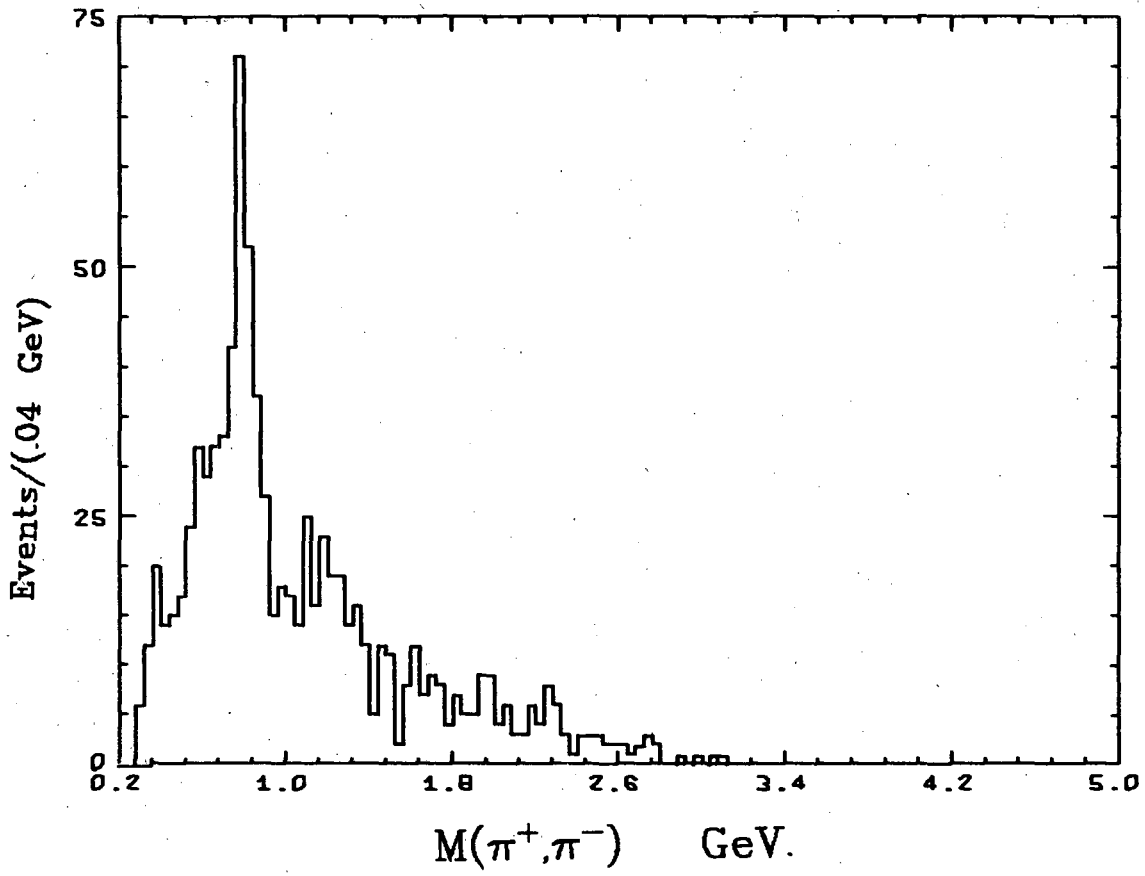

XBL 715-953

Fig. 28

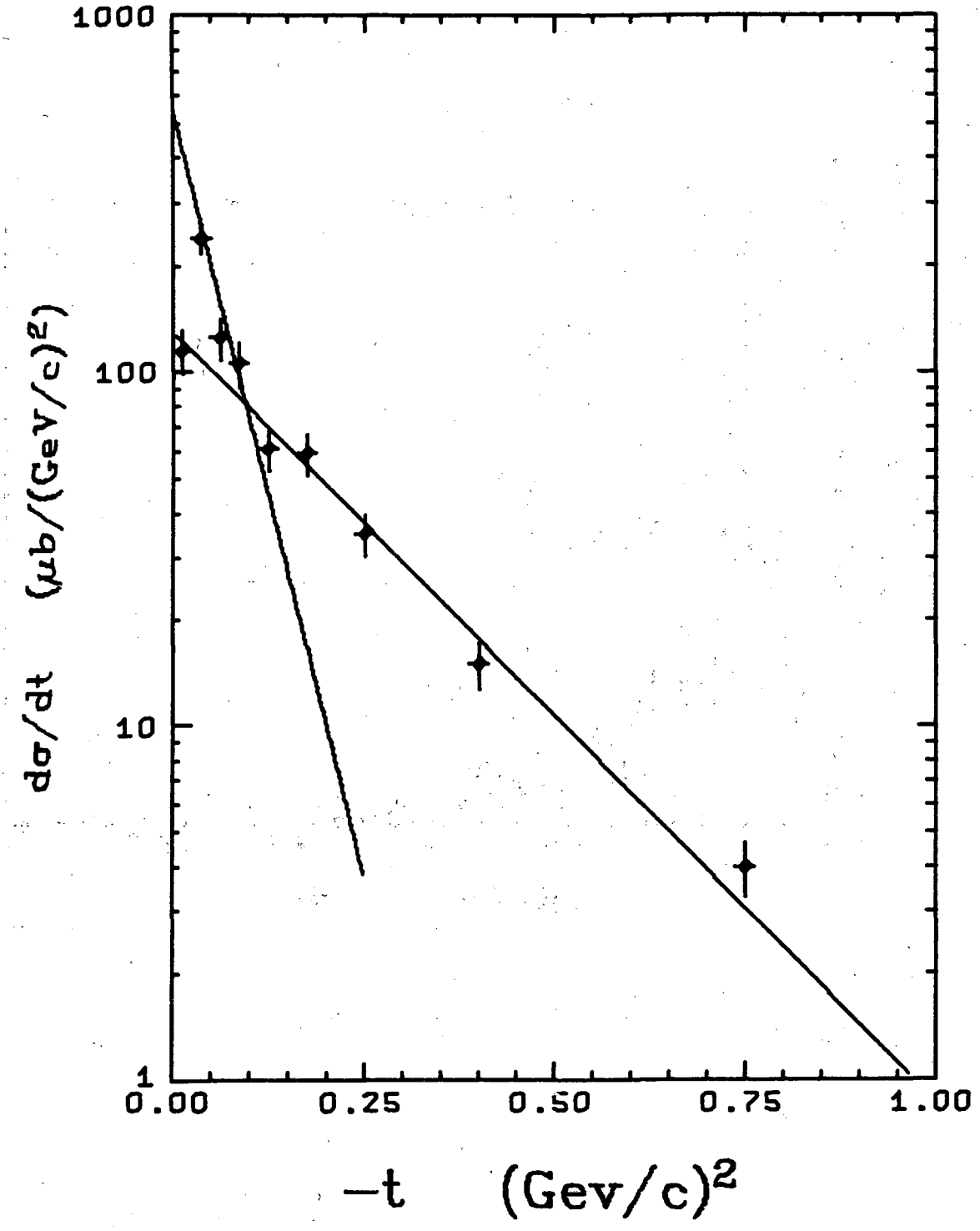

XBL 715-1001

Fig. 29

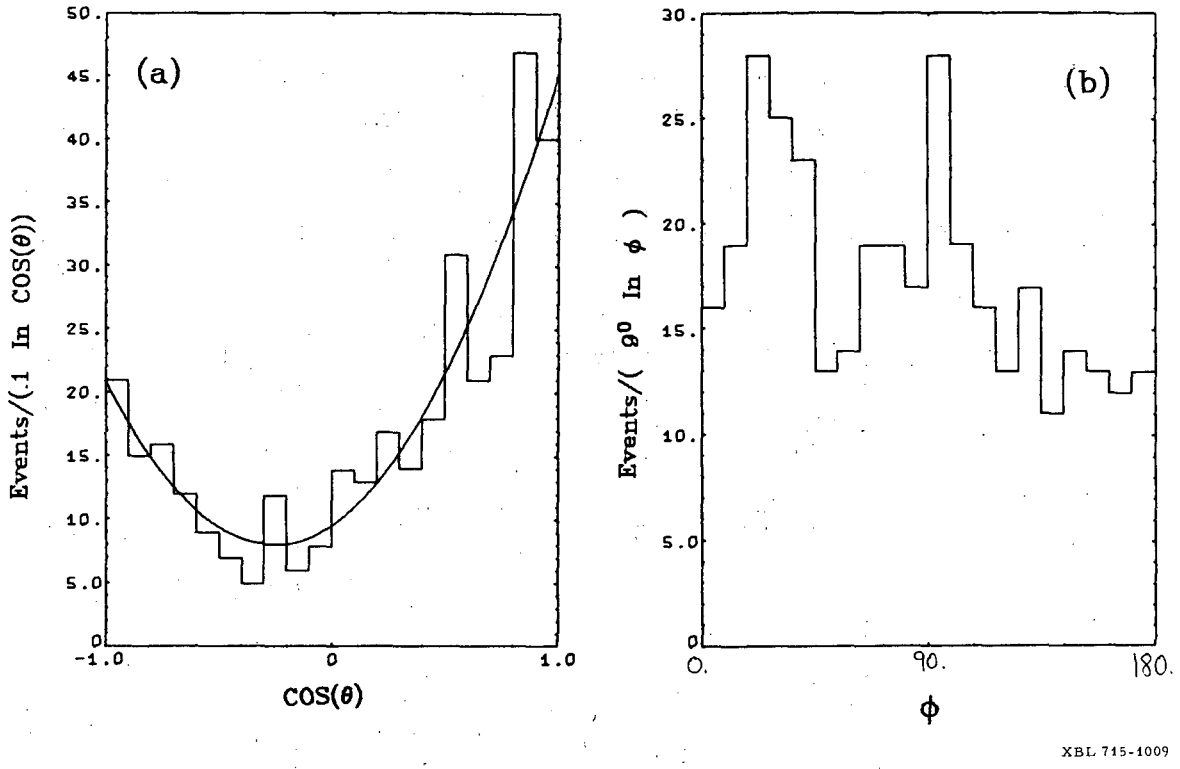
(a)
Events/(.1 ln COS(θ))
COS(θ)
50.
45.
40.
35.
30.
25.
20.
15.
10.
5.0
0
-1.0
0
1.0
(b)
Events/(g0 ln φ)
φ
30.
25.
20.
15.
10.
5.0
0
0.
90.
180.
XBL 715-1009

Fig. 30

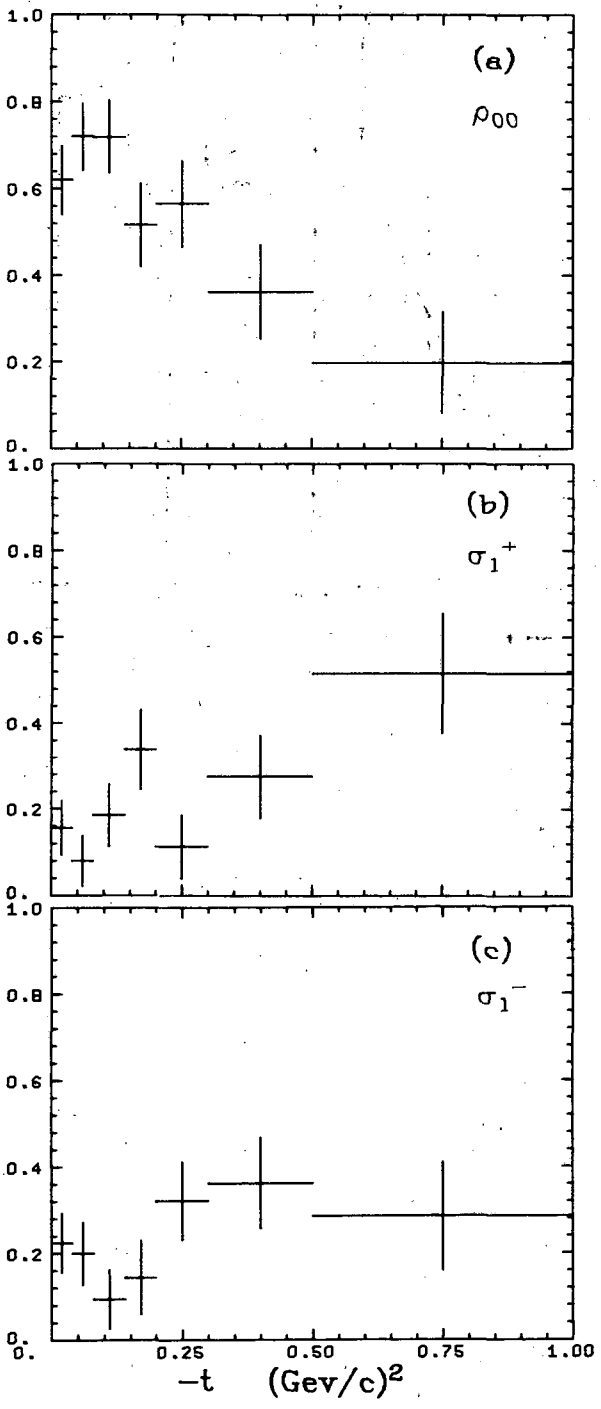

XBL 715-1012

Fig. 31

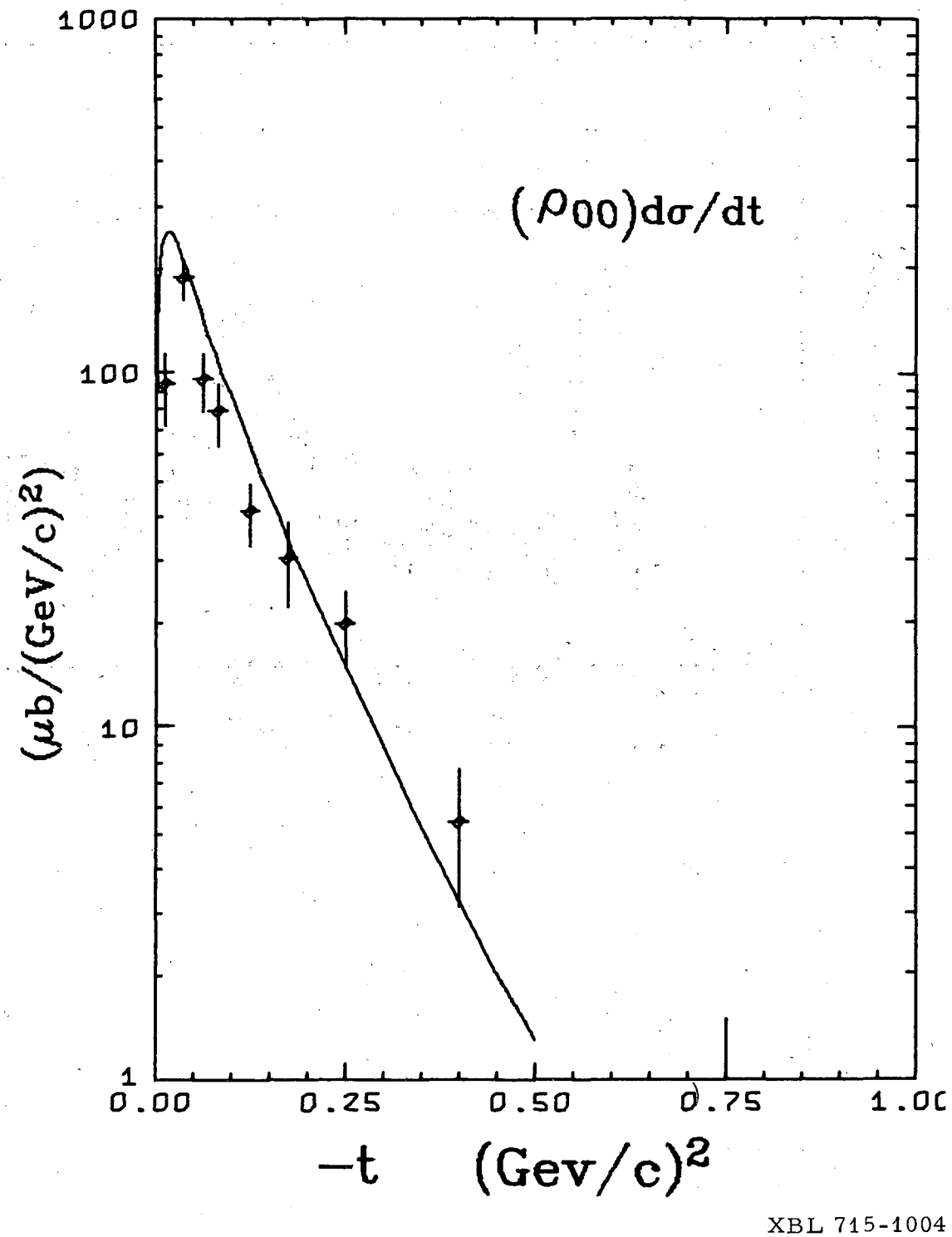

XBL 715-1004

Fig. 32

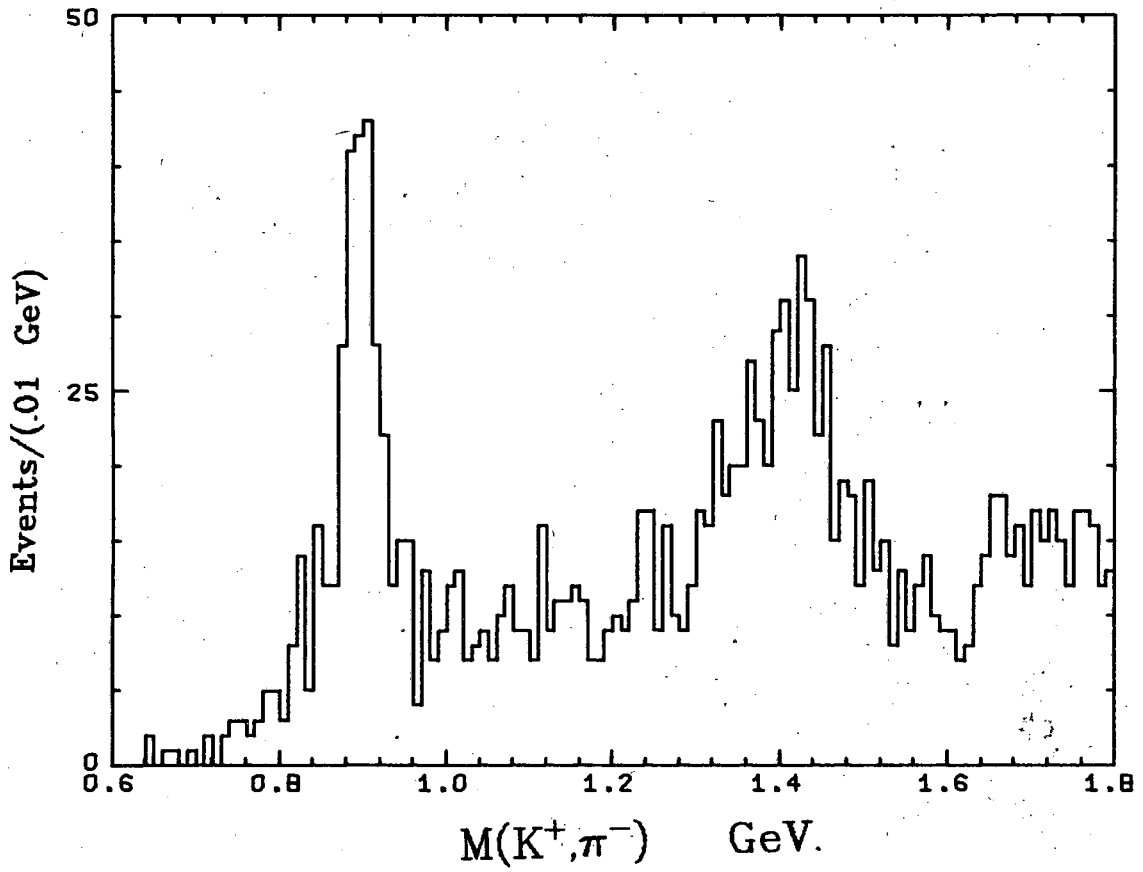

XBL 715-1003

Fig. 33

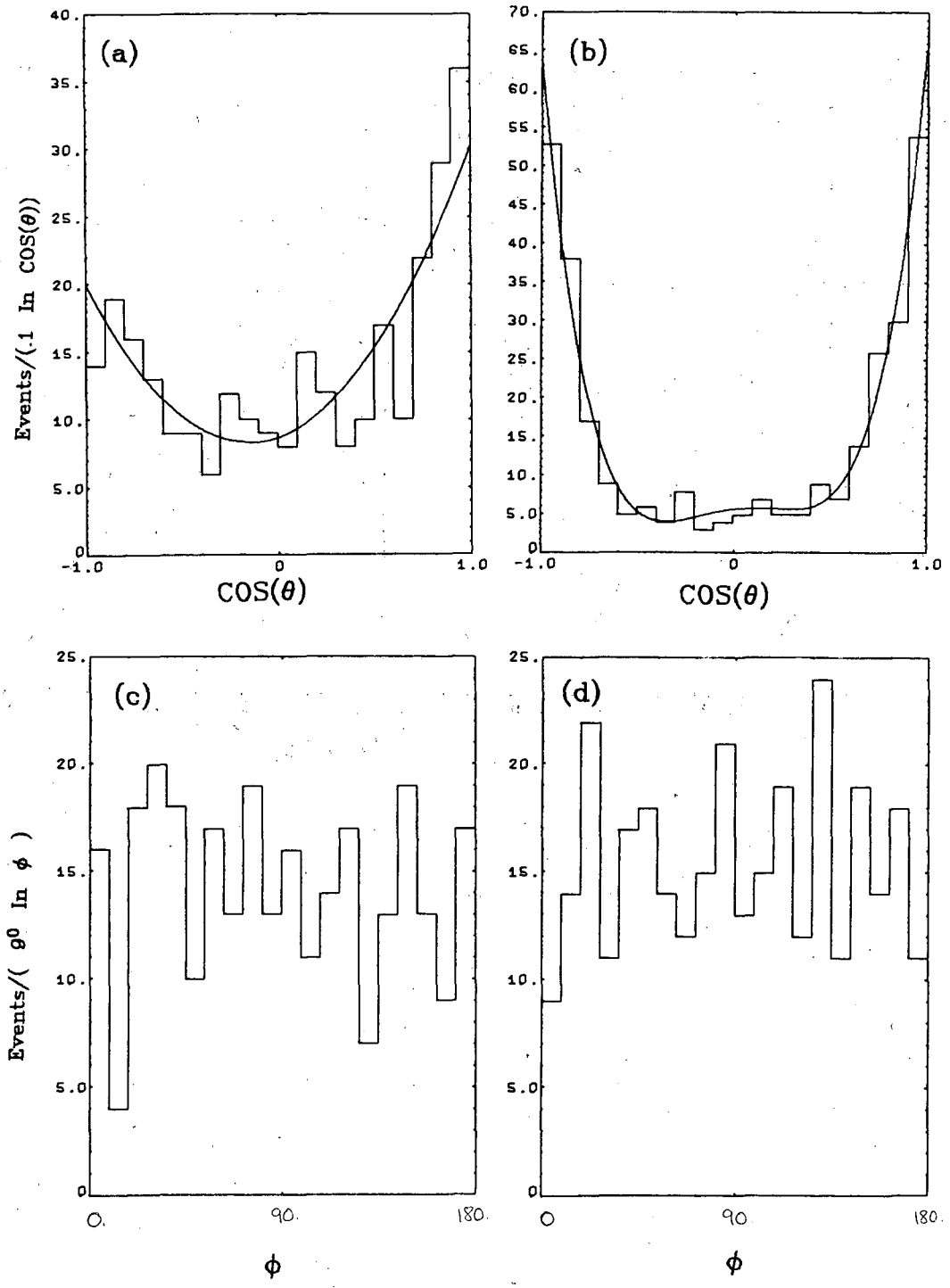

Fig. 34

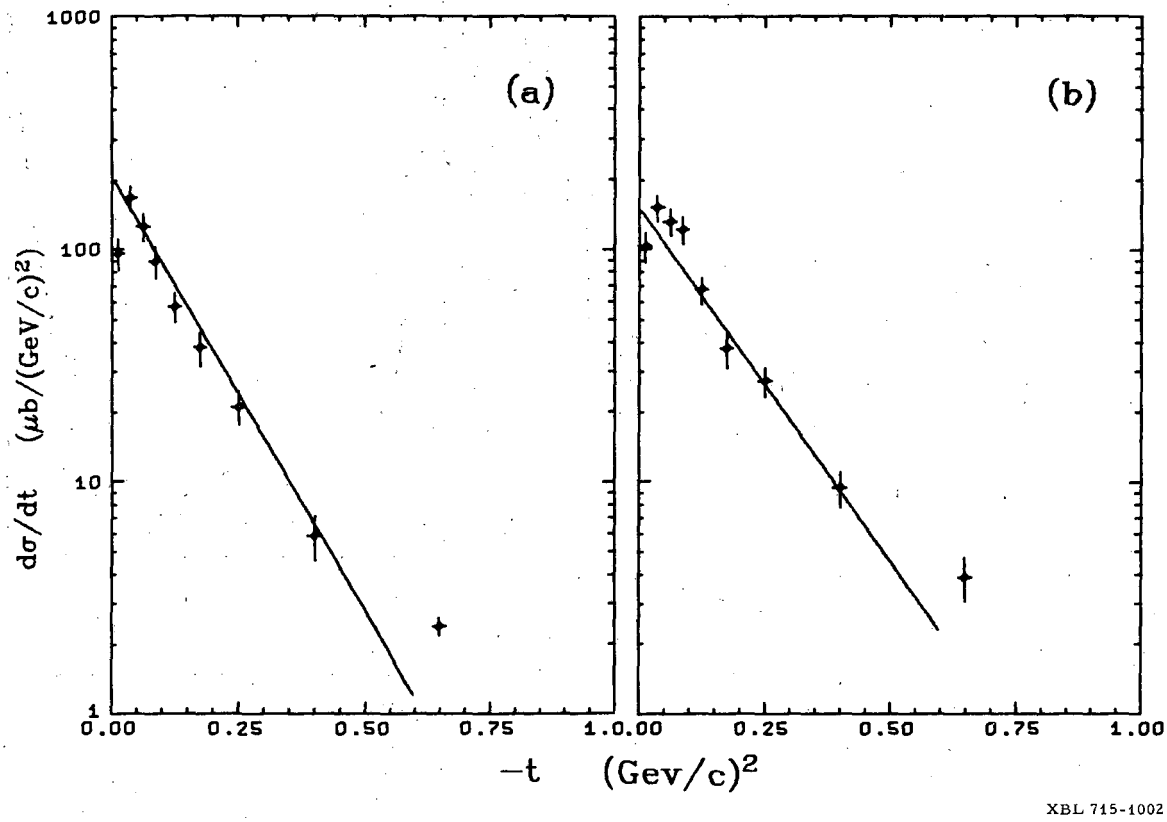
1000
100
10
1
dσ/dt (μb/(GeV/c)²)
(a)
(b)
0.00
0.25
0.50
0.75
1.00
−t (Gev/c)²
XBL 715-1002

Fig. 35

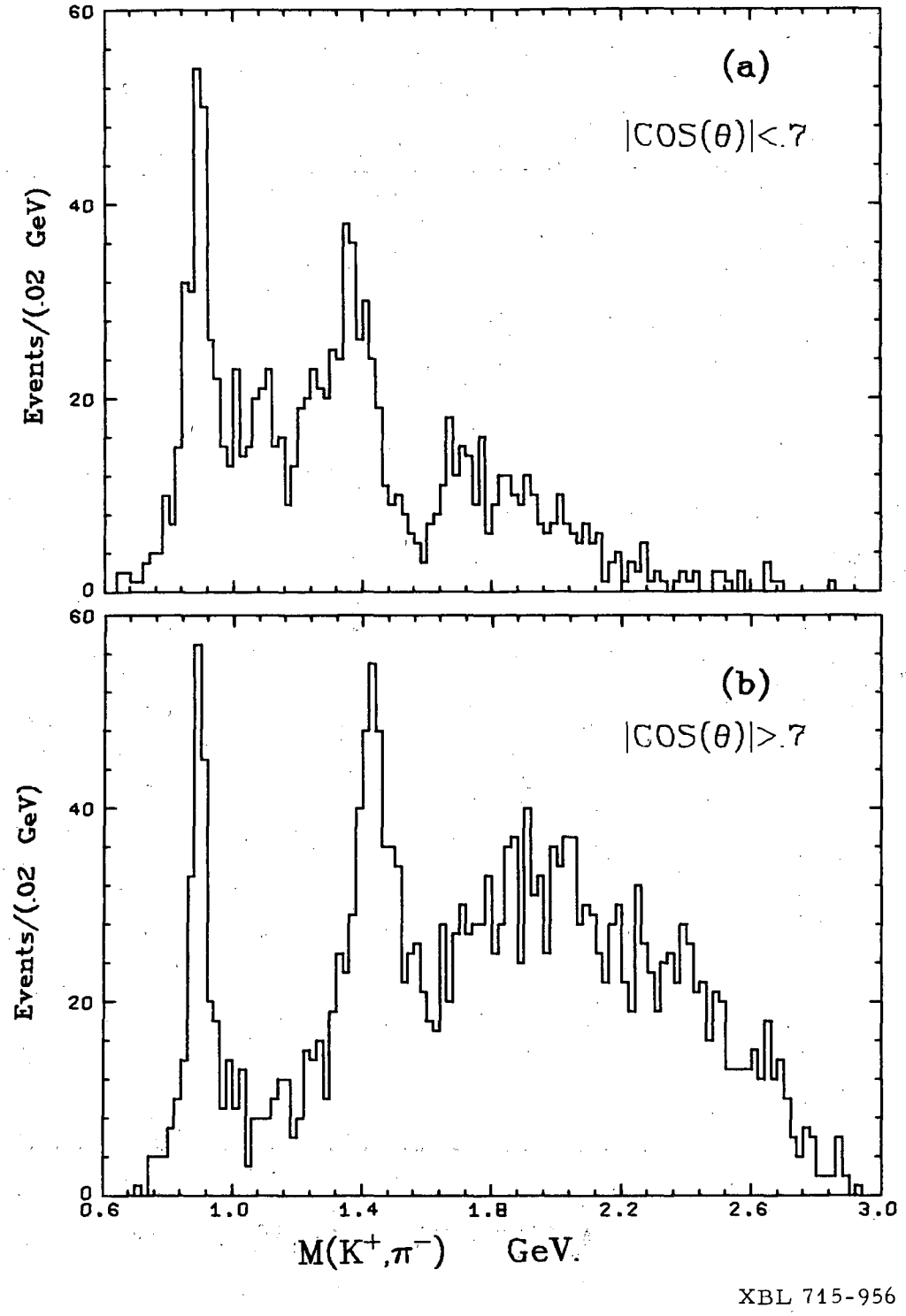
(a)
|COS(θ)|<.7
(b)
|COS(θ)|>.7
Events/(.02 GeV)
Events/(.02 GeV)
0
20
40
60
0.6
1.0
1.4
1.8
2.2
2.6
3.0
M(K⁺,π⁻) GeV.
XBL 715-956

Fig. 36

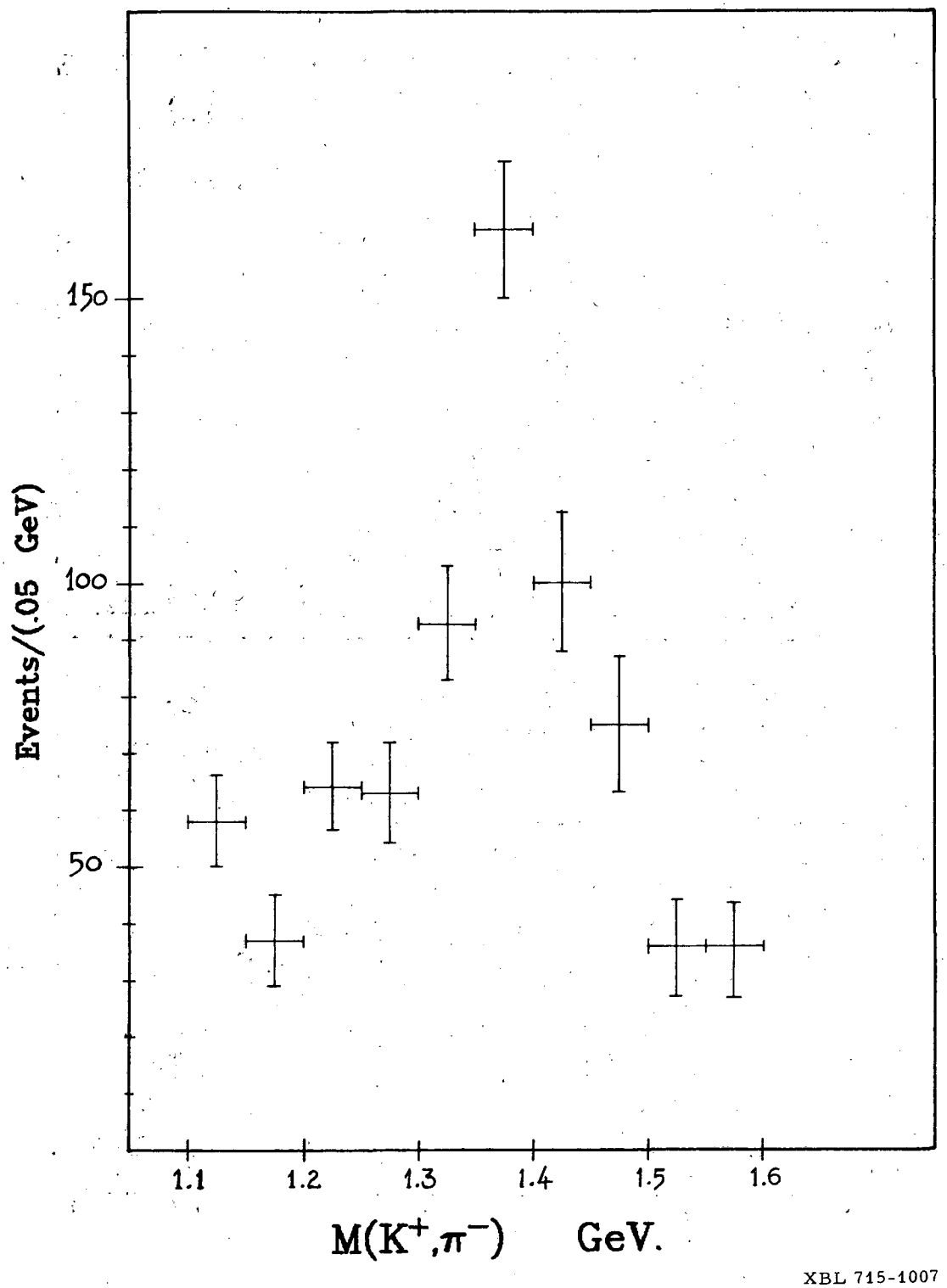

Fig. 37

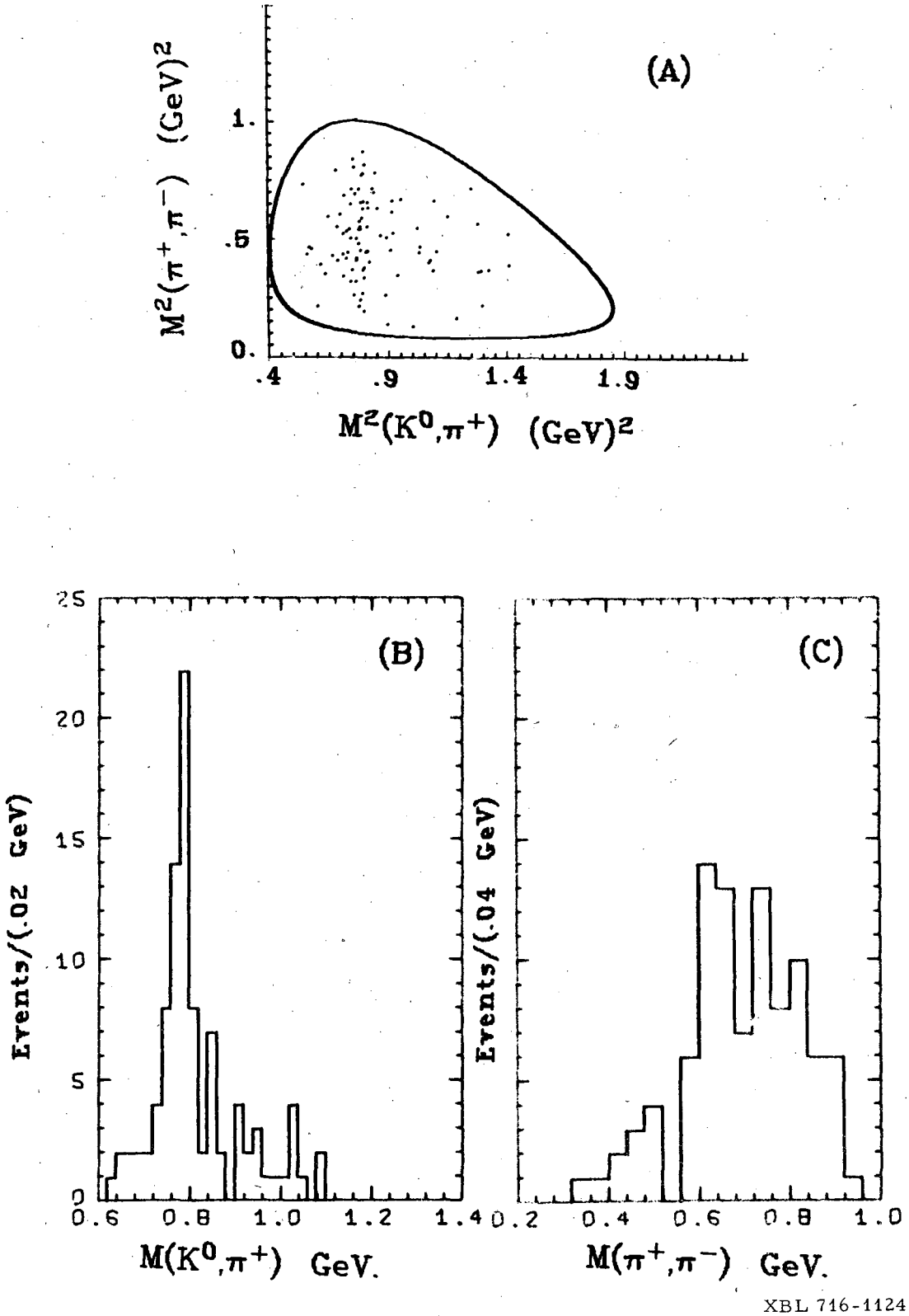
(A)
$M^2(\pi^+,\pi^-)$ (GeV)^2
1.
.5
0.
.4
.9
1.4
1.9
$M^2(K^0,\pi^+)$ (GeV)^2
(B)
Events/(.02 GeV)
25
20
15
10
5
0
0.6
0.8
1.0
1.2
1.4
$M(K^0,\pi^+)$ GeV.
(C)
Events/(.04 GeV)
0.2
0.4
0.6
0.8
1.0
$M(\pi^+,\pi^-)$ GeV.
XBL 716-1124

Fig. 38

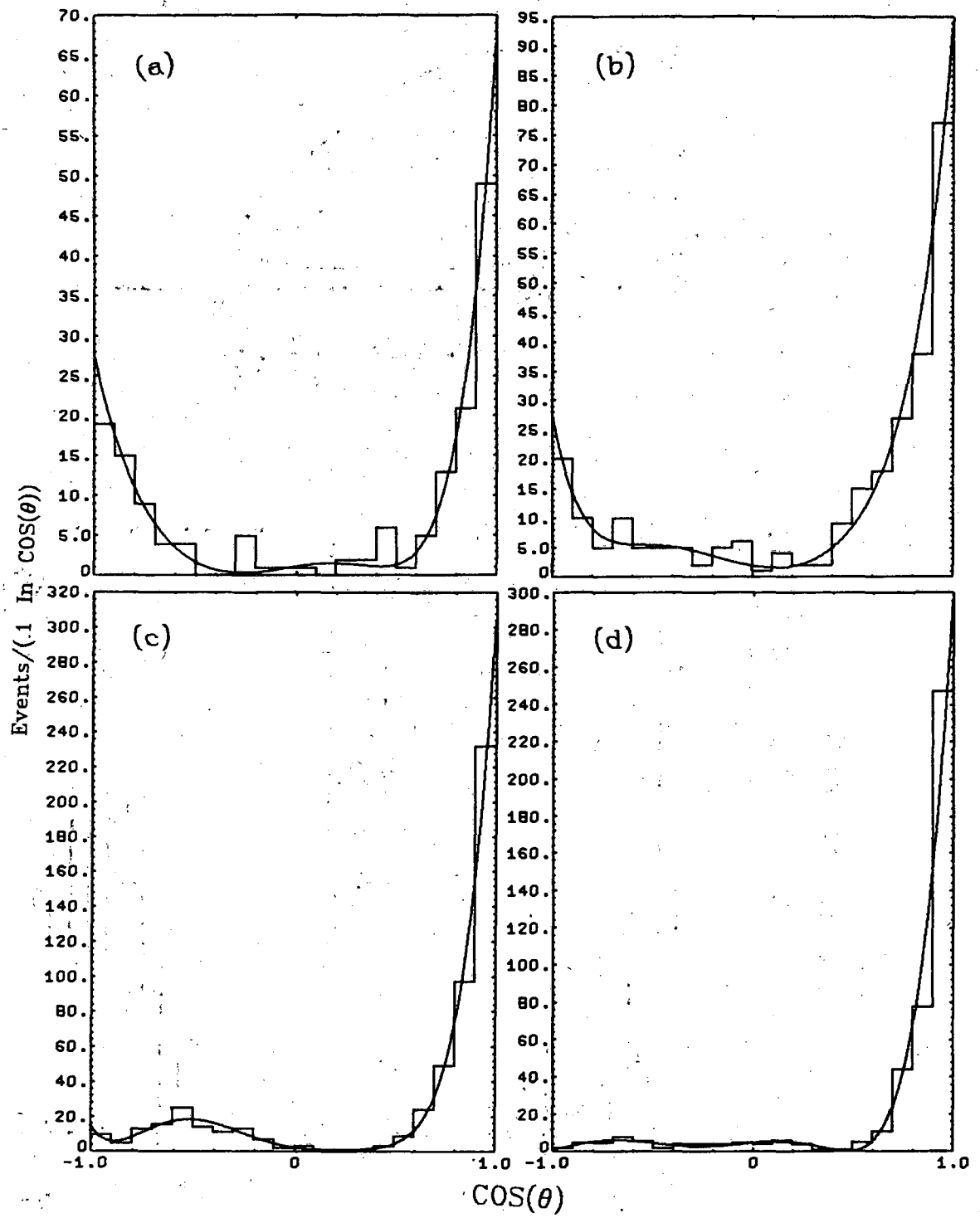

Fig. 39

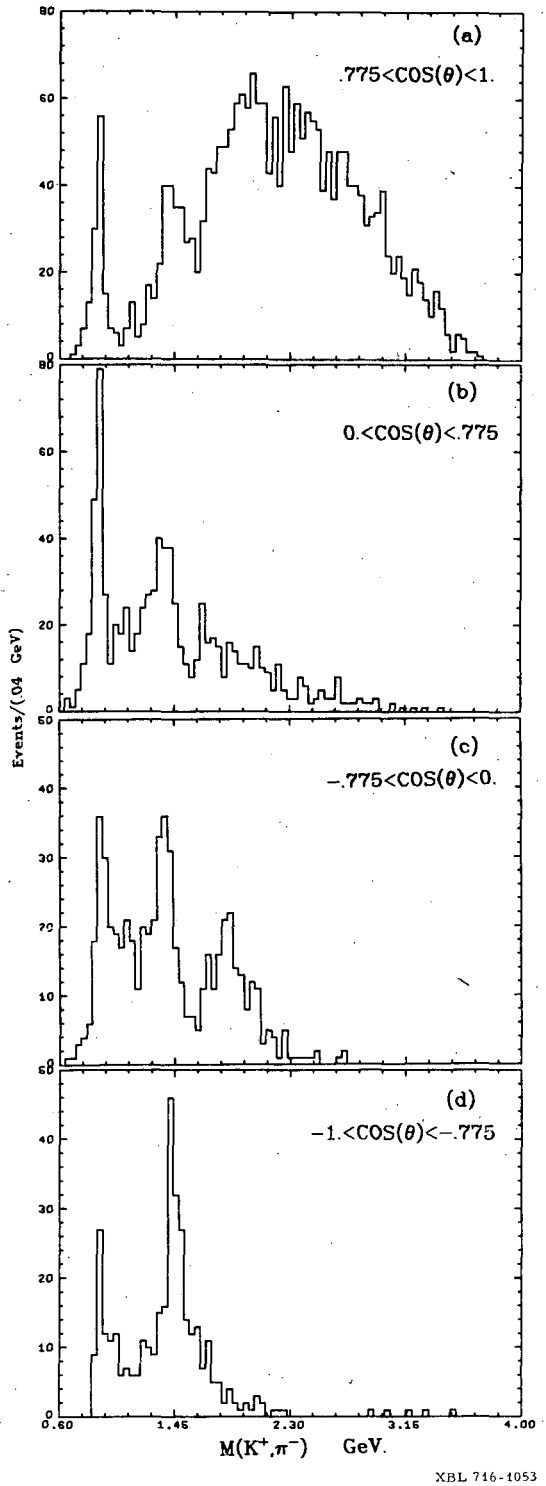
(a)
.775<COS(θ)<1.
(b)
0.<COS(θ)<.775
(c)
-.775<COS(θ)<0.
(d)
-1.<COS(θ)<-.775
Events/(.04 GeV)
M(K⁺,π⁻) GeV.
XBL 716-1053

Fig. 40

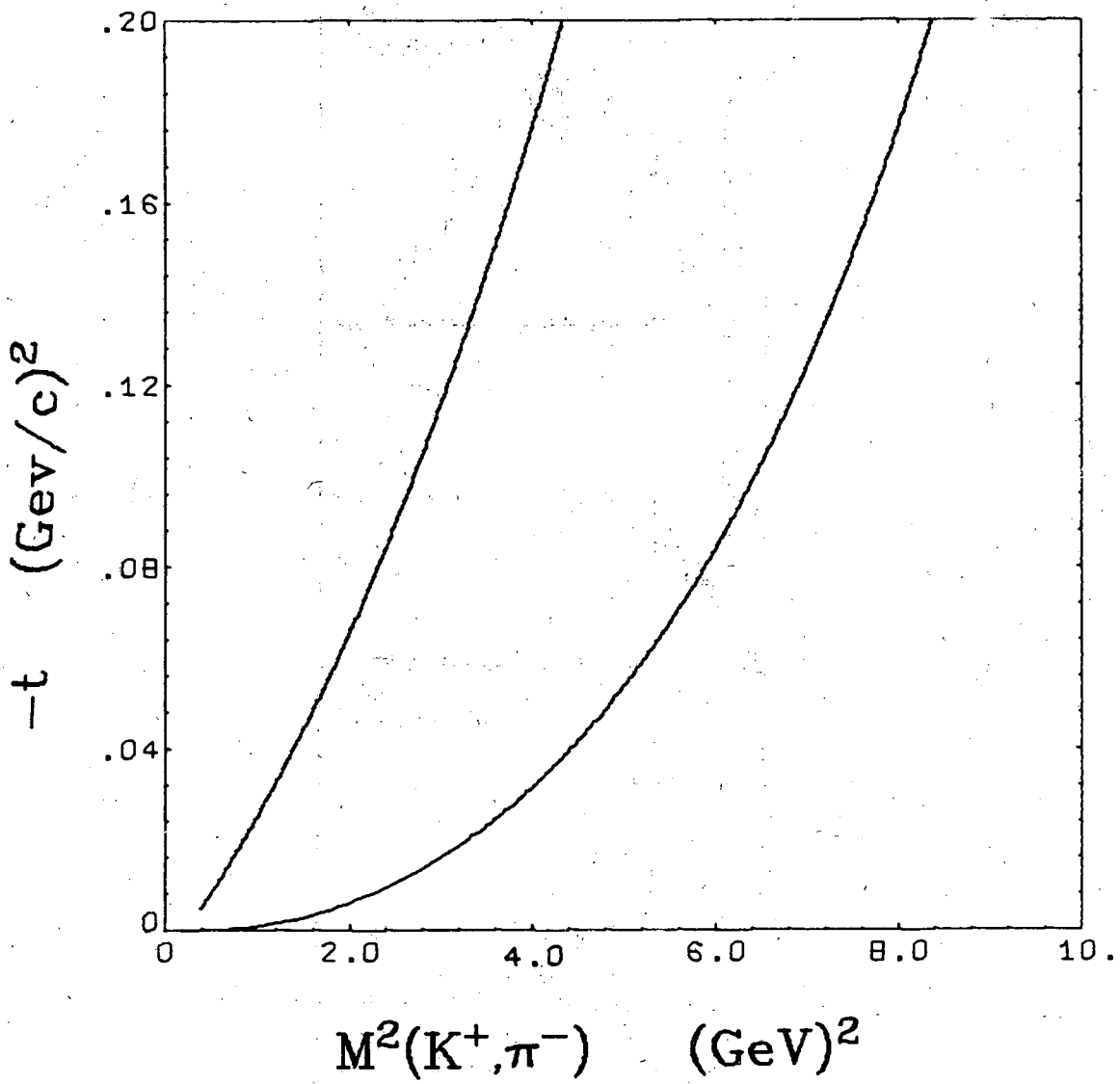

XBL 715-935

Fig. 41

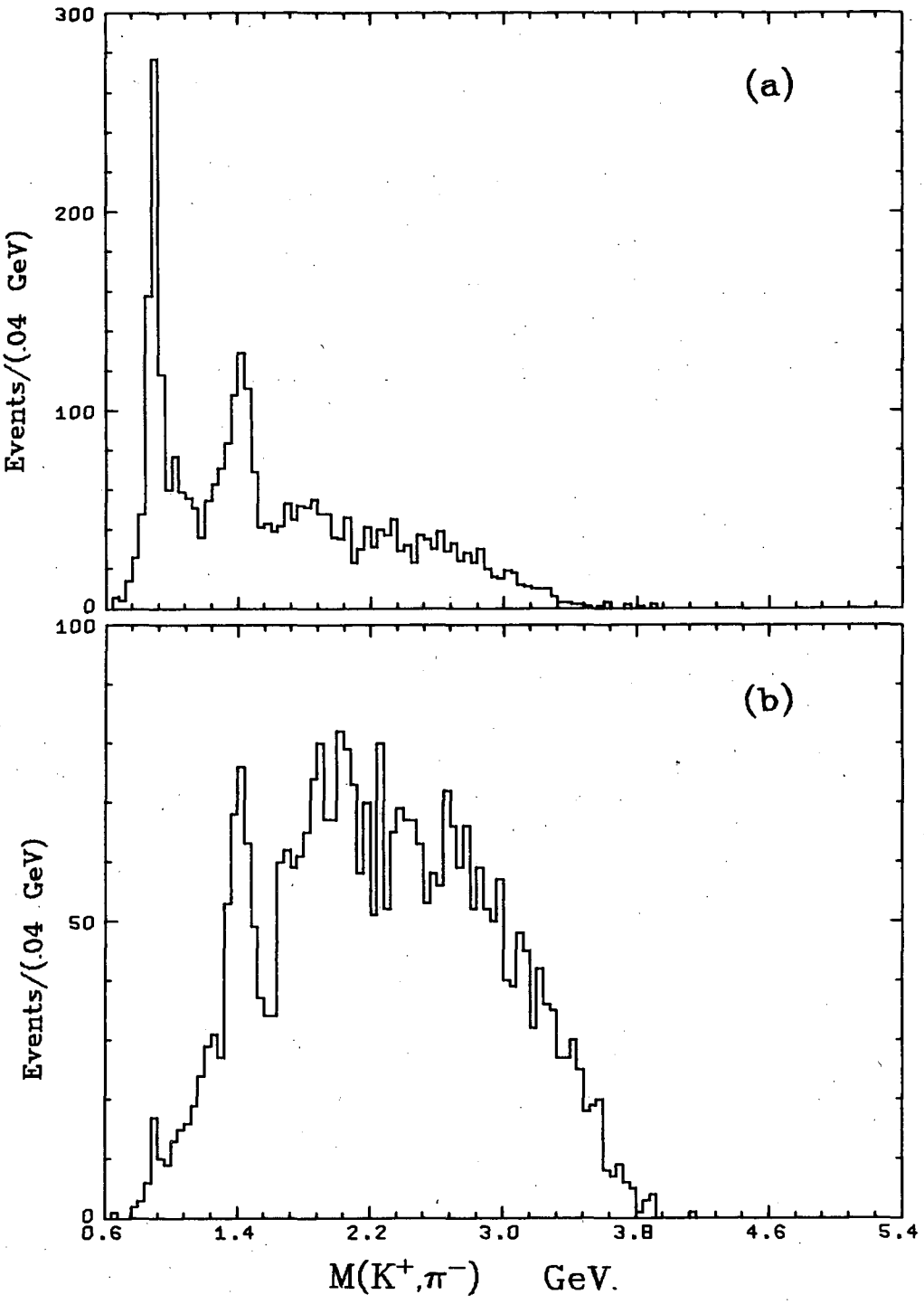

XBL 715-960

Fig. 42

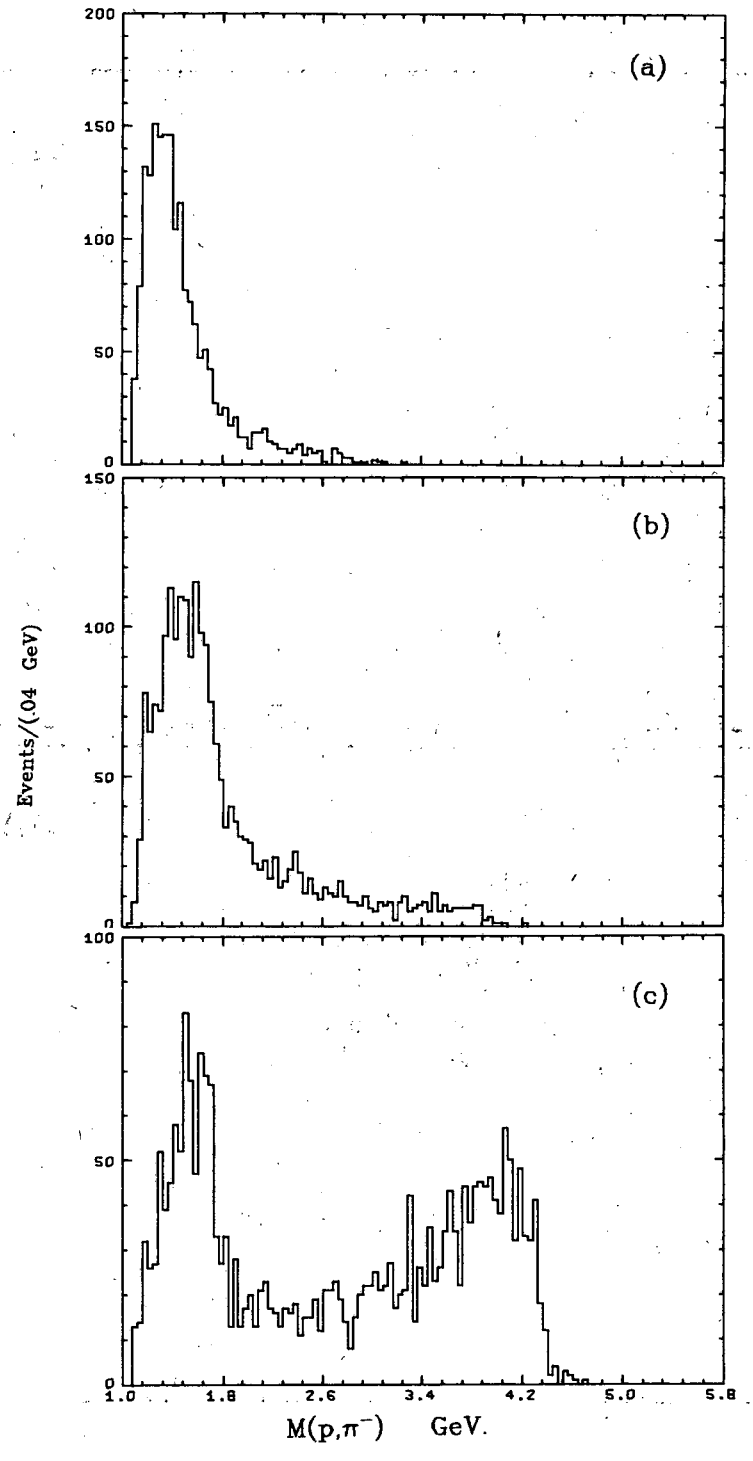

Fig. 43

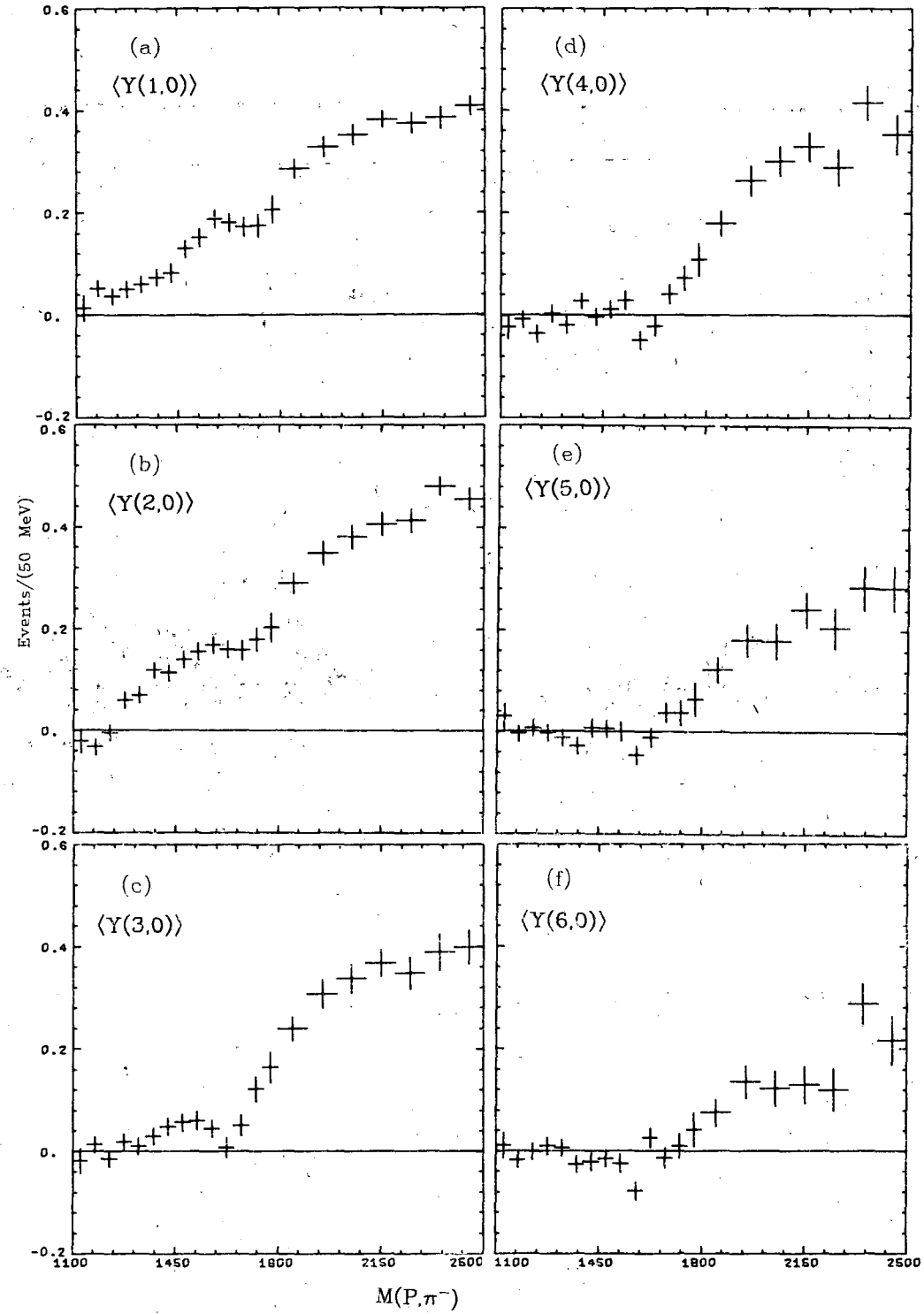

XBL 715-944

Fig. 44

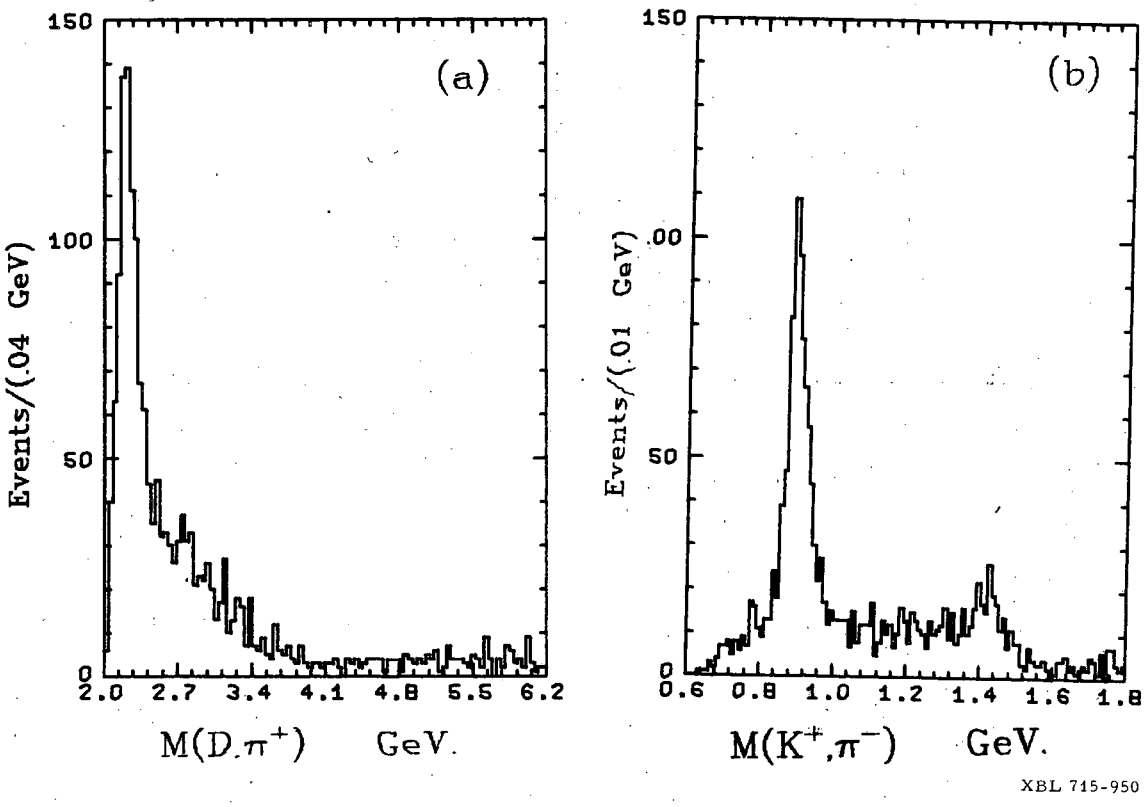
150
100
50
0
Events/(.04 GeV)
(a)
2.0 2.7 3.4 4.1 4.8 5.5 6.2
M(D.π+) GeV.
150
100
50
0
Events/(.01 GeV)
(b)
0.6 0.8 1.0 1.2 1.4 1.6 1.8
M(K+,π−) GeV.
XBL 715-950

Fig. 45

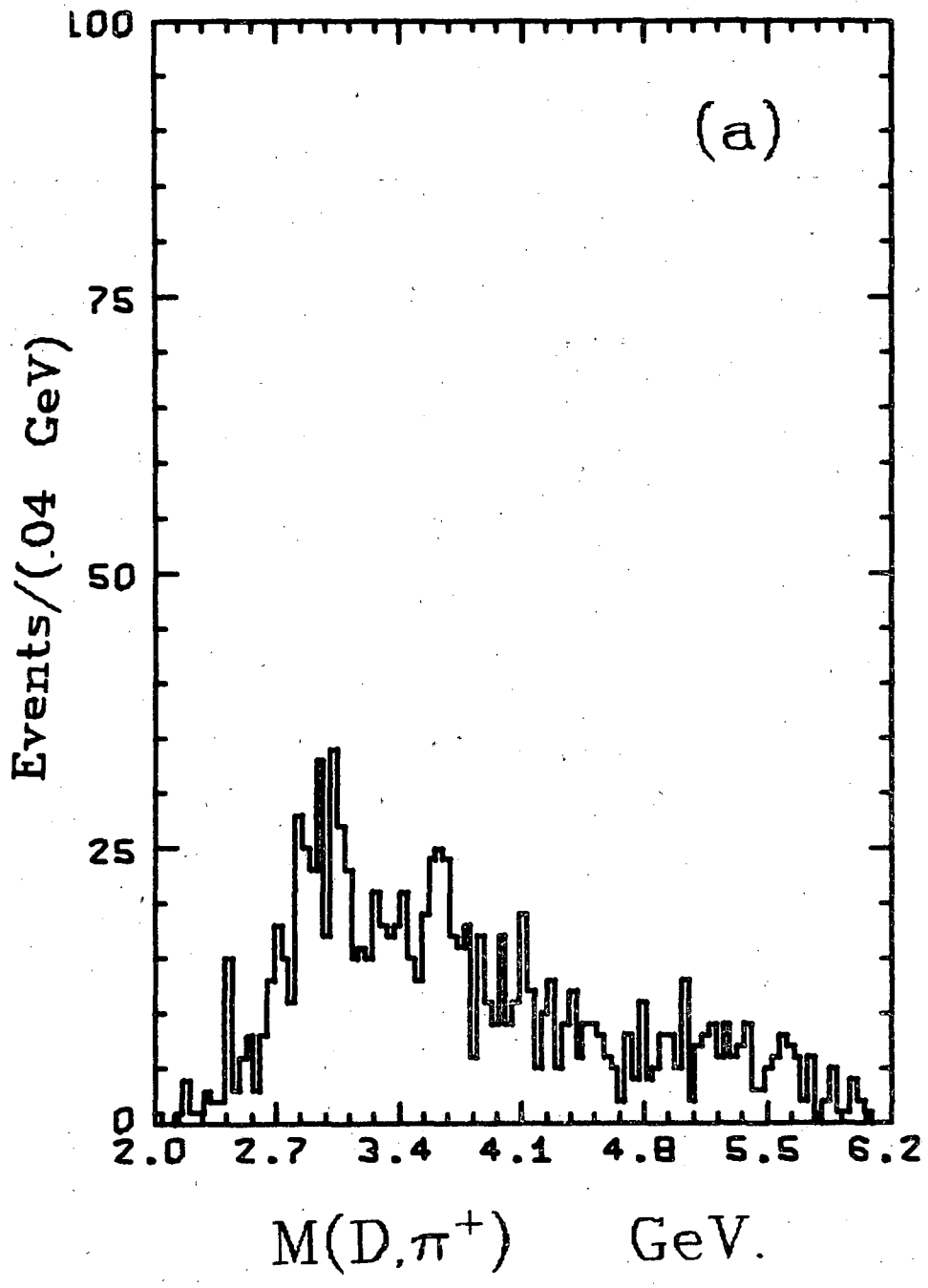

XBL 715-948

Fig. 46

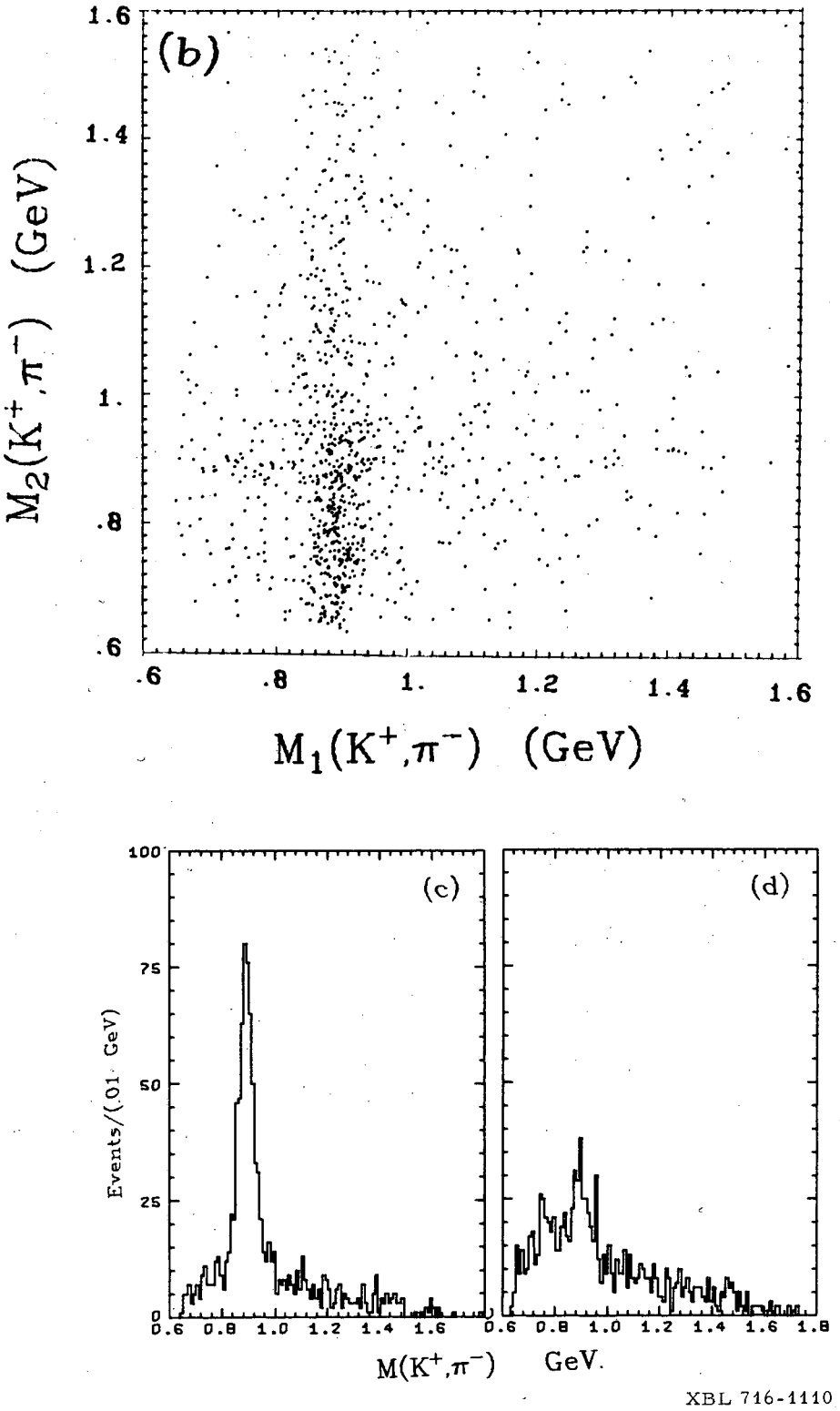
(b)
$M_2(K^+,\pi^-)$ (GeV)
$M_1(K^+,\pi^-)$ (GeV)
1.6
1.4
1.2
1.
.8
.6
.6
.8
1.
1.2
1.4
1.6
(c)
(d)
Events/(.01 GeV)
100
75
50
25
0
0.6 0.8 1.0 1.2 1.4 1.6
0.6 0.8 1.0 1.2 1.4 1.6 1.8
$M(K^+,\pi^-)$ GeV.
XBL 716-1110

Fig. 46

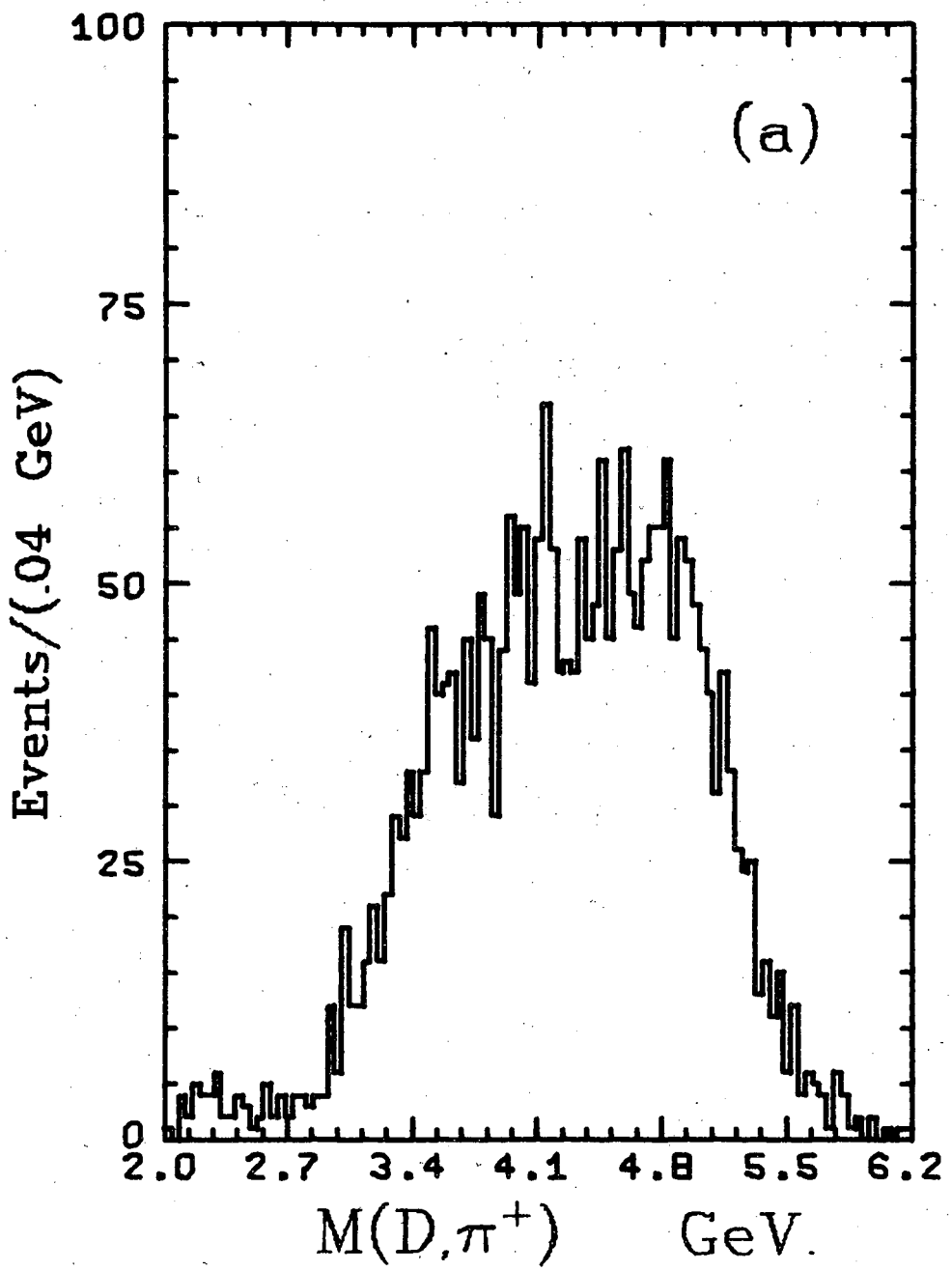

XBL 715-947

Fig. 47

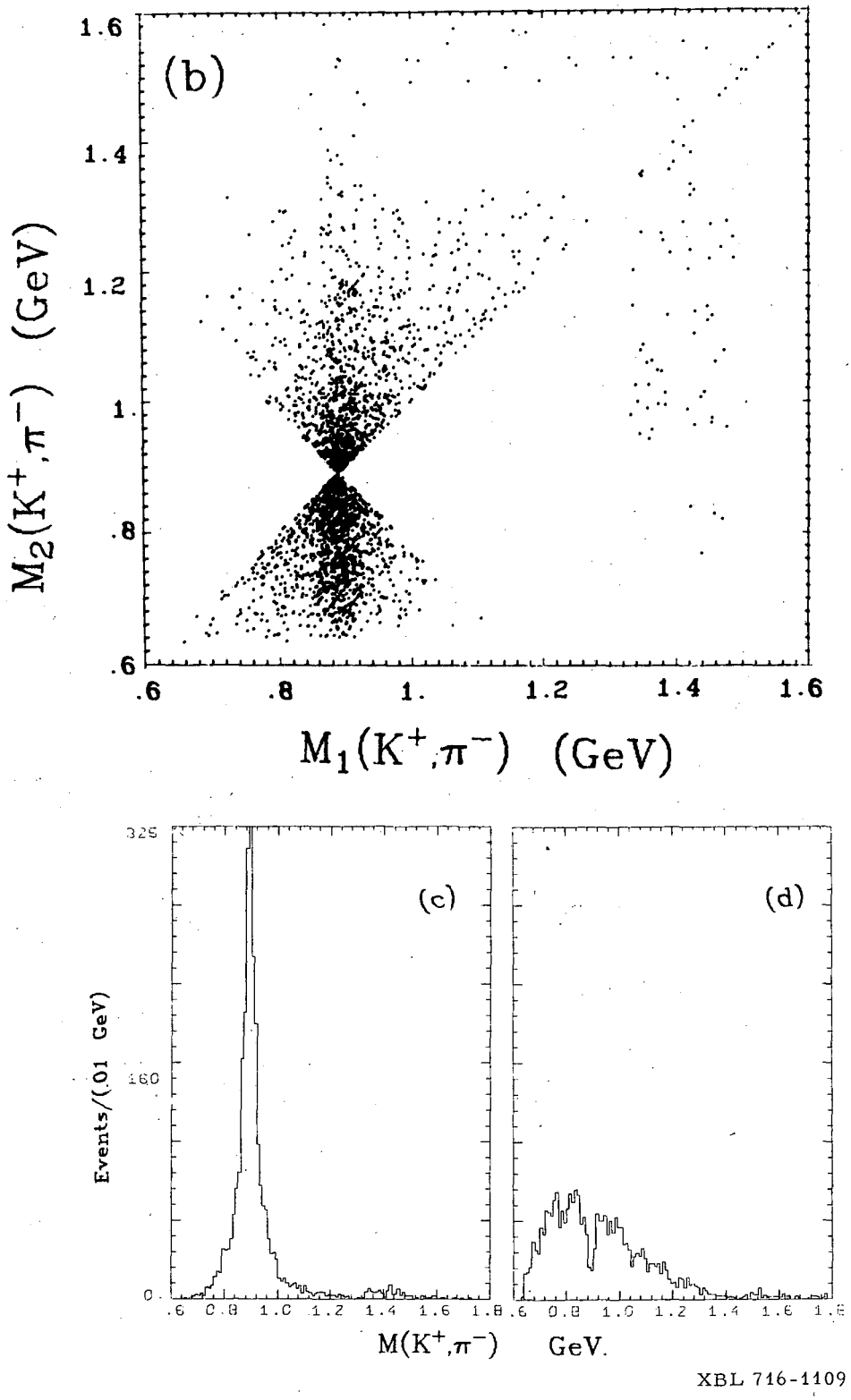
(b)
1.6
1.4
1.2
1.
.8
.6
$M_2(K^+,\pi^-)$ (GeV)
.6
.8
1.
1.2
1.4
1.6
$M_1(K^+,\pi^-)$ (GeV)
(c)
(d)
325
160
0
Events/(.01 GeV)
.6 0.8 1.0 1.2 1.4 1.6 1.8
.6 0.8 1.0 1.2 1.4 1.6 1.8
$M(K^+,\pi^-)$ GeV.
XBL 716-1109

Fig. 47

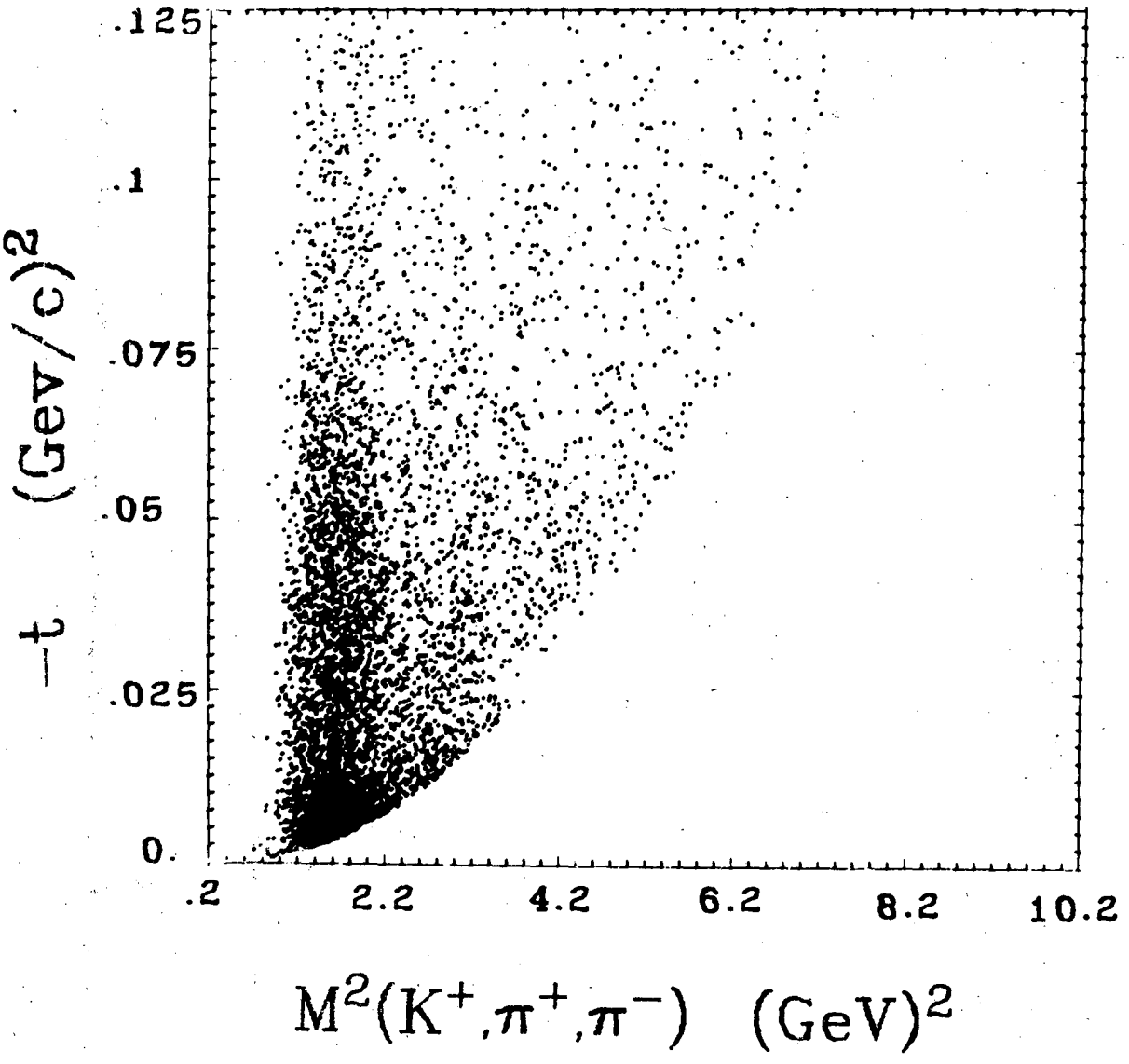

XBL 716-1113

Fig. 48

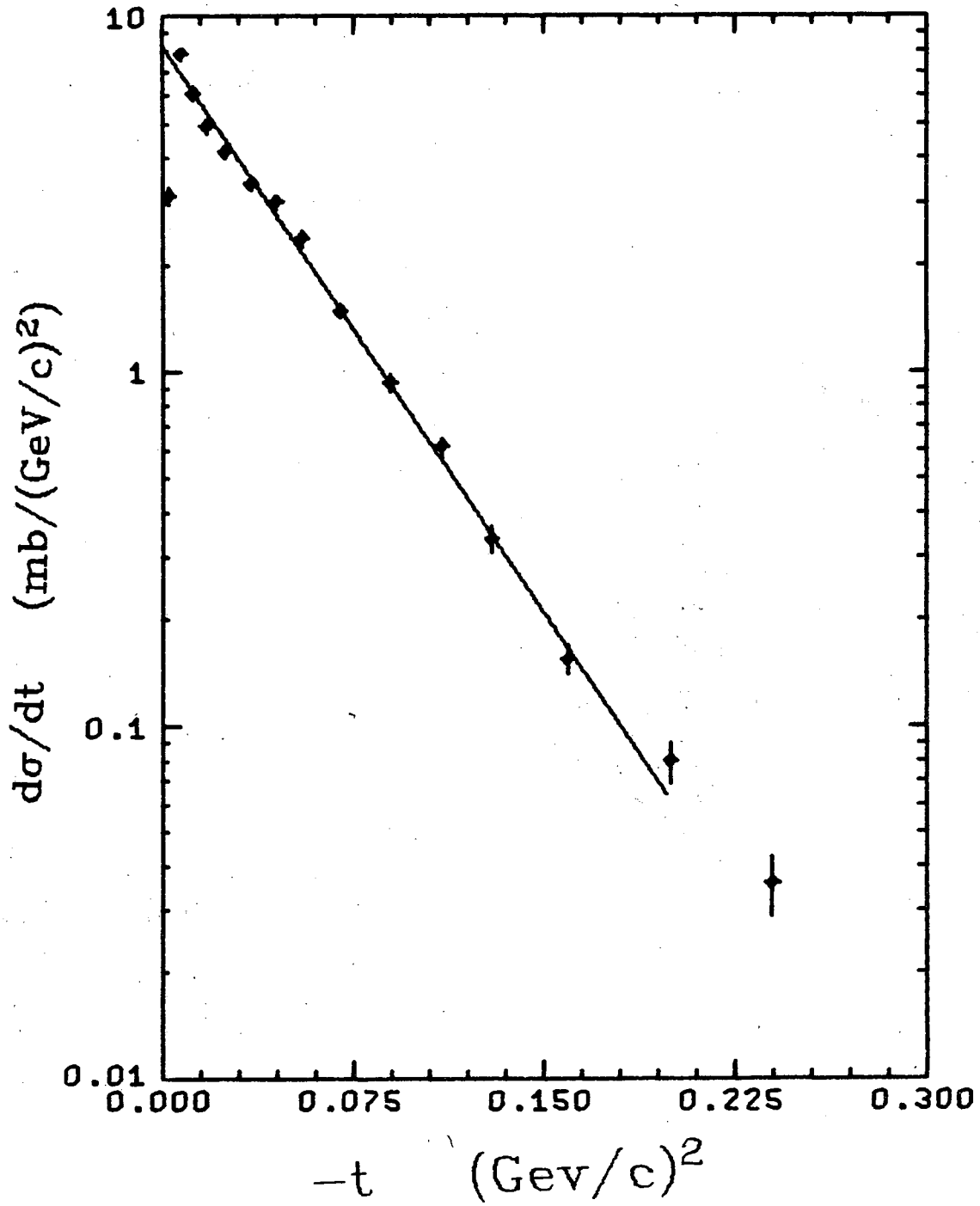

XBL 716-1037

Fig. 49

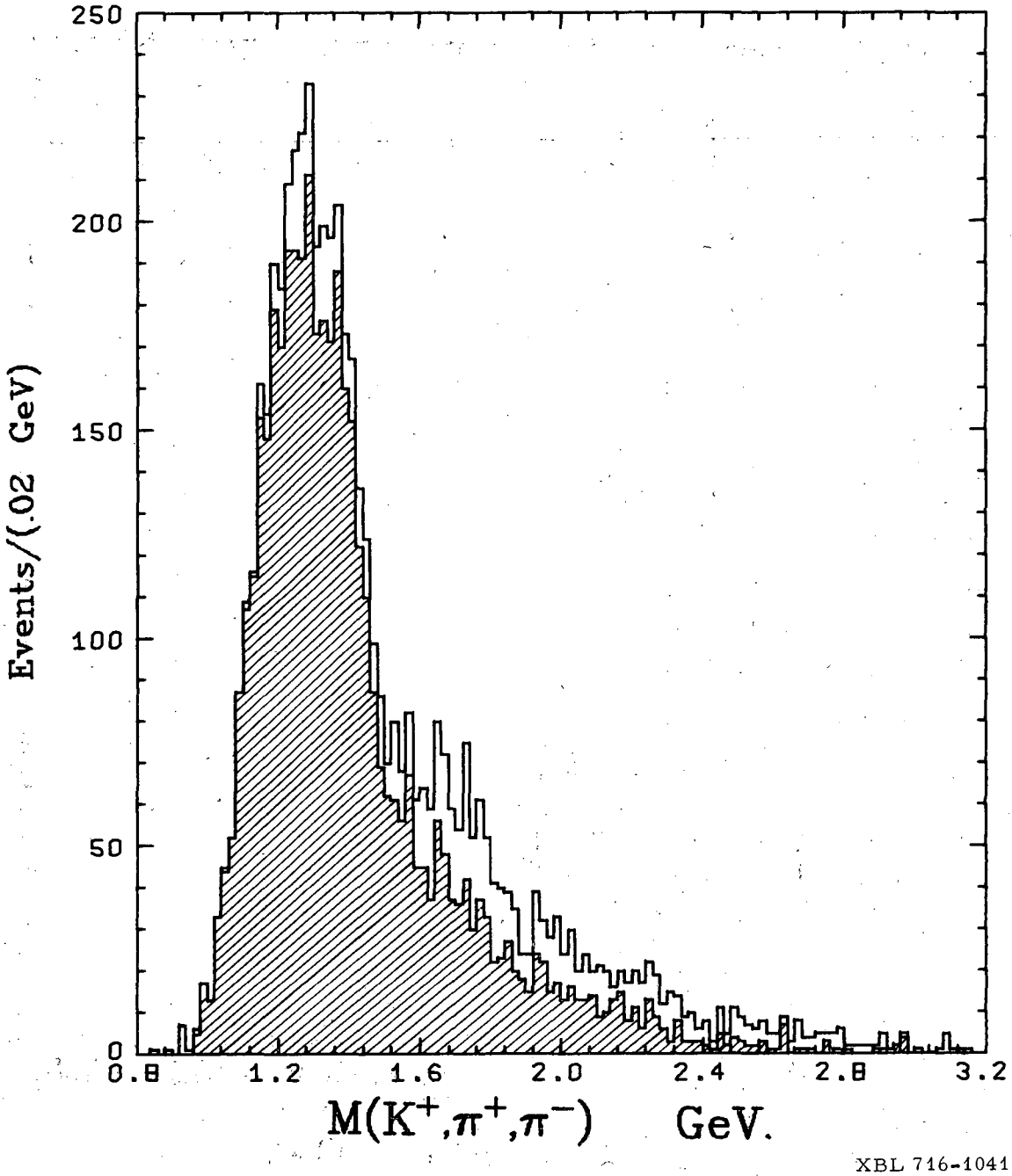
250
200
150
100
50
0
Events/(.02 GeV)
0.8
1.2
1.6
2.0
2.4
2.8
3.2
M(K+,π+,π−) GeV.
XBL 716-1041

Fig. 50

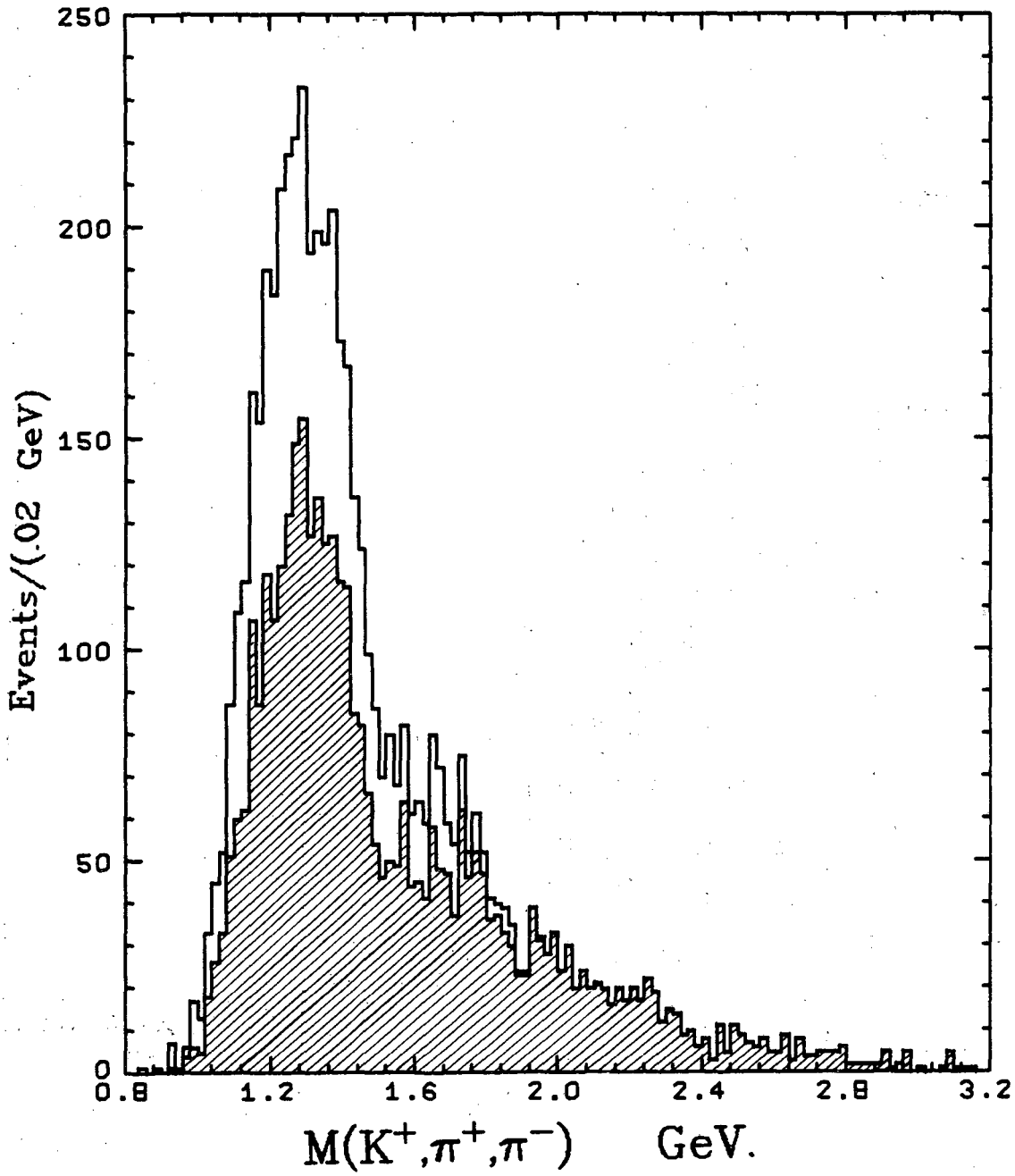
250
200
150
100
50
0
Events/(.02 GeV)
0.8
1.2
1.6
2.0
2.4
2.8
3.2
M(K+,π+,π−) GeV.
XBL 716-1038

Fig. 51

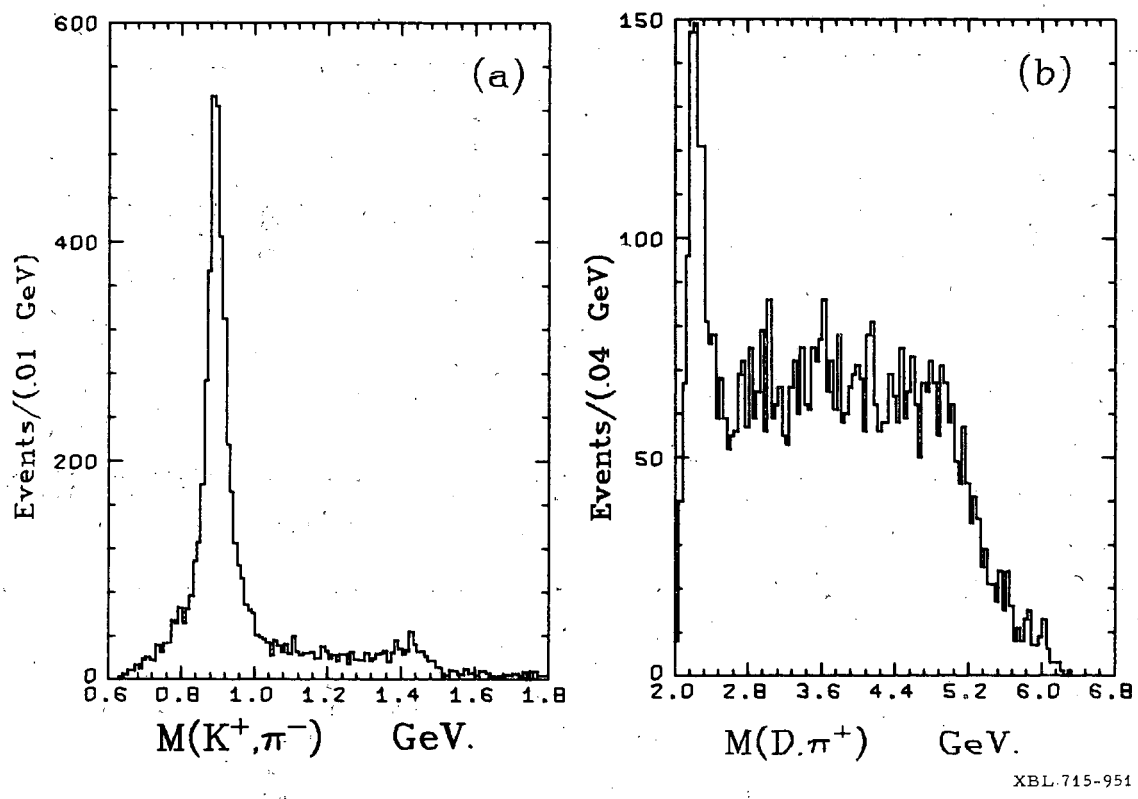
(a)
Events/(.01 GeV)
600
400
200
0
0.6 0.8 1.0 1.2 1.4 1.6 1.8
M(K⁺,π⁻) GeV.
(b)
Events/(.04 GeV)
150
100
50
0
2.0 2.8 3.6 4.4 5.2 6.0 6.8
M(D.π⁺) GeV.
XBL 715-951

Fig. 52

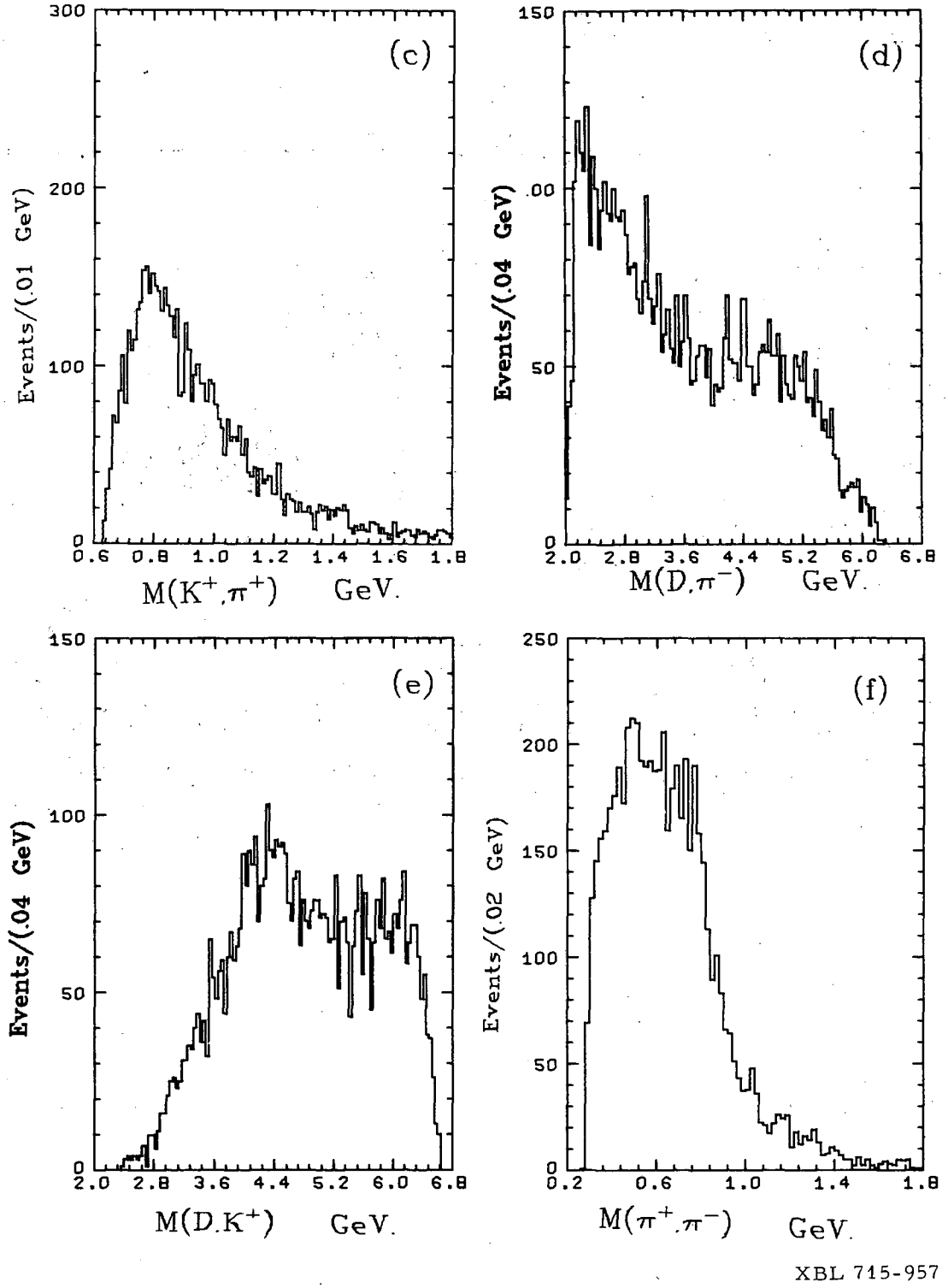
(c)
Events/(.01 GeV)
M(K⁺,π⁺) GeV.
(d)
Events/(.04 GeV)
M(D,π⁻) GeV.
(e)
Events/(.04 GeV)
M(D,K⁺) GeV.
(f)
Events/(.02 GeV)
M(π⁺,π⁻) GeV.
XBL 715-957

Fig. 52

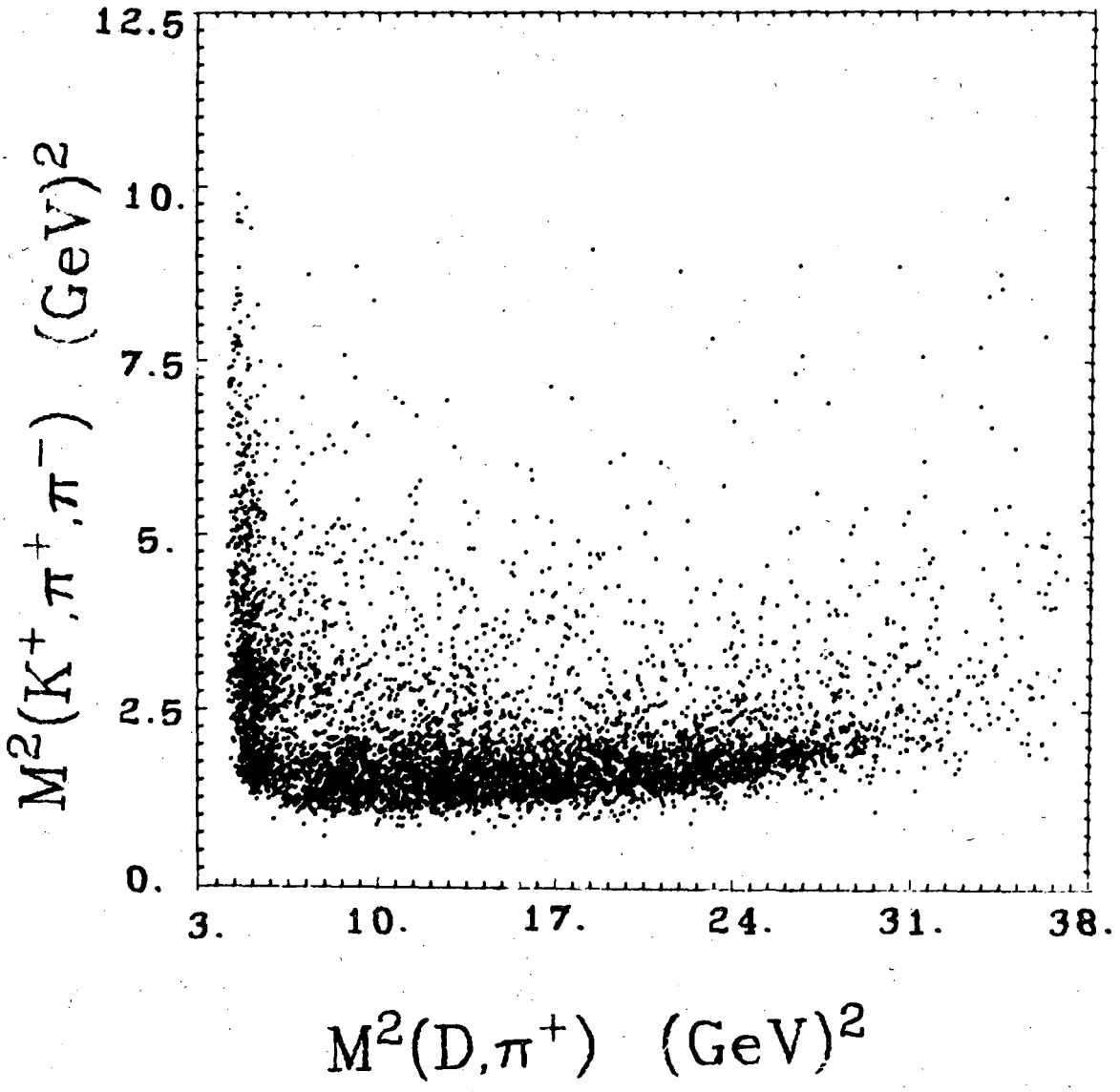

XBL 716-1114

Fig. 53

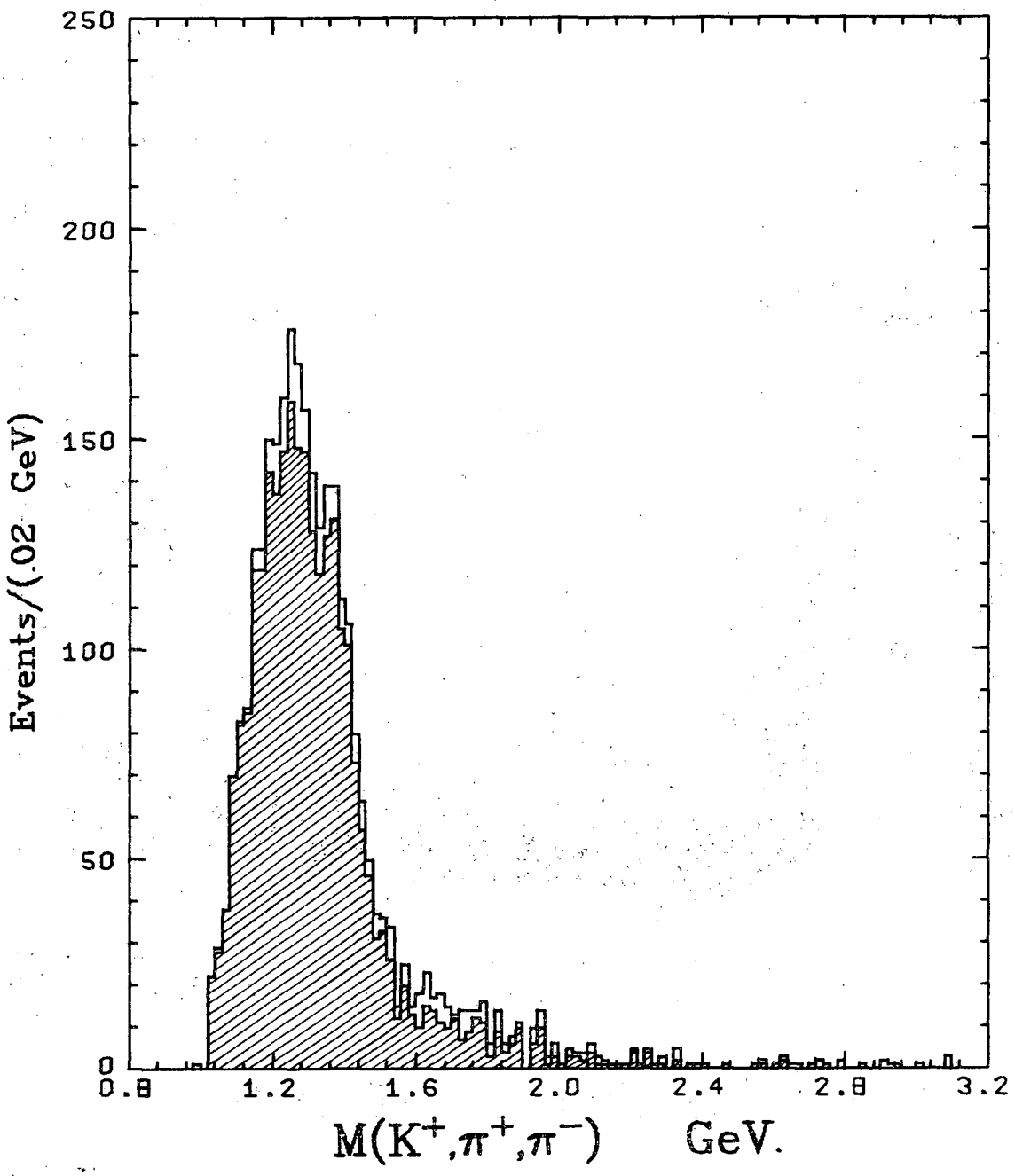
250
200
150
100
50
0
Events/(.02 GeV)
0.8
1.2
1.6
2.0
2.4
2.8
3.2
M(K+,π+,π−) GeV.
XBL 716-1039

Fig. 54

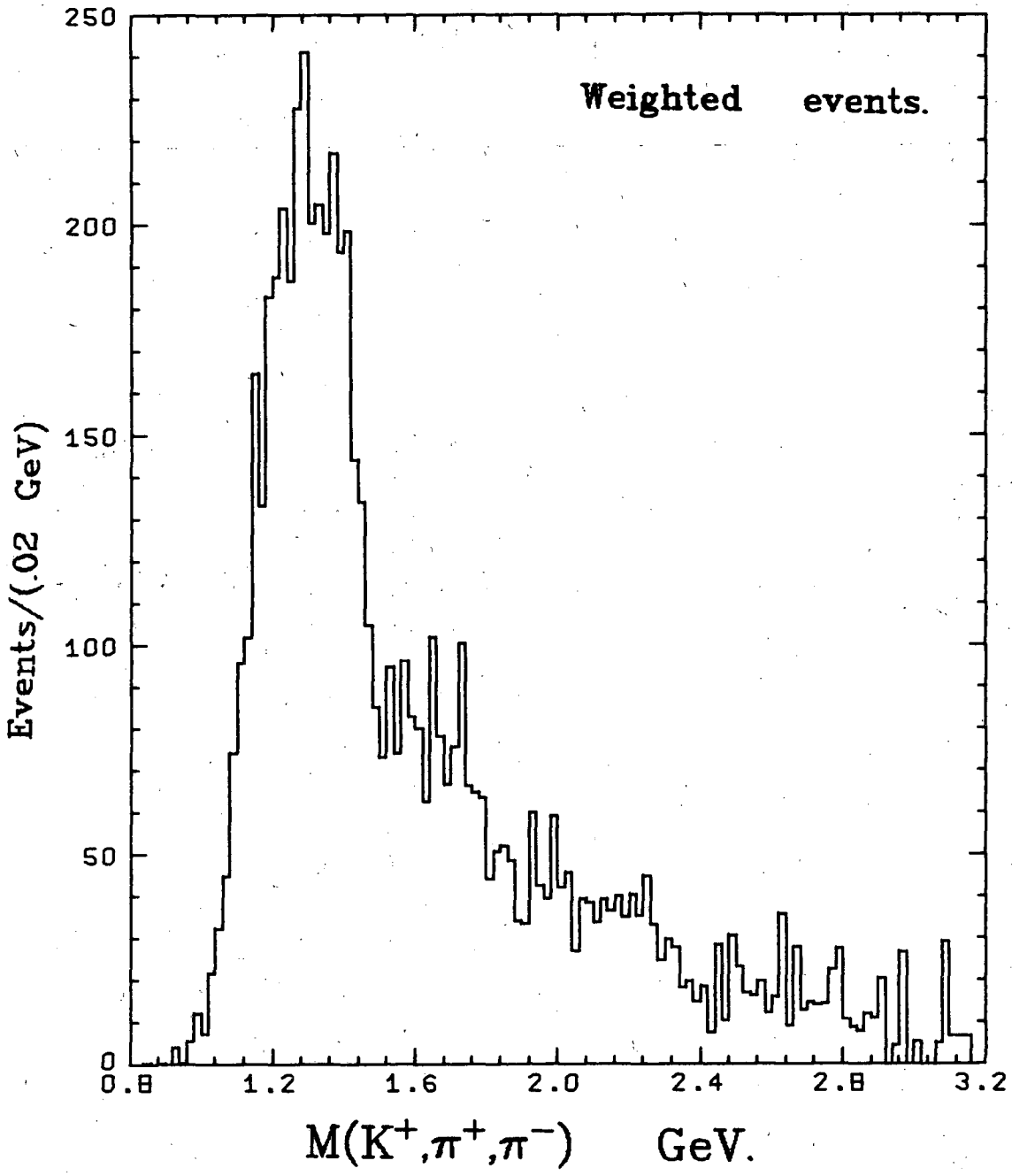
Weighted events.
Events/(.02 GeV)
250
200
150
100
50
0
0.8
1.2
1.6
2.0
2.4
2.8
3.2
M(K+,π+,π−) GeV.
XBL 716-1040

Fig. 55

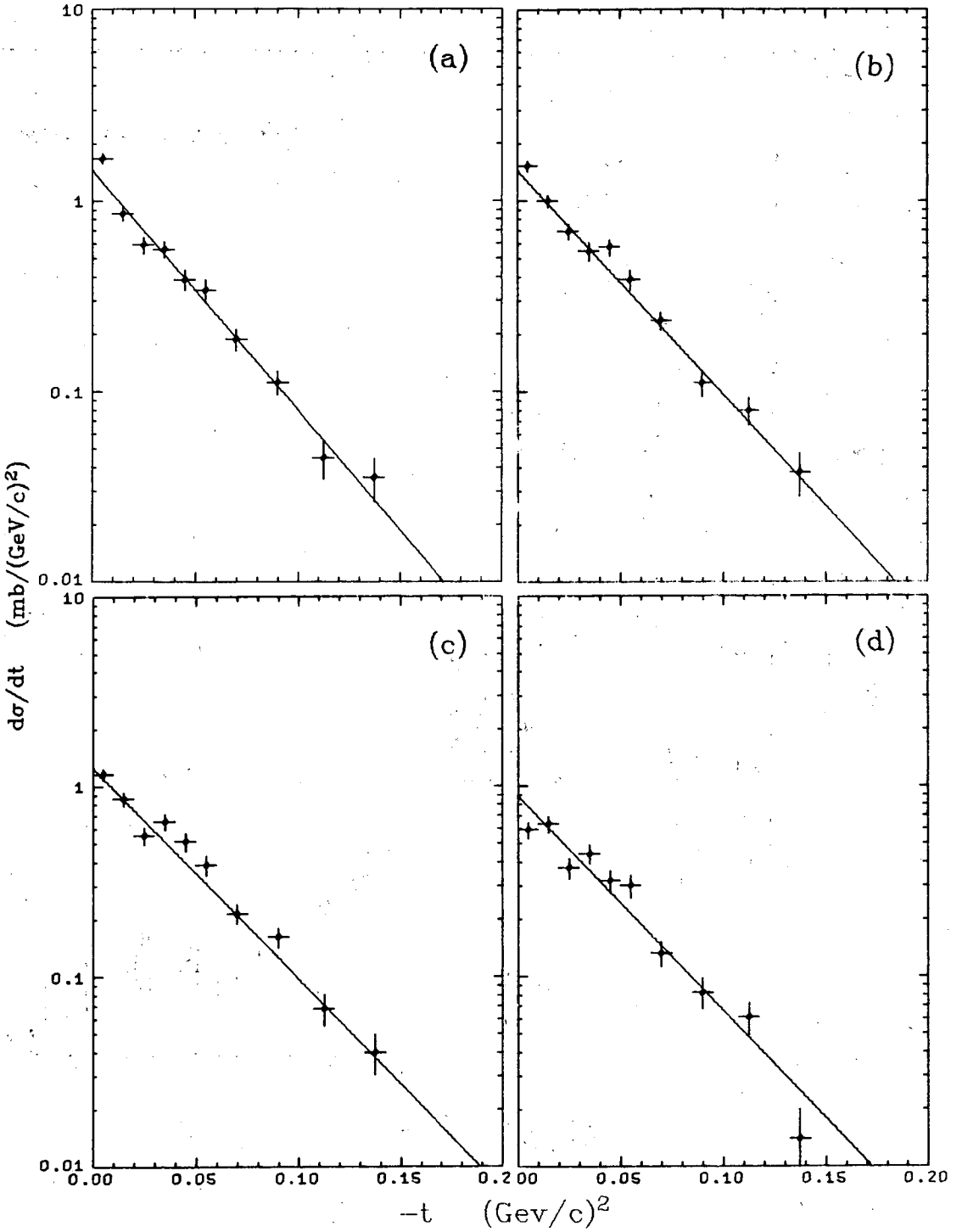
(a)
(b)
(c)
(d)
10
1
0.1
0.01
dσ/dt (mb/(GeV/c)²)
0.00
0.05
0.10
0.15
0.20
−t (Gev/c)²
XBL 716-1044

Fig. 56

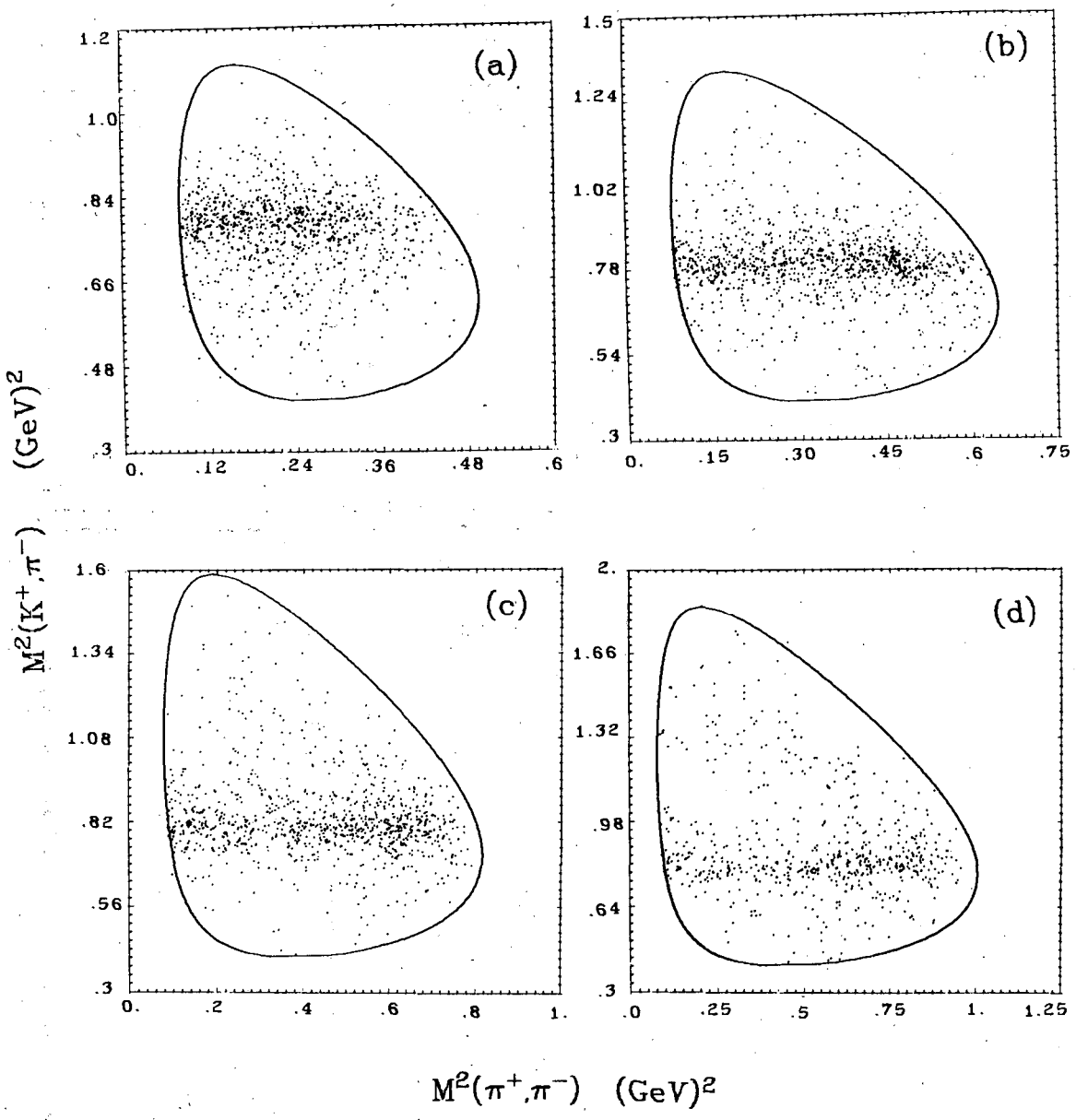

XBL 716-1125

Fig. 57

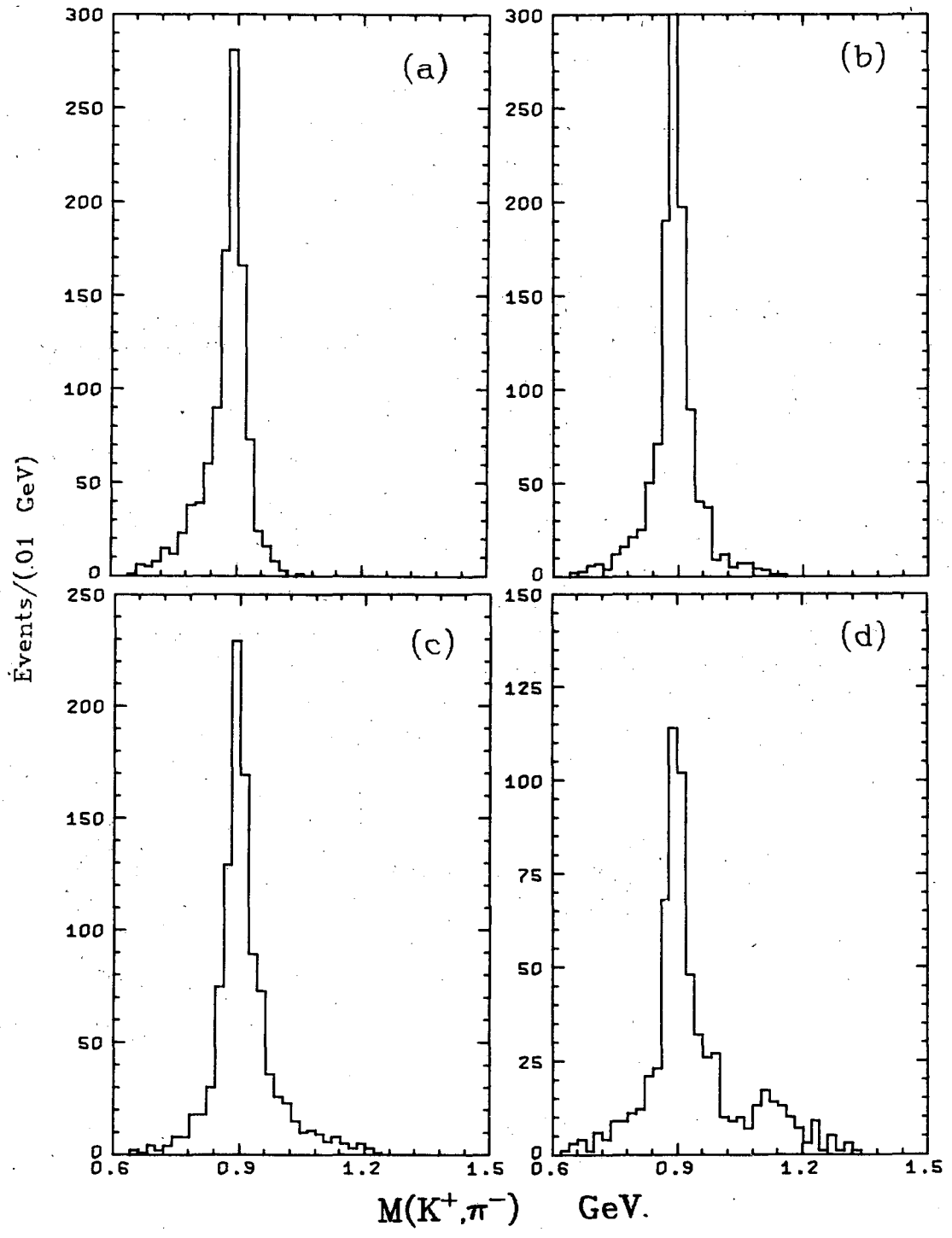

XBL 715-955

Fig. 58

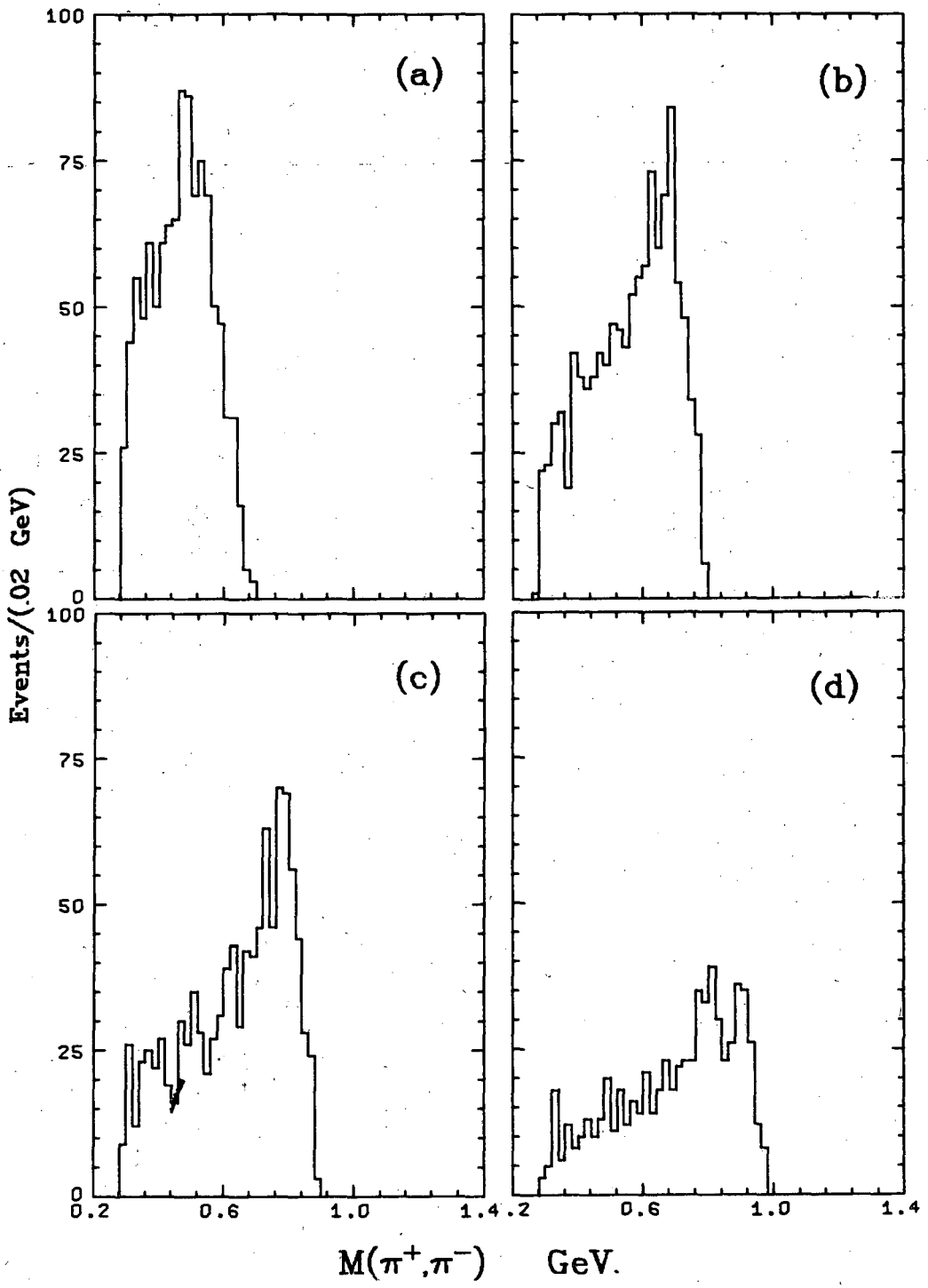

XBL 715-961

Fig. 59

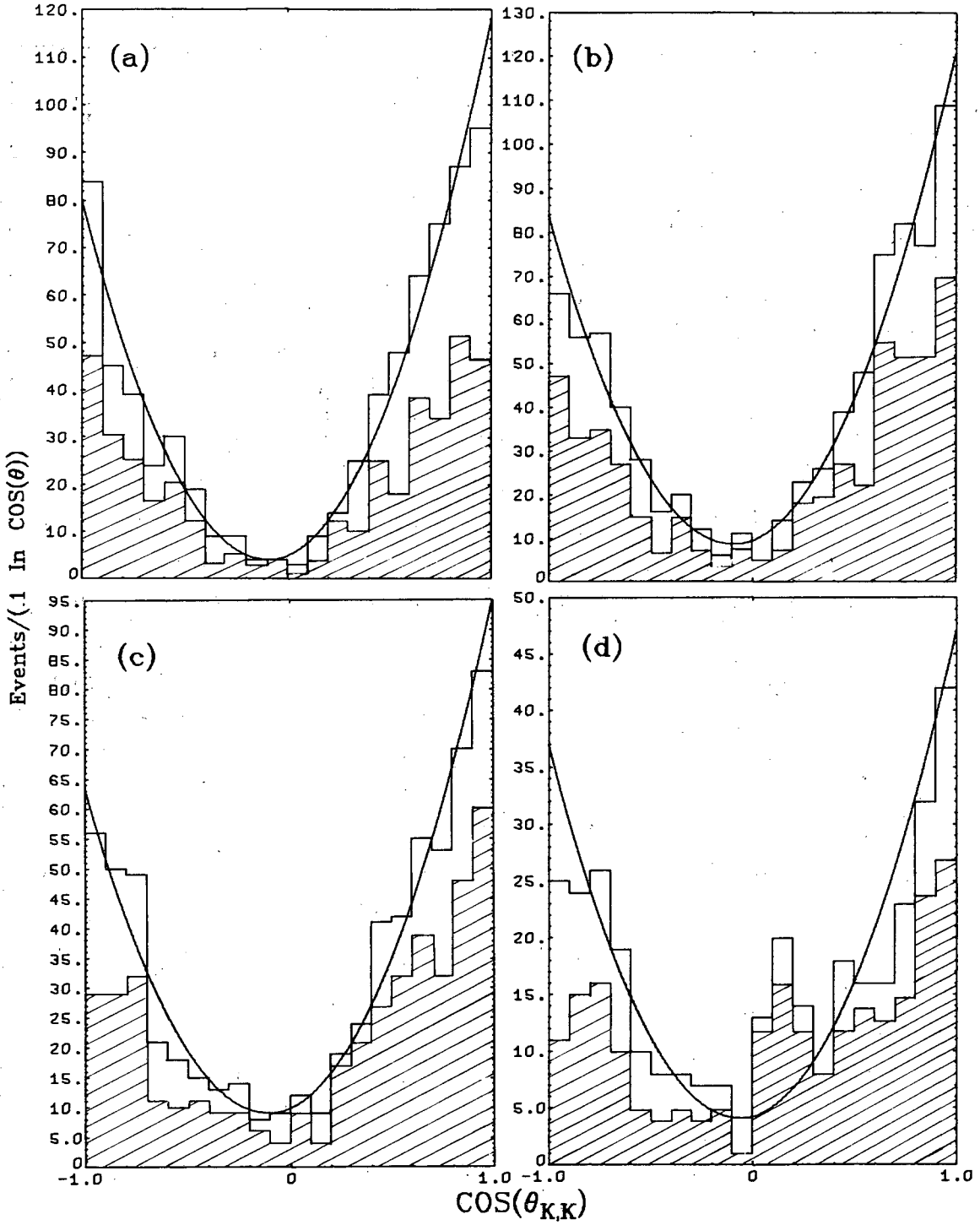

XBL 716-1050

Fig. 60

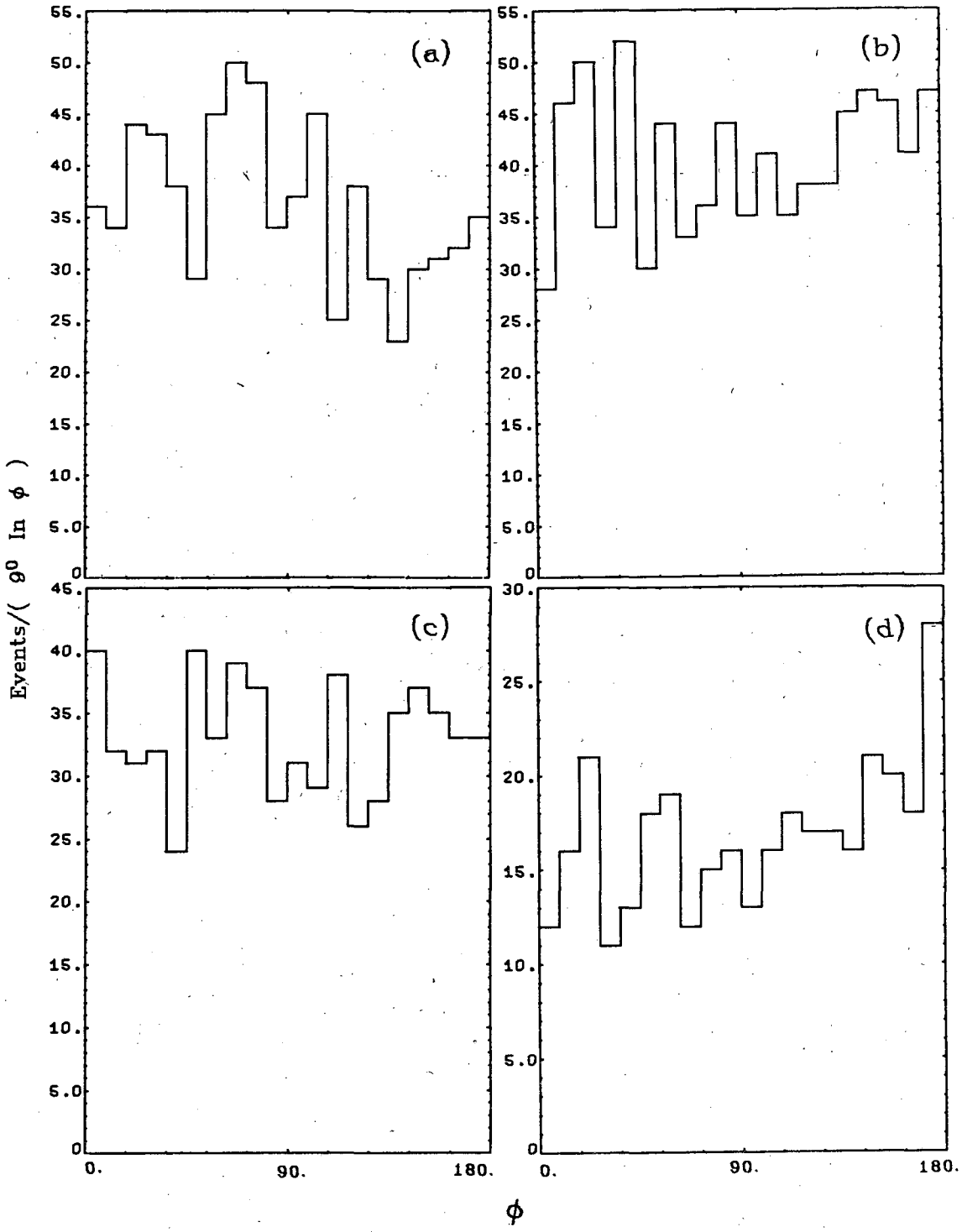

Fig. 61

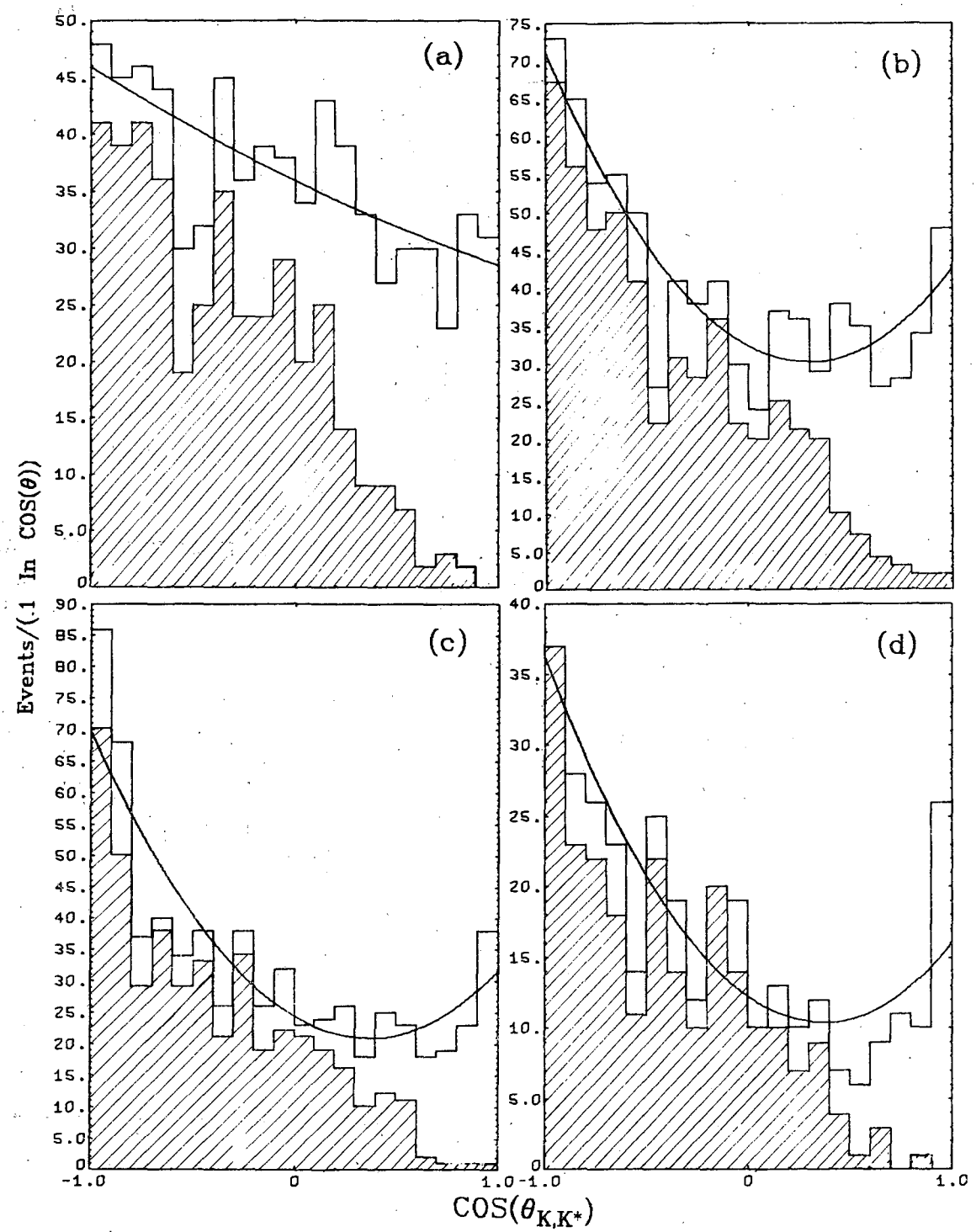

XBL 716-1048

Fig. 62

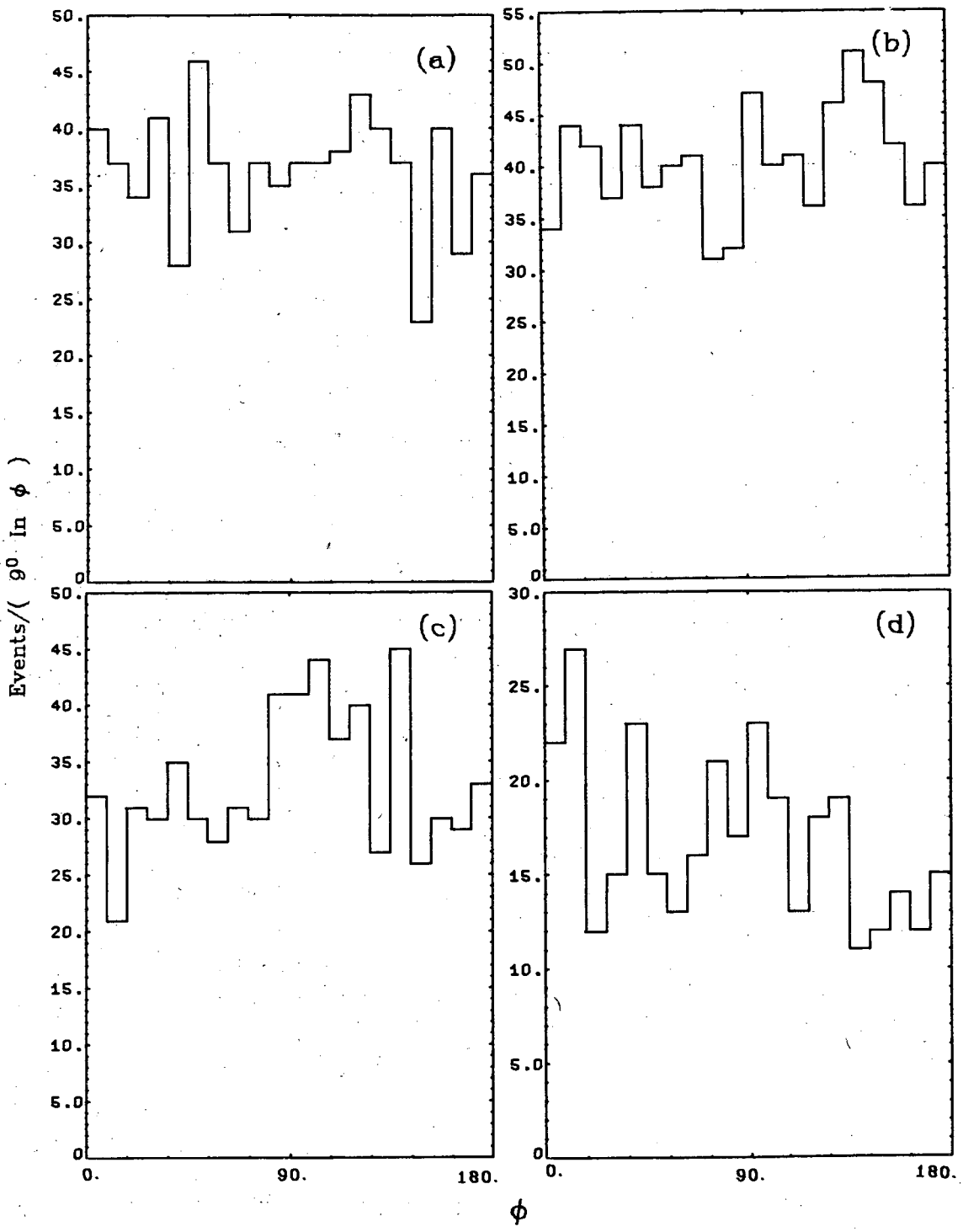

Fig. 63

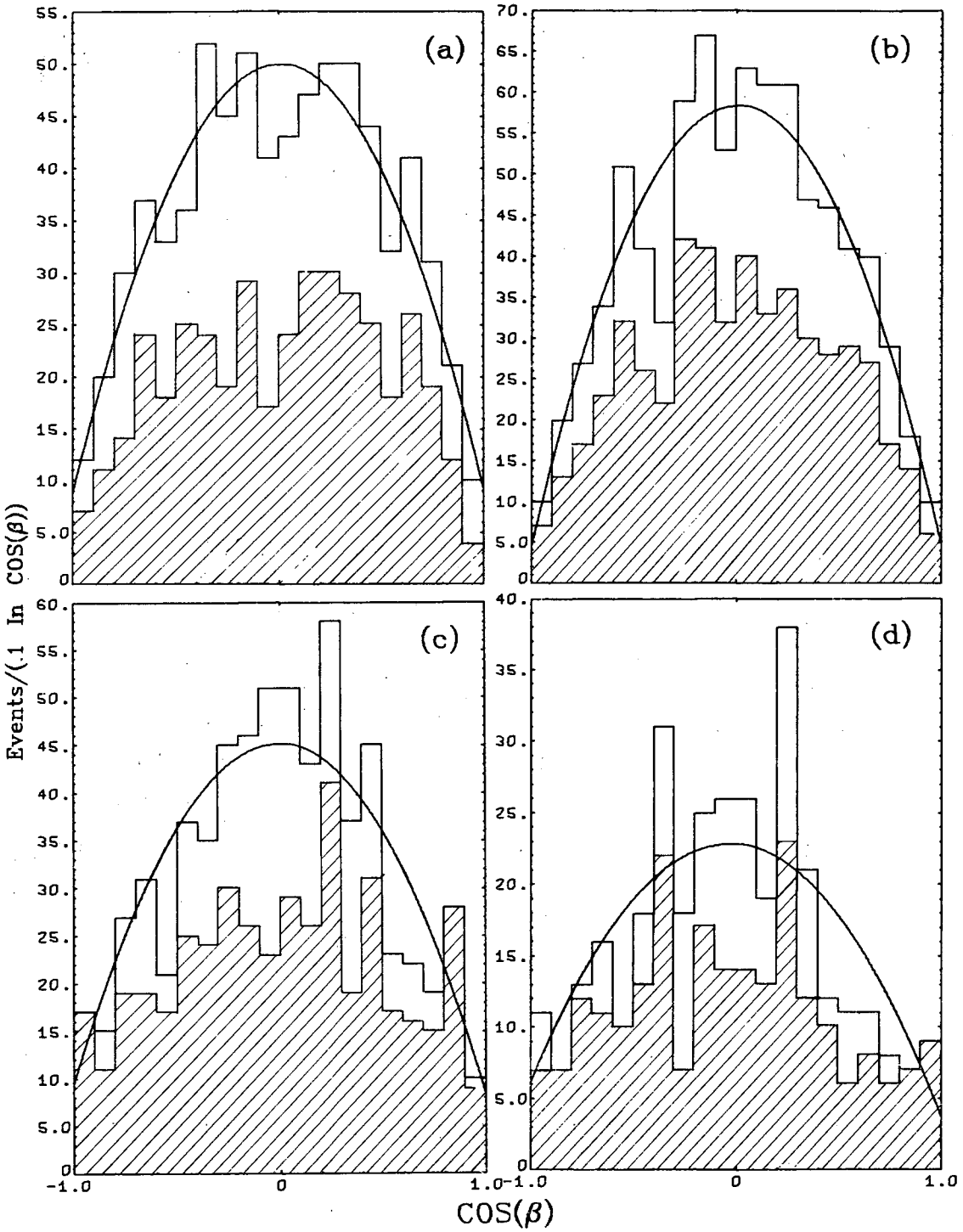

XBL 716-1049

Fig. 64

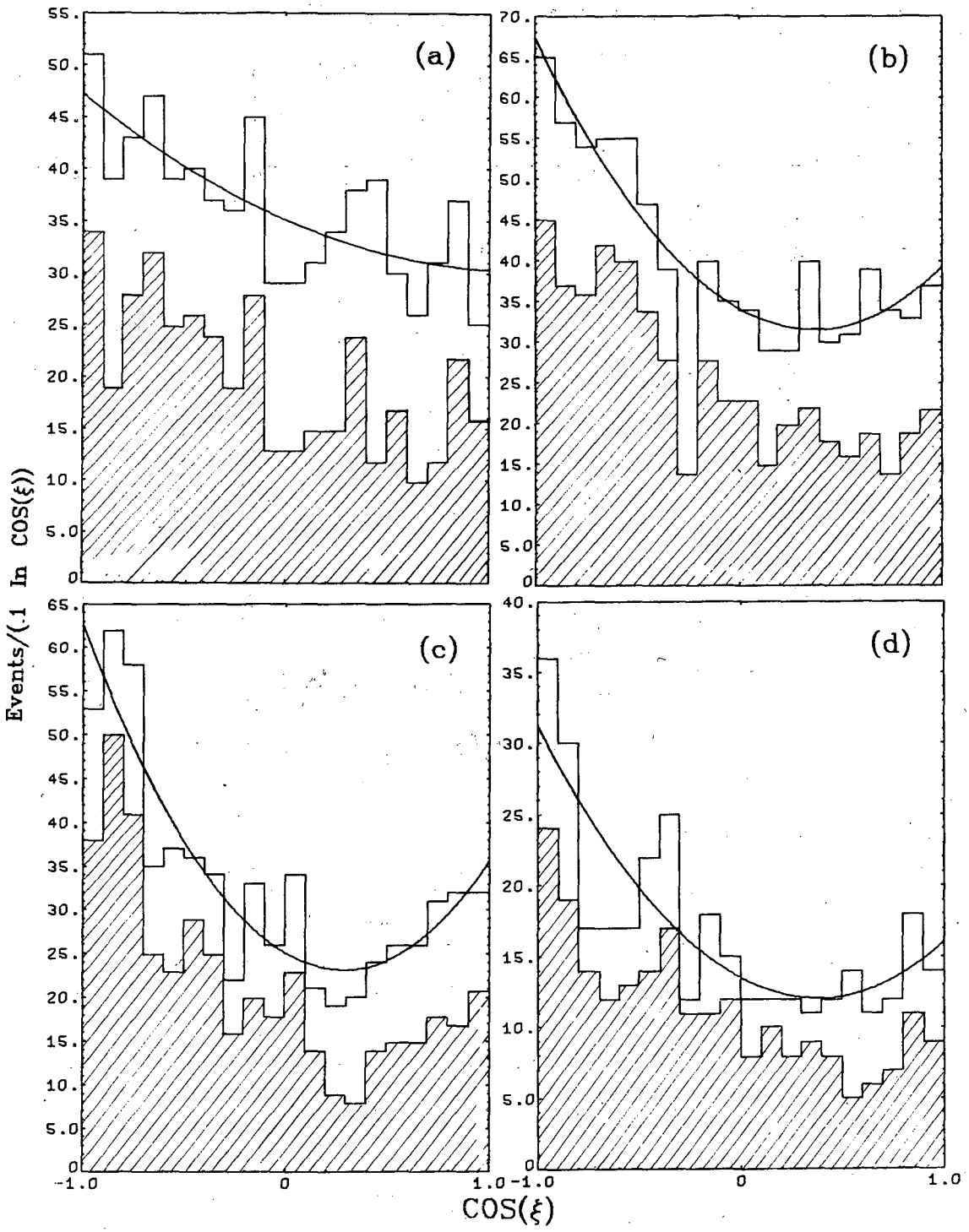

Fig. 65

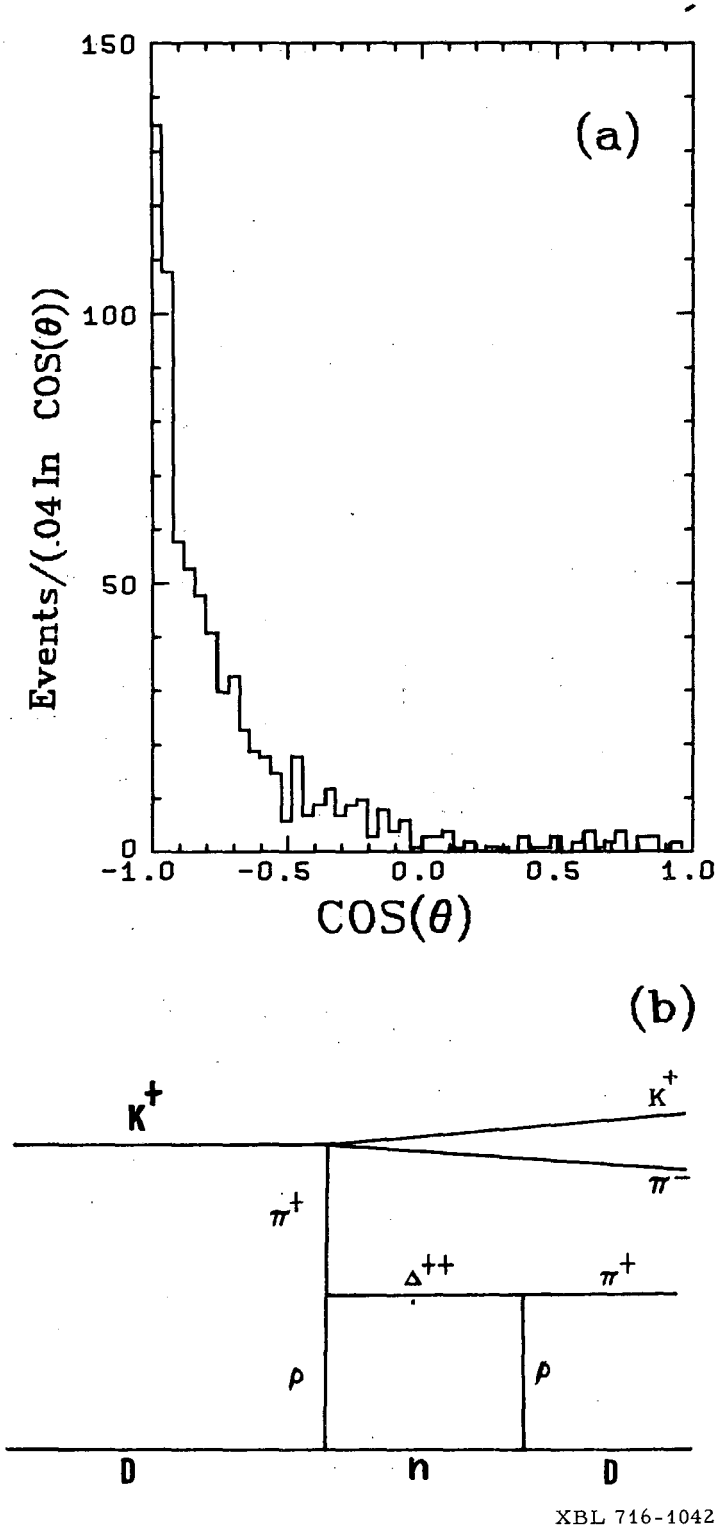
150
100
50
0
(a)
Events/(.04 ln COS(θ))
-1.0
-0.5
0.0
0.5
1.0
COS(θ)
(b)
K+
K+
π−
π+
Δ++
π+
ρ
ρ
D
n
D
XBL 716-1042

Fig. 66

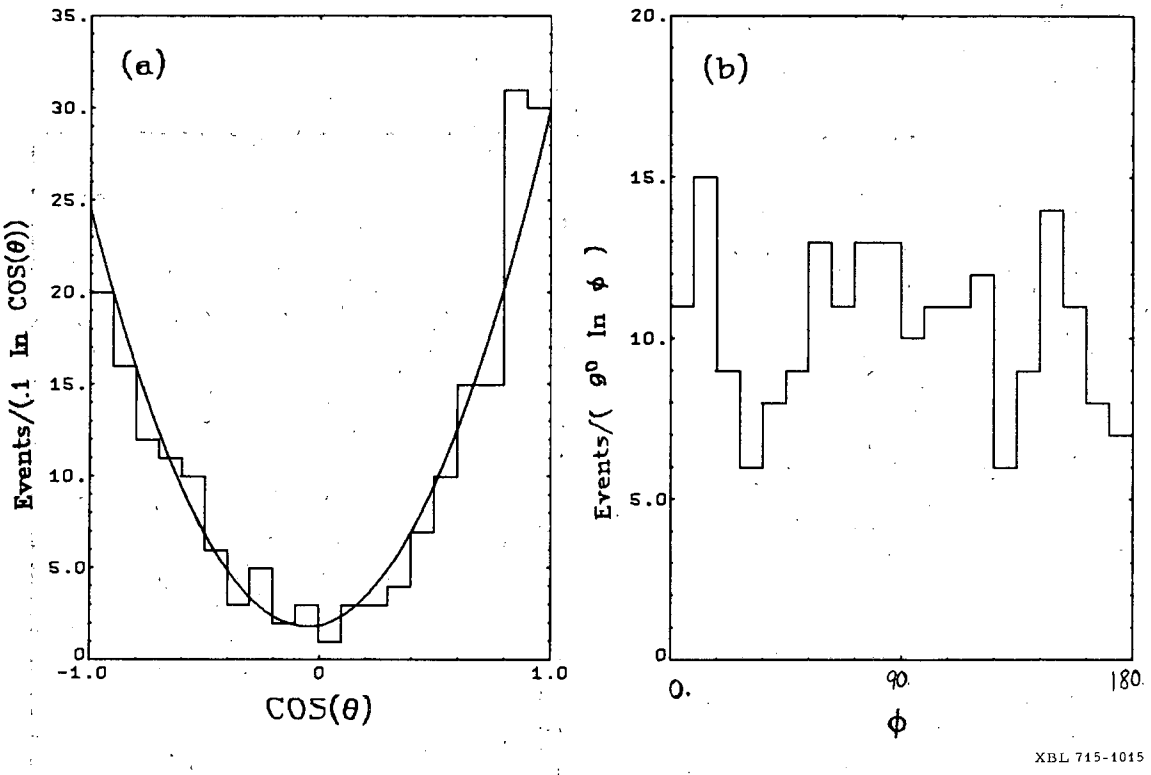
(a)
Events/(.1 ln COS(θ))
COS(θ)
35.
30.
25.
20.
15.
10.
5.0
0
-1.0
0
1.0
(b)
Events/(9° ln φ)
φ
20.
15.
10.
5.0
0
0.
90.
180.
XBL 715-1015

Fig. 67

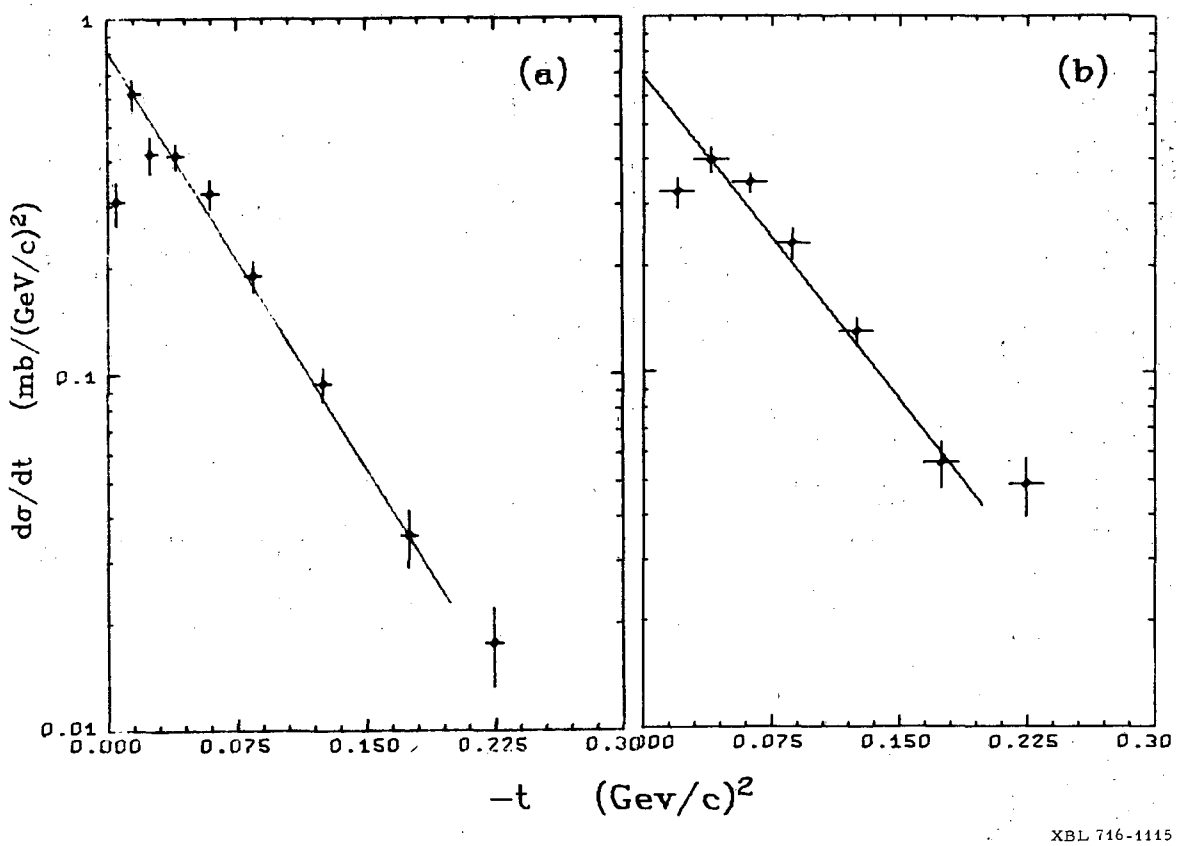
(a)
(b)
1
0.1
0.01
dσ/dt (mb/(GeV/c)²)
0.000
0.075
0.150
0.225
0.30
−t (Gev/c)²
XBL 716-1115

Fig. 68

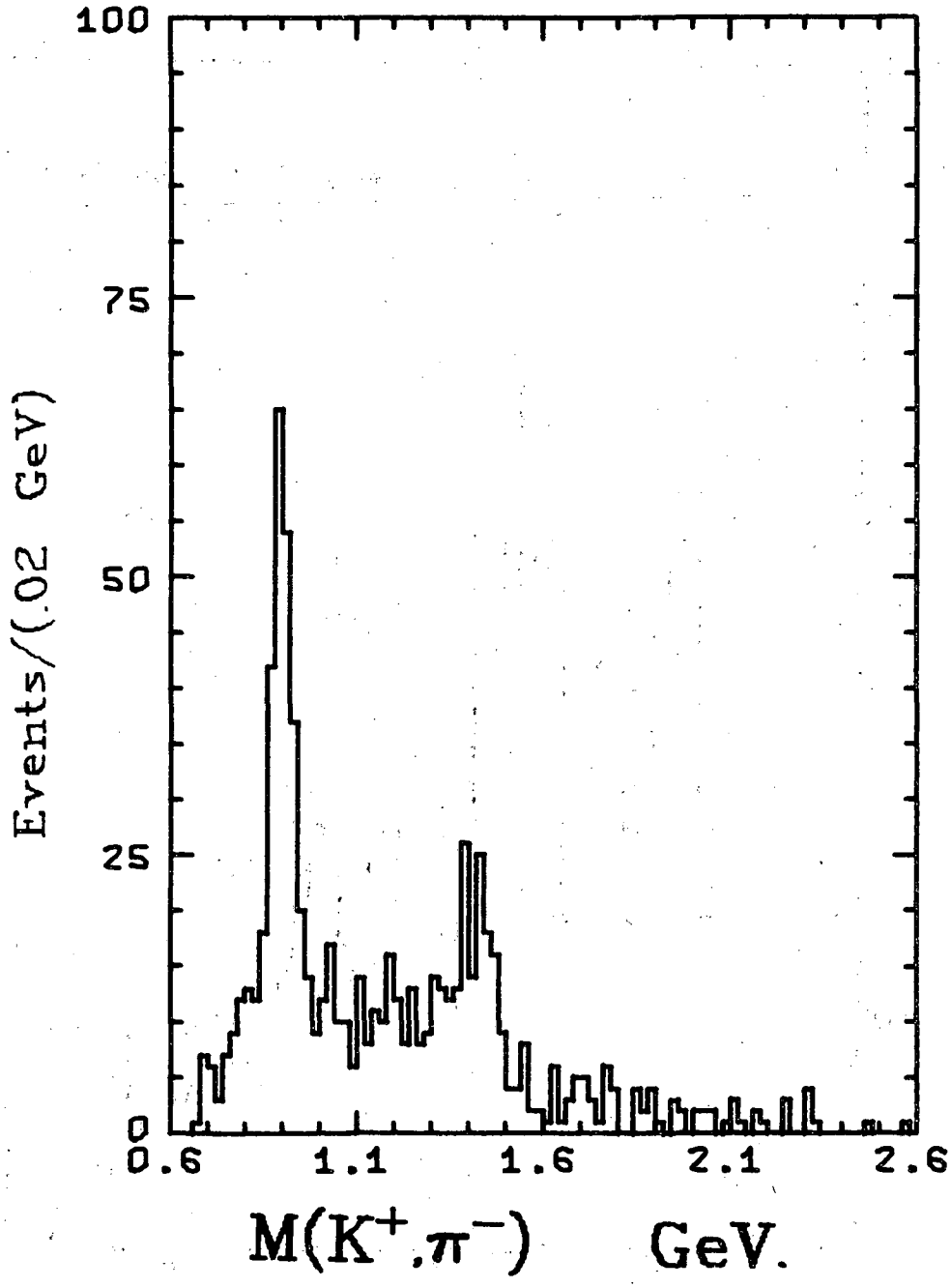

XBL 715-952

Fig. 69

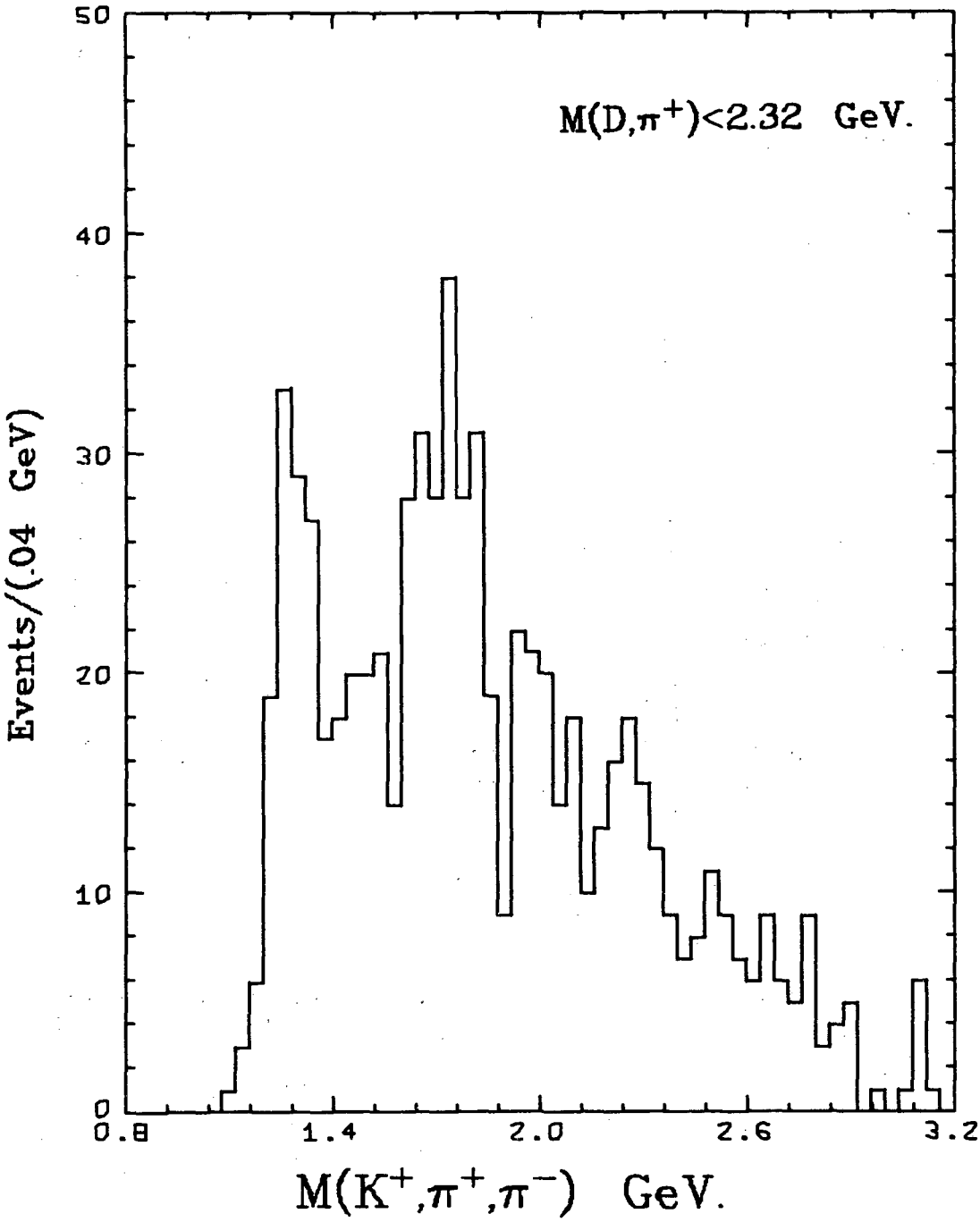

XBL 716-1111

Fig. 70

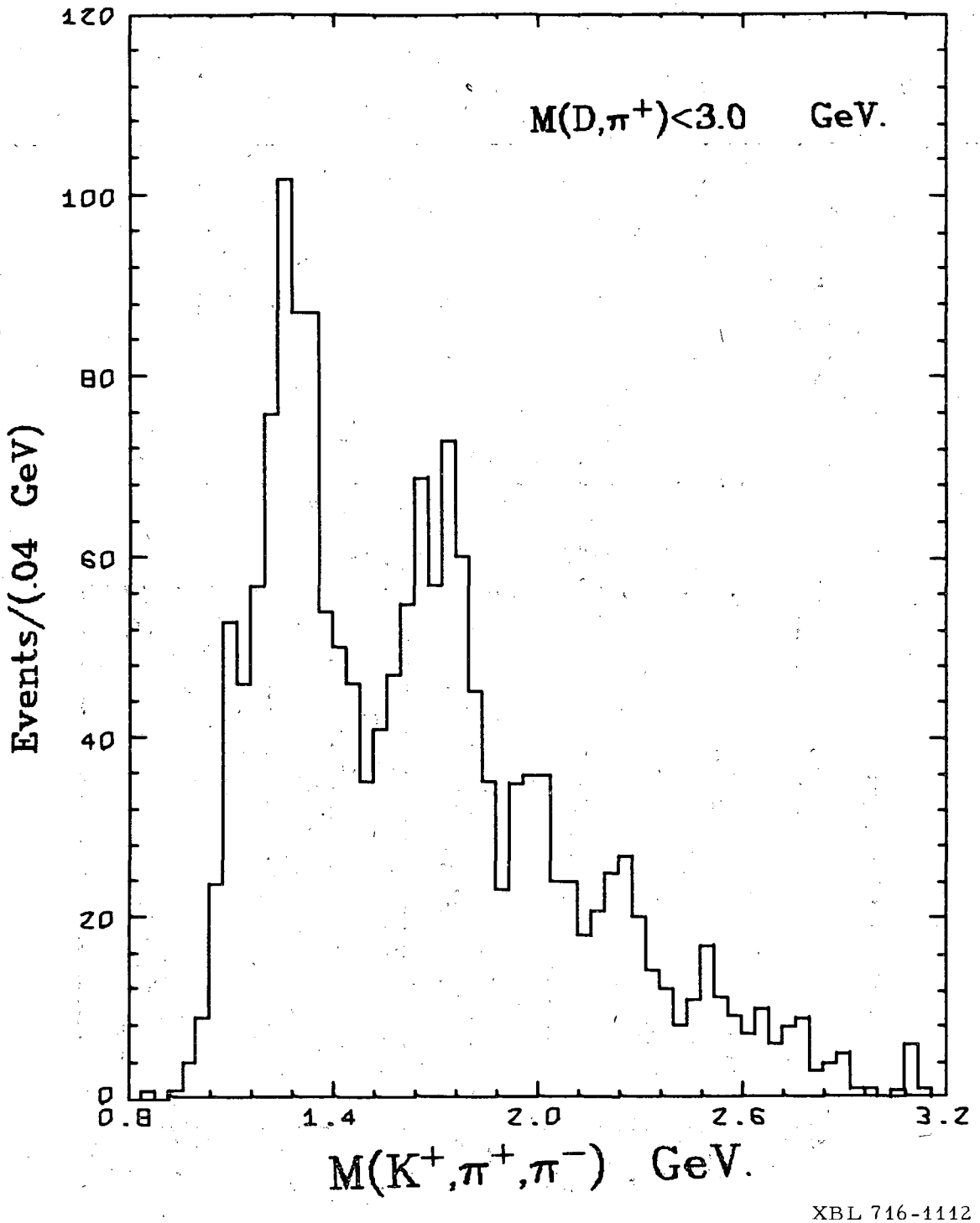

XBL 716-1112

Fig. 71

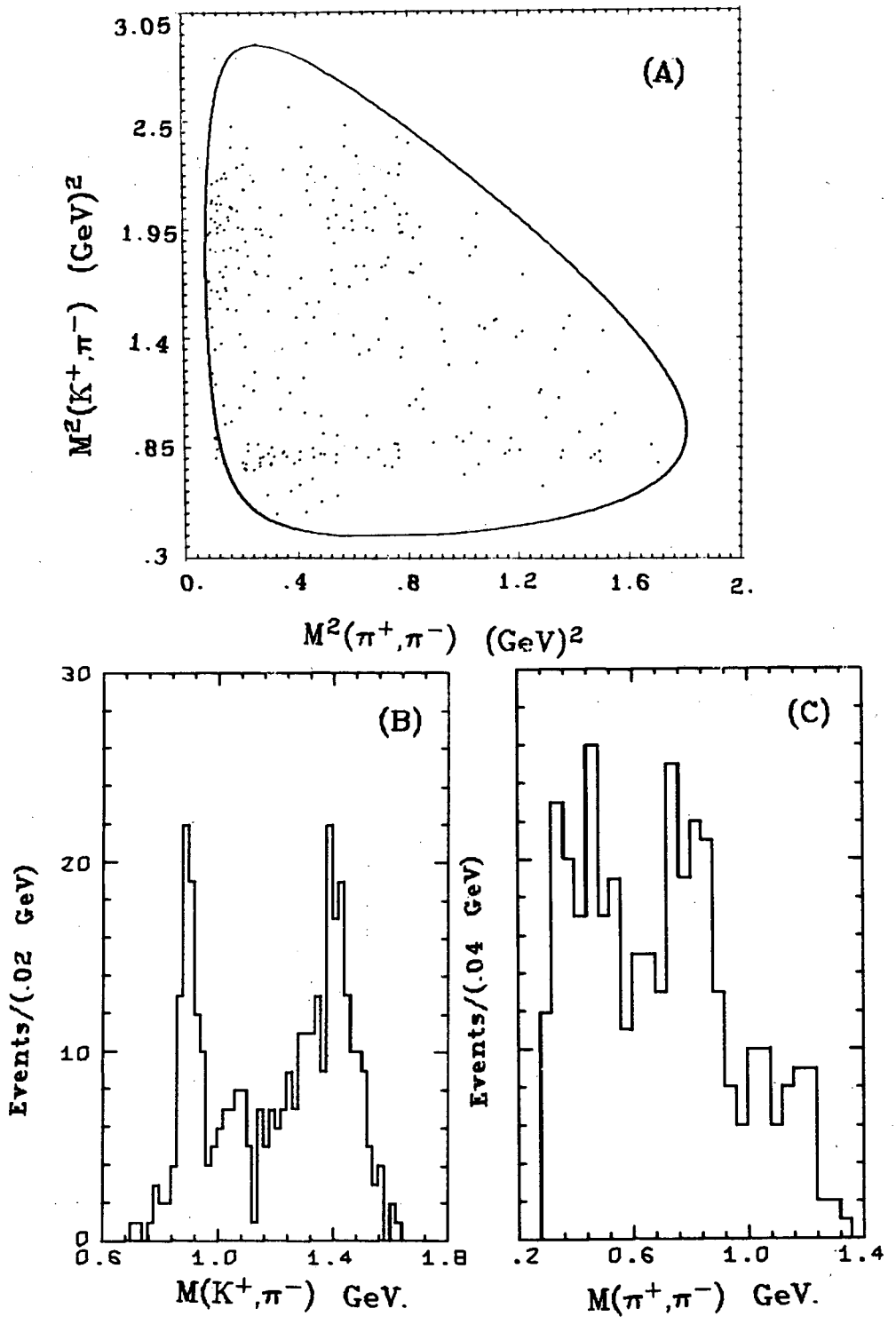
(A)
3.05
2.5
1.95
1.4
.85
.3
0.
.4
.8
1.2
1.6
2.
$M^2(K^+,\pi^-)$ $(GeV)^2$
$M^2(\pi^+,\pi^-)$ $(GeV)^2$
(B)
30
20
10
0
0.6
1.0
1.4
1.8
Events/(.02 GeV)
$M(K^+,\pi^-)$ GeV.
(C)
.2
0.6
1.0
1.4
Events/(.04 GeV)
$M(\pi^+,\pi^-)$ GeV.
XBL 716-1123

Fig. 72

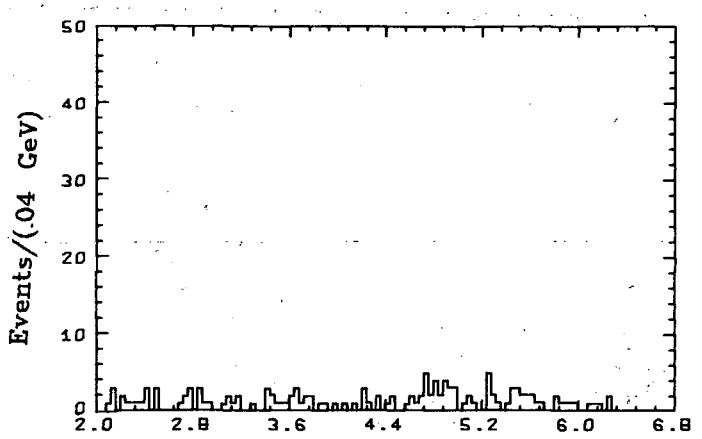

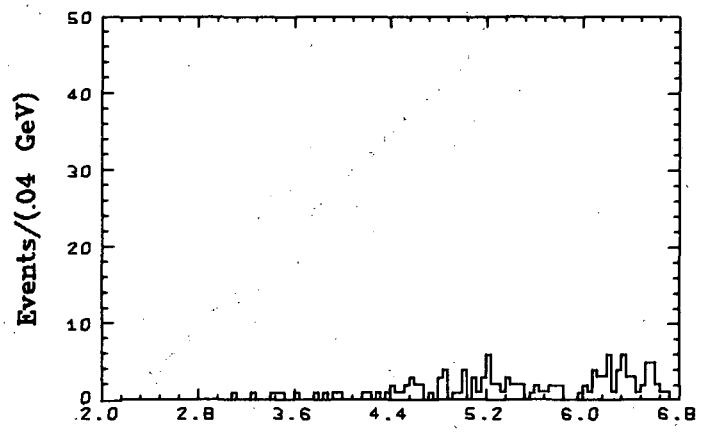

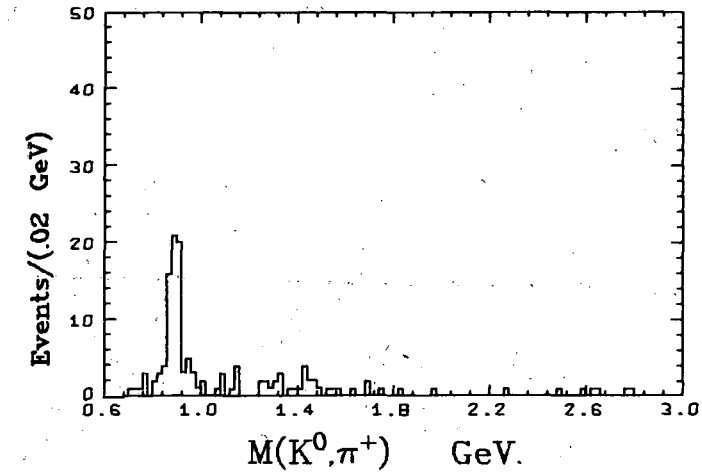

XBL 715-959

Fig. 73

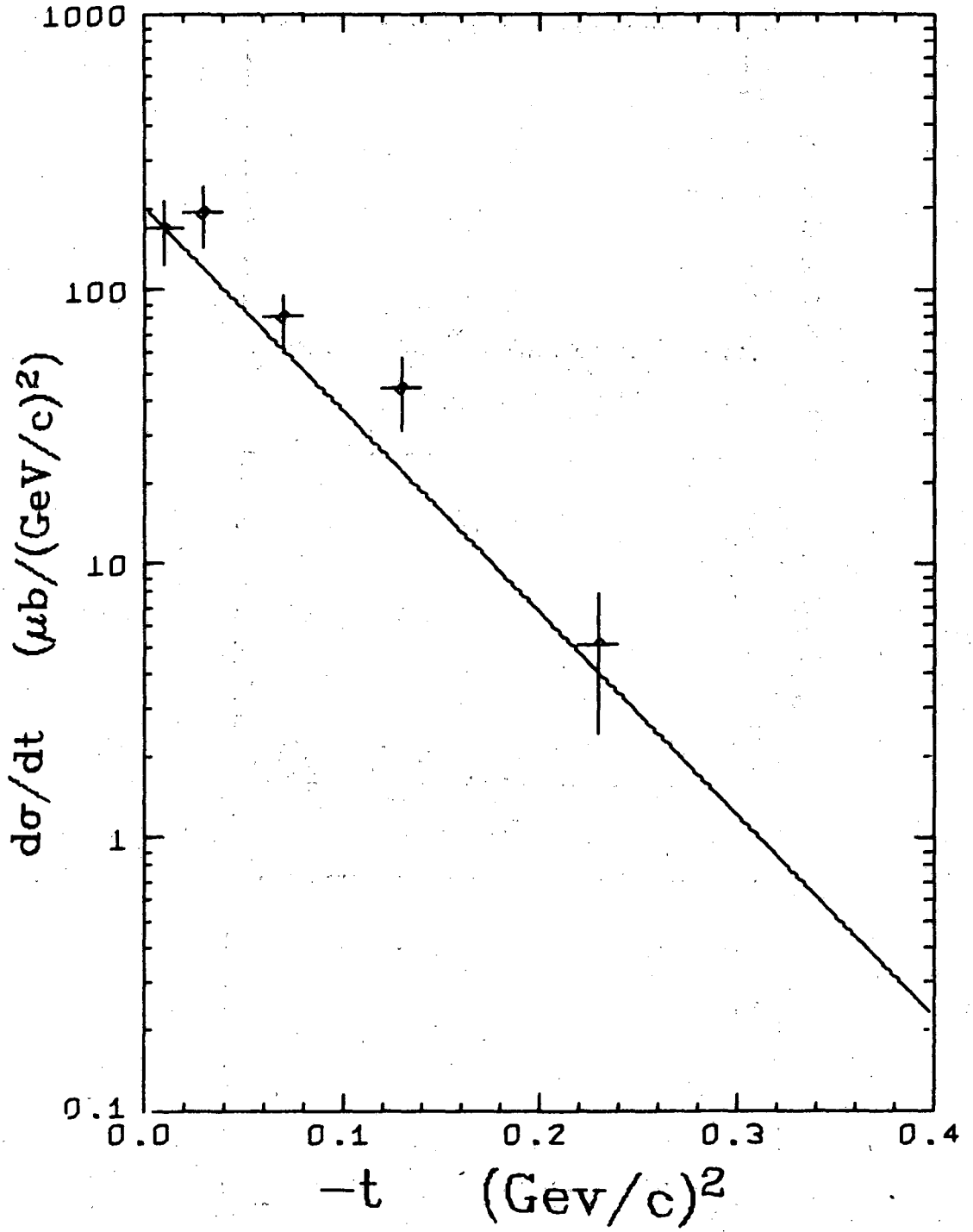

Fig. 74

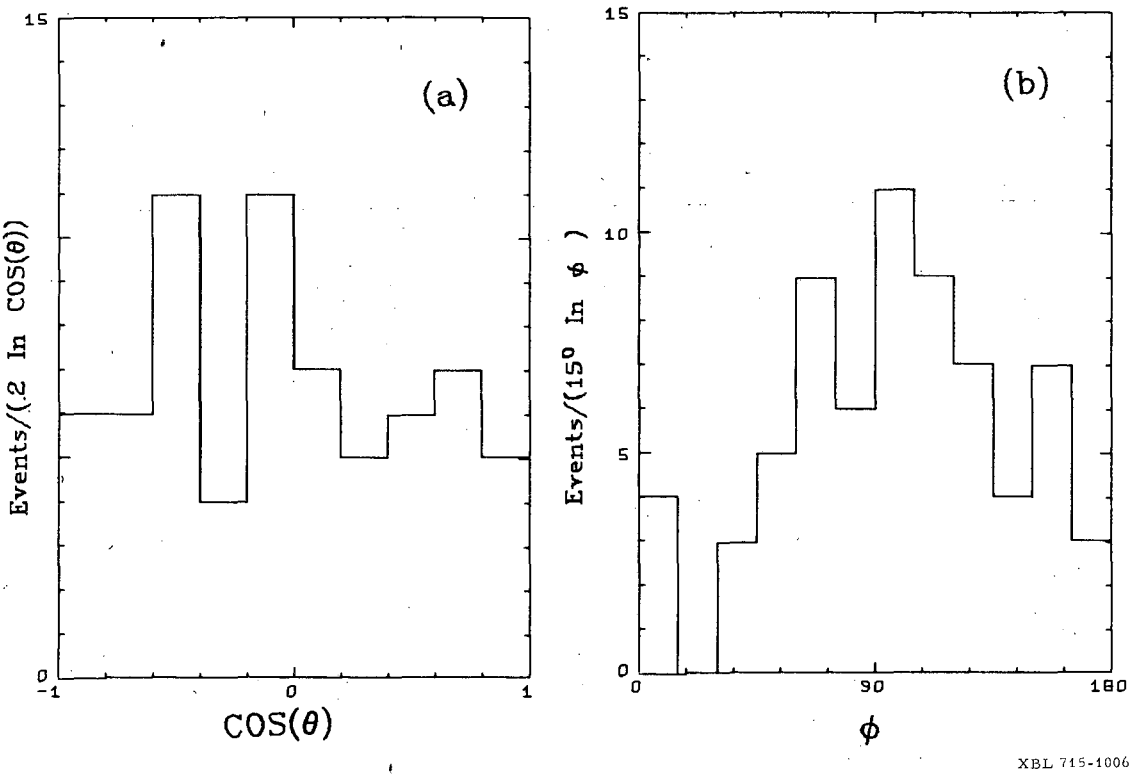
(a)
(b)
Events/(.2 ln COS(θ))
Events/(15° ln φ)
COS(θ)
φ
15
10
5
0
-1
0
1
90
180
XBL 715-1006

Fig. 75

TECHNICAL INFORMATION DIVISION
LAWRENCE BERKELEY LABORATORY
UNIVERSITY OF CALIFORNIA
BERKELEY, CALIFORNIA 94720